Accession No. _____

Contract Program or Project Title: Non-Equilibrium Phase Change Studies
FIN # A 3045

Subject of this Document: Preliminary Data Analysis Report - Volume I

Type of Document: Informal Report

Author(s): N. Abuaf, B. J. C. Wu, G. Zimmer, and O. C. Jones, Jr.

Date of Document: January 1980

Responsible NRC Individual
and NRC Office or Division: Y. Y. Hsu and L. Thompson
Separate Effects Branch

This document was prepared primarily for preliminary or internal use. It has not received full review and approval. Since there may be substantive changes, this document should not be considered final.

Brookhaven National Laboratory
Upton, NY 11973
Associated Universities, Inc.
for the
U.S. Department of Energy

Prepared for
U.S. Nuclear Regulatory Commission
Washington, D. C. 20555
Under Interagency Agreement EY-76-C-02-0016
NRC FIN No. A-3045

INTERIM REPORT

BNL-NUREG-27138
INFORMAL REPORT
LIMITED DISTRIBUTION

PRELIMINARY DATA ANALYSIS REPORT

VOLUME I

(SECTIONS 1 THROUGH 5)

N. ABUAF, B.J.C. WU, G. ZIMMER,
AND O. C. JONES, JR.

REACTOR SAFETY EXPERIMENTAL MODELING GROUP

DATE PUBLISHED - JANUARY 1980

DEPARTMENT OF NUCLEAR ENERGY BROOKHAVEN NATIONAL LABORATORY
UPTON, NEW YORK 11973

Prepared for the U.S. Nuclear Regulatory Commission
Office of NuclearRegulatory Research
Contract No.EY-76-C-02-0016

BNL-NUREG-27138
INFORMAL REPORT
LIMITED DISTRIBUTION

PRELIMINARY DATA ANALYSIS REPORT

By

N. Abuaf, B.J.C. Wu, G. Zimmer
and O. C. Jones, Jr.

Reactor Safety Experimental Modeling Group
Thermal Hydraulic Development Division
Department of Nuclear Energy
Brookhaven National Laboratory
Upton, New York 11973

January 1980

Prepared for the U.S. Nuclear Regulatory Commission
Office of Nuclear Regulatory Research
Contract No. EY-76-C-02-0016
FIN No. A-3045

ABSTRACT

A preliminary evaluation of the experimental data on flashing of water in a converging-diverging nozzle obtained at BNL is presented for milestone reporting purposes. Experimental data of the static pressure distribution, and of axial and transverse void fraction distributions are reported along with photographic records of the two-phase flow downstream of the test section.

These data are preliminary. The experiments described herein represent a total of close to one-quarter million pieces of information for the data included in this report. It has been impossible to examine each point individually, and up to this time the data reported herein have not been thoroughly reviewed and verified. Therefore, the data and the conclusions based on these data should be treated as preliminary and subject to change due to the inclusion of more definitive and accurate calibration data and procedures in the data reduction and evaluation process.

The development of voids in nonequilibrium flashing flows is shown through the Oswatitsch integral to be dependent on three major phenomena: an accurate description of the void inception point which will determine the initial and subsequent liquid superheats; a specification of the interfacial mass transfer rates which depend on the local superheat; and the local interfacial area density where the mass transfer occurs. The flashing onset correlation of Alamgir and Lienhard (1979) was extended to accurately predict flashing inception in pipe and nozzle flows with subcooled inlets. A void development model was based on a simple concept for interfacial area density in conjunction with a conduction-controlled bubble growth law. This model was applied to the

experiments reported herein, and to those of Reocreux (1974) and found to give a reasonable description of the measured void distributions up to approximately 25% voids. This is the expected range encompassing bubbly flows.

Comparison of the BNL experiments with TRAC-P1A (Mod-0) predictions revealed that while the code gave a good qualitative description of the flow, it was inadequate in predicting the flashing inception point. This failure led to quantitative discrepancies in the predicted and measured flow parameters. Specific modifications to rectify this are suggested.

TABLE OF CONTENTS

TABLE OF CONTENTS (Cont'd)

LIST OF FIGURES

Figure

LIST OF FIGURES (Cont'd)

Figure

LIST OF FIGURES (Cont'd)

Figure

LIST OF FIGURES (Cont'd)

Figure

LIST OF FIGURES (Cont'd)

Figure

Figure

LIST OF FIGURES (Cont'd)

Figure

LIST OF TABLES

PRINCIPAL NOMENCLATURE

A	cross section area
A_s	interfacial area density
a	thermal diffusivity
C_o	void distribution parameter
C_Γ	parameter in Eq. (6.21)
c	static quality
c_p	specific heat at constant pressure
D	diameter
DP	pressure differential between the test section inlet (tap 1) and a specific tap location along the nozzle. (This difference does not include any gravitational head effects.)
DP^*	$= DP/1/2\rho U_o^2$, dimensionless pressure differential
DPP	$= DP_m^* - DP_c^*$
G	mass flux
G_g	mass flow rate of vapor
g	gravitational acceleration
h	heat transfer coefficient or, enthalpy
I_E	number of counts for a specific period of time at a given location while the test section is empty (full of air)
I_F	number of counts for a specific period of time at a given location while the test section is full of water
$I_{2\phi}$	number of counts for a specific period of time at a given location under two-phase conditions
J	nucleation rate
j	volumetric flux
K_s	constant in Eq. (6.19)
k	thermal conductivity
L	latent heat, or axial length

$m(Z,\zeta)$	mass of a vapor bubble at Z nucleated at
N	number density
p	pressure
$\dot{q}_i''$	interfacial heat flux
R	radial coordinate
r	radius
T	temperature
t	time
U_o	test section inlet velocity = G_{in}/ρ_{in}
u	velocity
V_{gj}	drift velocity of vapor
x	flow quality
Z	axial coordinate
α	void fraction
β	defined in Eq. (6.21a)
Γ_v	volumetric rate of vapor mass generation
ζ	dummy variable of integration
ξ_h	perimeter
ρ	mass density
μ	γ attenuation coefficient
σ	surface tension

Subscript

b	bubbles
c	single phase calibration
crit	quantity pertaining to critical size

ct	condensing tank (test section discharge)
d	droplets
f	saturated liquid
g	saturated vapor
in	test section inlet
ℓ	liquid
m	measured, or mixture
NVG	point of net vapor generation
o	initial point
s or sat	saturation
v	vapor

Superscript

*	dimensionless
+	throat

Symbol

< >	area averaged quantity

1. INTRODUCTION

Several experimental, as well as analytical investigations have been undertaken to date in order to calculate the discharge flow rates of two-phase mixtures from pipes, nozzles, and orifices accurately. This problem presents itself in the safety analysis of water cooled nuclear reactors and also in the safe storage and handling of liquid cryogens in space applications.

During a hypothetical Loss-Of-Coolant Accident (LOCA) of a nuclear reactor, the flow is expected to be choked at the break. The discharge flow rate affects the heat transfer in the core, the depressurization rate of the containment vessel, and it dictates the design requirements of the Emergency Core Cooling System (ECCS). Theoretical models have been proposed, and large computer codes have been developed, to predict the critical flow rates and their dependence on the upstream thermodynamic and flow conditions, as well as the pipe size and component geometry. At present, there is no general model or correlation for critical flows which considers both thermal nonequilibrium and relative velocities between the phases and which is valid for a wide range of pipe lengths, diameters, and upstream conditions, including subcooled liquid. A modeling effort in conjunction with well-controlled experiments is currently being undertaken at Brookhaven National Laboratory to investigate and measure the actual vapor generation rates under nonequilibrium conditions. The purpose of this report is to describe the test facility, including the venturi test section and loop instrumentation, as well as to present the experimental results acquired under nonequilibrium flashing conditions, including axial static pressure distributions, axial and transverse void fraction distributions, and photographic observations. In addition, the experimental data will be compared with analytical and code models.

2. REVIEW OF THE LITERATURE

Extensive analytical and experimental work has been reported on the two-phase critical flows in the last three decades. Thorough reviews have been presented by Hsu (1972) and Saha (1978). The latter summarized the various available critical flow models and emphasized the effects of thermal nonequilibrium and relative velocities between the phases, which become prominent under certain conditions. Since the objective of the present research was the determination of the vapor generation rates under nonequilibrium conditions, we will concentrate on pertinent experimental work in the literature.

To study flashing flows and critical flow conditions, researchers have used several kinds of test facilities. Some use an upstream vessel containing a saturated or subcooled liquid, which expands and may vaporize in the test section. Others have used systems where the two phases are generated separately and then mixed together before being introduced into the test section. When either system is operated as a once-through experiment, the flow from the test section discharges into a downstream container whose pressure can be adjusted independently of the upstream conditions. When either system is operated as a steady closed loop, the control of the downstream pressure independently of the upstream conditions becomes more difficult to achieve due to the hydrodynamic coupling of the test section with the loop. In this report, we will consider only experiments conducted with subcooled or saturated inlet conditions. The various test sections investigated to date can be classified as: first, long tubes and nozzles; second, short tubes and short nozzles; and third, orifices.

Long tubes and nozzles can be characterized by L/D > 40 (Seynhaeve 1977). Such experiments were conducted by Isbin, Moy, and DaCruz (1957), James (1962), Fauske (1965), Reocreux and Seynhaeve (1974), Ardron and Ackerman (1978), etc. Reocreux (1974) was the first researcher to provide pressure measurements, as well as void fraction distributions which allow the direct calculation of the vapor generation rates, provided a specific slip model is adopted. In all of the experiments conducted with long straight pipes, the frictional effects are equally important as the vapor generation rate to the choking condition, and thus the vapor generation effect can not be singled out easily.

Short tubes and nozzles with 1 < L/D < 40 have been extensively investigated by Silver (1948), Zaloudek (1963), Fauske and Henry (1971), and Schrock, Starkman and Brown (1977). Similar choked flow experiments were also reported by Simoneau (1975) and Hendrick, Simoneau, and Barrows (1976) with cryogenic liquids. Although the experiments in this group with a converging diverging nozzle can provide information on the flashing inception, and choking conditions, no detailed void fraction measurements were performed to allow the determination of vapor generation rates in any of the experiments in the literature.

Experiments with orifices were usually conducted using orifices with L/D < 1 placed in a uniform cross section tube, and the jet has been investigated by several authors. More recently, Seynhaeve (1977) measured axial and radial void fractions of the jet, in addition to the pressure distributions.

3. EXPERIMENTAL TECHNIQUES

3.1 Flow Loop

The main flow loop presented in Fig. 3-1 is constructed from "three inch" nominal (7.6 cm) stainless steel pipe. High purity water is circulated through the loop using a centrifugal pump rated at 1500 ℓ/min at a head of 600 kPa.

Starting from the pump, the fluid passes through a flow control station where the flow rate can be controlled from 3 to 950 ℓ/min and measured with an accuracy of 1/2 percent of full scale. Excess flow from the pump is directed to secondary loops for cooling, purification and simple bypass flow routing. After the flow rate is set and measured, the fluid passes through the heater system where up to 520 kW of heat can be added to the water, and the outlet temperature can be regulated to $\pm$ 0.3°C over the entire controlled flow range.

Leaving the heater system, the fluid passes through the test section. A pressurizer is connected to the main loop between the heater system and the test section and, when valved in, the pressurizer fixes the inlet pressure to the test section. Alternately, the pressurizer may be isolated from the loop and in this fashion, the pressure in the loop is controlled by pump flow rate. Thus, two modes of operation are possible: the pressure controlled and the flow controlled modes. Once the fluid has passed through the test section, it enters a condensing tank where a cooling spray is utilized to condense the vapor and to fix the tank temperature. Since the pressure in the tank is essentially the same as in the test section exit,

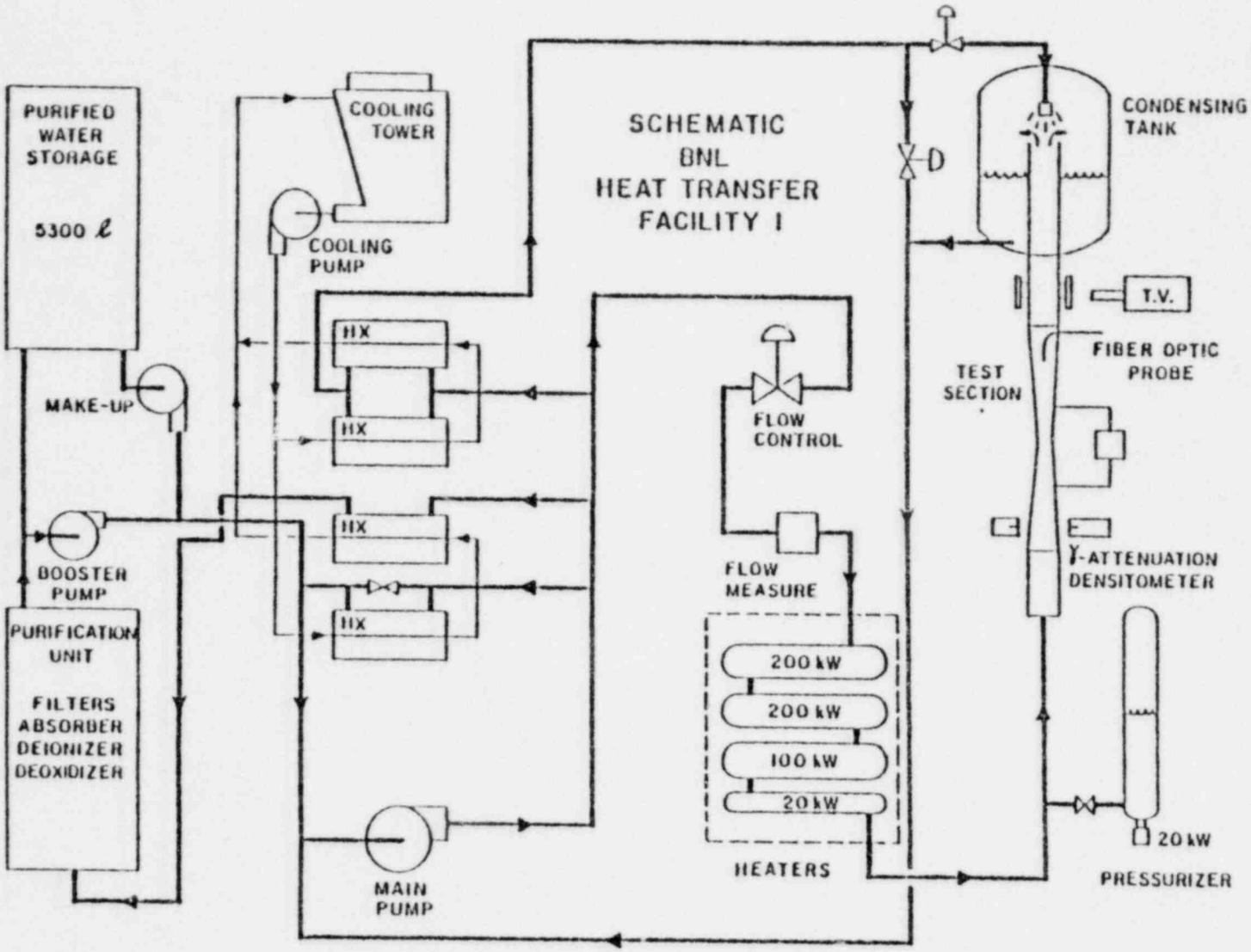

Figure 3-1 Schematic of BNL Heat Transfer Facility

Rev.
12/4/79

the condensing tank and pressurizer can be used together to fix the pressure drop across the test section.

The fluid travels, after leaving the condensing tank, back to the pump, and, depending on conditions, cooling water can be added to this flow to prevent cavitation in the pump. Cooling water is provided from excess pump flow and is cooled by shell and tube heat exchangers tied to a 730 kW cooling tower.

Purification of the test fluid is accomplished during initial filling of the test loop. The water is deoxidized, deionized and passed through 0.22 micron filters. In addition, about 40 ℓ/min of excess pump flow is passed through the purification station as a polishing procedure during flow loop operation.

3.2 Test Section

The test section is made of stainless steel with a total length of 78.7 cm, including a symmetrical converging/diverging portion of 55.9 cm length and inside diameters of 5.1 cm at the ends and 2.5 cm at the throat. The wall thickness varies only from 0.57 mm to 0.60 mm over the entire tube length. "Intrimiks" were used to accurately map the interior dimension of TS-2. The data taken have been reduced and analyzed and are summarized in Figs. 3-2 and 3-3 . A reference datum was established as the flange face on the inlet to the test section assembly. Figure 3-2 shows the mean inside diameter plotted as a function of the axial distance from the reference datum. Each point is the mean of four measurements made at a particular axial distance with the "intrimik" rotated 90° in each case. The

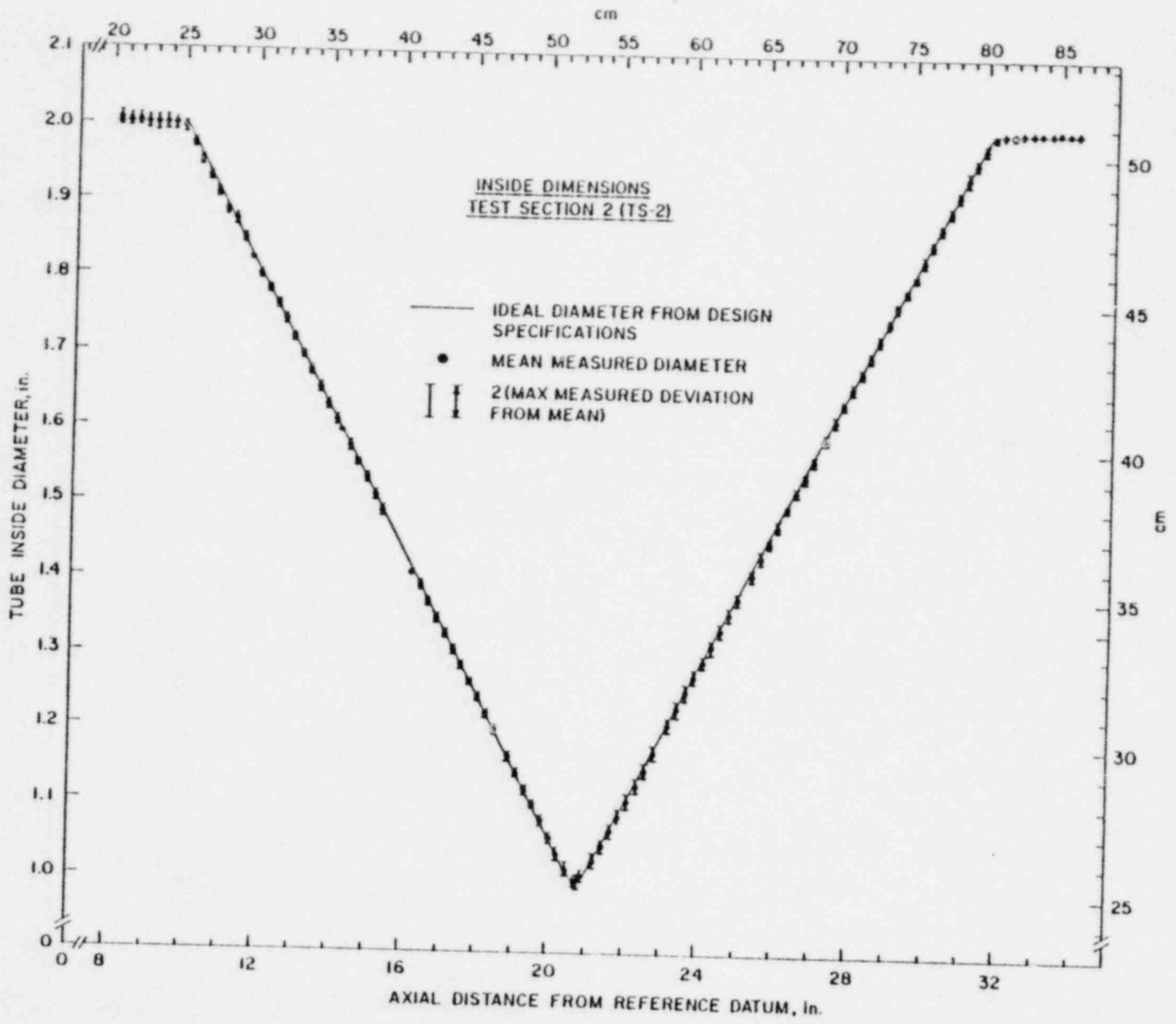

Figure 3-2 Inside Dimensions of TS-2 (BNL Neg. No. 10-243-780)

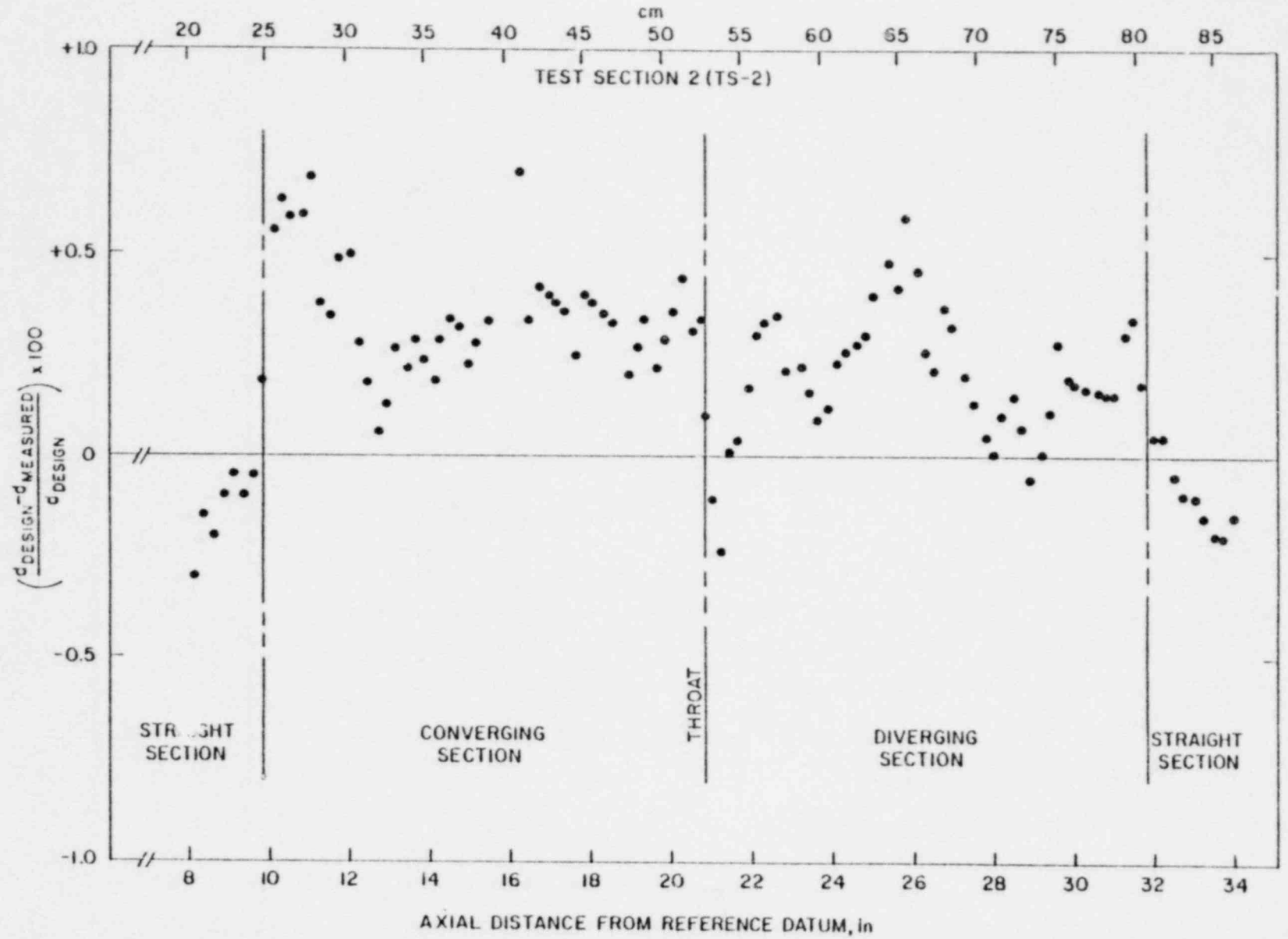

Figure 3-3 Deviation From Design of TS-2 Inside Dimensions (BNL Neg. No. 10-244-78).

"error bars" show the maximum dev'ation from the mean encountered at each point. The solid line plotted is the actual design dimensions for the test section that were specified prior to construction. A point by point comparison of the design versus the measured dimensions is given in Fig. 3-3, and shows that most of the measured dimensions deviate less than one-half a percent from the design.

The test section design and construction was performed in three levels, each with an increased complexity in instrumentation. In the first level, 49 wall pressure taps (0.4 mm in diameter) were installed on 1.27 cm centers along the length of the venturi, in addition to a set of observation windows located 30 cm downstream of the test section exit, which allowed photographic observations by flash photography. Taps 1, 2, and 3 are in the constant area entrance of the converging section, while Taps 47, 48, and 49 are at the exit of the diverging section. If we take Tap 1 as the origin of the axial coordinate, as designed, Tap 25 is located 30.61 cm downstream. However, as constructed, the throat determined from the actual diameter measurements reported above is located at 30.48 cm downstream of Tap 1. This fact implies that Tap 25 is 0.13 cm downstream of the geometric throat. An additional pressure tap, 50, is located at 159 cm upstream of the test section inlet tap 1. The gauge pressure at Tap 50, with respect to the atmospheric pressure, is constantly monitored at the control panel, and it provides the needed information to calculate the absolute pressure at the test section inlet within an accuracy of < 1 percent. The temperature is monitored by means of two platinum resistance thermometers, one located near pressure Tap 50 for the flow inlet conditions and one at the condensing tank for the flow outlet conditions.

In the second level, a single channel (i.e., single beam) gamma densitometer which can be traversed virtually everywhere within the test section was added for chordal averaged void fraction measurements. In the third level, the single beam densitometer was replaced by a bank of five gamma beams for more efficient data taking. A stationary hydrofoil-like probe containing ten pairs of local sensors was also planned but not executed that will allow the measurement of local void fractions and phase velocities across a particular diameter.

To date, pressure distribution, as well as void fraction distribution data have been taken, and the flashing regimes were recorded photographically by means of a flash and a still camera arrangement located downstream of the test section outlet.

3.3. Loop Operation Conditions and Instrumentation

The operational range of the facility is summarized in Table 3.1. The inlet pressure and temperature can be varied from 100-1000 kPa and from room temperature to 150°C respectively. The loop flow rate capability ranges from 3 to 1000 liters per minute with 0.5 percent measurement accuracy. For the test section this represents a maximum inlet Reynolds number of 10^6. The various loop instrumentation, including ranges and accuracies, are tabulated in Table 3.2 Pressure measurements are accomplished by means of Statham gauges, each calibrated to an accuracy better than 0.1 percent of the reading. The temperatures are measured by thermocouples and RTD's, and the flow rate measurements are obtained by two Cox turbine flow meters, upstream of the test section in the subcooled flow region.

TABLE 3-1

OPERATIONAL RANGE OF THE FACILITY

Test Section Inlet Pressure	100 - 1000 kPa
Test Section Inlet Temperature	20 - 150°C
Mass Flow rates	3 - 1000 lbm^2s
Maximum test section inlet Reynolds Number	10^6

Converging Test Section Inlet Conditions From Subcooled To Low Qualities

TABLE 3-2

TEST SECTION INSTRUMENTATION

QUALITY MEASURED	TYPE OF SENSOR	RANGE	ACCURACY
Temperature	Resistance Temp. Detector (RTD)	-200 to 500°C	1.2% @ 200°C *
Differential Pressure	Strain Gage Δp Transducer	4 to 500 kPa	1% of Reading **
Flow Rate	Turbine Meter	3 to 950 ℓ/min	0.5% of reading +
Void Fraction	Gamma Densitometer (Thulium/Cad-Telluride)	0 to 1	5% Steady State ++ (Future 5% per 1 ms)

* Mfg. spec. - calibrated at 0°C and 100°C within 0.1°C.

** Mfg. spec. - calibrated generally to 0.1% F.S. by Mensor quartz monometer to 1 part in 300,000.

\+ Mfg. calibration

++ For single beam, low activity source. Multibeam, high activity sources are significantly more accurate since the count rates are 20-30 times greater.

4. DATA ACQUISITION

4.1 General Data Acquisition System

The centralized Data Acquisition and Data Analysis System (DADAS) was designed as a real time digital data system with multiterminal multitasking capability. The system was constructed around a Hewlett Packard 9640 system consisting of a 21MX minicomputer with 112 kilowords of central memory, 7.5 megaword cartridge discs, 9 track magnetic tape transport and paper tape I/O. Central control of the system is accomplished with a CRT terminal while the 3 satellite stations employ silent 700 terminals. Tabular and graphical presentation of data is achieved with a Varian electrostatic printer/plotter capable of listing 600 LPM and plotting 1.6 ips. Interface of the ADC systems is both direct, an interface per device, and via the universal interface bus, IEEE standard 488.

Three levels of ADC speed and resolution are incorporated within DADAS. The slow speed, high resolution system employs an integrating digital voltmeter with microvolt resolution and 300 channel guarded crossbar scanner. The through-put rate of this system is up to 18 measurements per second with high common mode voltage rejection capability. The intermediate speed system is a 15 bit ($\pm$ 10.24 volts) multiplexed ADC with a 50 kHz through-put rate. The system employs a single programmable gain amplifier and a signal conditioning amplifier and filter per channel. The system has high common mode voltage rejection capability and can be connected directly to experiments. The high speed system is also a 15 bit ($\pm$ 10.24 volt) multiplexed ADC with a 500 kHz through-put rate. The system has eight input

channels with simultaneous sample and hold amplifiers. This system was designed specifically for digitizing analog tapes.

4.2 Static Pressure Measurement Set-Up

Each of the 49 pressure taps on the test section can be connected to either of two manifolds, one a common high side the other a common low side, via two hand operated toggle valves to the low or high pressure sides of a pressure transducer bank. The differential pressure between two locations along the test section can be measured by connecting the two taps to the low and high sides of the pressure transducer. Six Statham pressure transducers with the ranges of 17, 34, 69, 170, 340, and 690 kPa (2.5, 5, 10, 25, 50, 100 psi) were connected in parallel to the two pressure measuring manifolds through two solenoid valves. A third solenoid valve in each transducer allows the shorting of the high and low pressure lines and thus provides a means of measuring and monitoring the zero point stability of the transducer preceding every Δp measurement. The solenoid valves are designed for a 200 psi differential pressure and were tested prior to installation. Once the two pressure taps were manually connected to the high and low pressure manifolds, the computer controlled procedure described below was initiated for the recording of the data.

Each measurement started with the pressure gauge shorted to record the zero Δp output. The pressure differential between the two taps was then measured across the 690 kPa (100 psi) range transducer. Once the pressure differential was calculated, the system automatically selected a pressure transducer such that the DP to be measured would fall between 25 and 75

percent of the full range of the particular transducer chosen. With the chosen transducer, the computer first measured the gauge's zero output when shorted, then took 20 consecutive DP readings, averaged them, and calculated their standard deviation. The same sequence was repeated once again and the new average of 20 new readings was compared to the last one calculated. If the two consecutive averages were within one percent of each other, the measurement was accepted and printed out as a data point. At the same time, the instantaneous flow rate and other flow variables of interest were also recorded. On the other hand, if the two consecutive averages did not satisfy the acceptance criterion, the computer repeated this procedure until the criterion was met or until 15 sets of 20 readings each were made and the last output was printed as the data point. This procedure permitted the measurement of static pressures with an accuracy of 1 percent of the reading as quoted in Table 3-2. It also allowed us to detect the presence of large pressure fluctuations at the onset of flashing or condensation. At other locations, such fluctuations were not observed and the readings converged smoothly. It should be noted that since the pressure transducers were located at the same horizontal level, gravity effects due to the elevation difference of the pressure taps were canceled out in the measurements. The pressure data reported here represent the difference, at two pressure taps, of the sum of the static pressure and gravational head. A typical output for an experiment is presented in Table 4-1, which depicts the data acquisition format with the tap identity, pressure data, as well as various other instantaneous flow parameters of interest.

TABLE 4-1

TYPICAL PRESSURE DROP DATA

BNL FLASHING FLOWS EXPERIMENT
PRESSURE DROP DATA FROM
TEST SECTION # 2

RUN NUMBER 74

TAPS	LOOP FLOW LTR/SEC	TEMPERATURES (DEG C) FLOW METER	TS INLET	COND TANK	PRESSURE (KPA) TS INLET	COND TANK	VELOCITY CM SEC	REYNOLDS NUMBER	DIFFERENTIAL PRES MEASURED	DIMENSIO
1-3	10.36	96.3	99.3	87.9	285.9	55.5	510.4	.865E+06	.00	.0
1-5	10.35	96.3	99.3	87.9	284.7	55.5	509.8	.864E+06	2.38	.
1-7	10.39	96.3	99.4	88.0	284.5	55.4	511.6	.867E+06	6.21	.
1-9	10.37	96.3	99.3	87.8	283.8	55.4	510.6	.866E+06	10.95	.
1-11	10.39	96.3	99.3	87.8	284.6	55.5	511.4	.867E+06	18.39	1.
1-13	10.36	96.3	99.4	87.9	284.8	55.5	510.3	.865E+06	26.64	2.
1-15	10.38	96.3	99.3	87.9	284.7	55.5	511.2	.866E+06	36.44	2.
1-17	10.37	96.3	99.4	87.7	284.0	55.5	510.7	.866E+06	56.23	4.
1-19	10.36	96.3	99.4	87.6	283.8	55.6	510.1	.865E+06	73.37	5.
1-20	10.36	96.3	99.4	87.9	284.2	55.6	510.1	.865E+06	87.11	6.
1-21	10.39	96.3	99.3	87.8	284.4	55.6	511.5	.867E+06	104.25	8.
1-22	10.36	96.3	99.3	87.9	284.6	55.6	510.3	.865E+06	127.88	10.
1-23	10.38	96.3	99.3	87.8	285.2	55.6	511.3	.867E+06	147.31	11.
1-24	10.36	96.3	99.3	87.8	284.0	55.6	510.3	.865E+06	176.15	14.
1-25	10.36	96.3	99.4	87.6	283.5	55.6	510.0	.865E+06	208.24	16.
1-26	10.34	96.3	99.3	87.6	284.8	55.8	509.2	.863E+06	196.18	15.
1-27	10.39	96.3	99.3	87.9	285.4	55.8	511.5	.867E+06	195.73	15.
1-28	10.37	96.3	99.3	87.8	285.5	55.7	510.5	.865E+06	196.05	15.
1-29	10.37	96.3	99.3	87.8	285.8	55.8	510.7	.866E+06	195.34	15.
1-31	10.39	96.3	99.3	87.7	283.8	55.8	511.7	.867E+06	194.48	15.
1-33	10.39	96.3	99.3	87.9	284.0	55.7	511.4	.867E+06	194.10	15.
1-35	10.35	96.3	99.3	88.0	284.8	55.7	509.9	.864E+06	193.55	15.
1-37	10.38	96.3	99.3	88.2	285.2	55.7	511.0	.866E+06	193.37	15.
1-39	10.38	96.3	99.4	88.1	285.7	55.7	510.9	.866E+06	192.95	15.
1-41	10.34	96.3	99.3	87.8	284.0	55.7	509.4	.863E+06	192.72	15.
1-43	10.38	96.3	99.3	87.8	284.4	55.7	511.1	.866E+06	192.72	15.
1-45	10.38	96.3	99.3	88.1	284.6	55.7	511.2	.866E+06	191.99	15.
1-47	10.35	96.3	99.3	87.8	283.6	55.8	509.7	.864E+06	191.92	15.
1-49	10.39	96.3	99.3	88.2	284.6	55.7	511.6	.867E+06	192.15	15.
50-1	10.37	96.3	99.3	88.1	284.5	55.5	510.5	.865E+06	17.94	1.

4.3 γ-Densitometer for Void Fraction Measurements

Both single- and multiple-beam systems were utilized for these experiments as described below.

4.3.1 Single-Beam Densitometer

The single channel γ densitometer set up presented in Fig. 4-1 was used for the void fraction measurements. For the single-beam system, the Thulium Oxide source was purchased from Amersham Corporation and was irradiated at the High Flux Beam Reactor at Brookhaven National Laboratory. The source strength was kept at a few millicuries due to the presence of high energy-activity (1.12 MeV), which is due to trace amounts ($\sim$70 ppm) of Scandium impurity present in the source material and which caused difficulties from the Health Physics and Safety point-of-view. The source capsule is placed in a "lead pig", with a collimator opening of 2.5 mm in diameter, which determines the size of the γ beam. The detector consisted of a Cadmium Telluride crystal (2.5 x 2.5 mm) mounted on a regular BNC connector. The CdTe detector was connected to "off-the-shelf" radiation electronic components (Tennelec), consisting of a preamplifier (TC 164), a high voltage power supply (TC 948) for the bias voltage (150 V), a linear amplifier (TC 203 BLR), a single channel analyzer (TC 440), a T 541 Timer and a scaler (TC 540A). The single channel analyzer was used in the differential discriminator mode of operation and the energy window was set around 84 keV with a dispersion range of $\pm$ 10 keV. The TC 541 timer was altered by Tennelec to include time intervals as short as 0.1 msec and as long as 54 sec. The γ source holder and detector were set on a traversing mechanism, which allowed both axial and radial traverses along the test section. The axial and radial repositioning of the γ beam by the traversing mechanism can be accomplished with an accuracy of $\pm$ 0.05 mm.

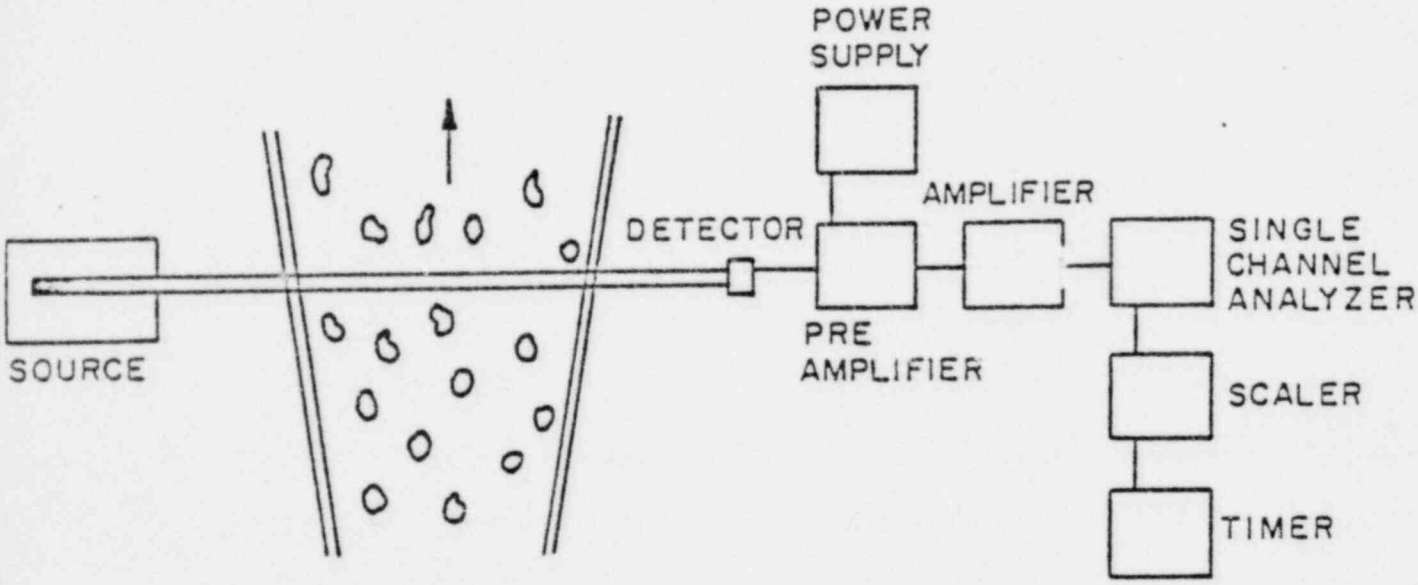

Figure 4-1 Schematic Representation of γ-Densitometer
(BNL Neg. No. 3-1016-79)

The chordal averaged void fraction was calculated from the following relation:

$$\alpha = 1 - \frac{\rho_{\ell c}}{\rho_{\ell m}} \quad \frac{\ln \frac{I_{2\phi}}{I_E}}{\ln \frac{I_F}{I_E}} \qquad (4\text{-}1)$$

where α is the chordal-averaged void fraction, I_E, and I_F are the number of counts during a preset period of time when the test section is "empty", i.e., full of air (attenuation due to stainless steel walls only) and full of water respectively, and $I_{2\phi}$, is the number of counts during the same preset period of time under two-phase flow conditions. $\rho_{\ell c}$ is the water density at the calibration temperature, ($20^{\circ}C$) and $\rho_{\ell m}$ is the water density at the temperature where the experiment was being conducted.

4.3.2 Multibeam γ-Densitometer for Transverse and Axial Void Distributions

The five beam gamma densitometer presented in Fig. 4-2 was used to measure the transverse distribution of the chordal averaged void profiles at various axial locations in the test section under flashing conditions. For each source, Thulium^{170}, obtained as a 99.999% pure oxide powder, was sealed in an aluminum container and irradiated to the desired activity in the HFBR ($\sim$ 5 days). The five sources have 3 mm diameter collimation holes and the sources are placed at 10.2 mm center-to-center distances. Figure 4-3 depicts a horizontal and vertical cross section of the source holder. The second additional row of five sources were added for the possible future purpose of measuring cross correlations in the flow direction. The detector holder presented in Fig. 4-4 has a similar 3 mm diameter collimation holes and contains the set of five Cadmium Telluride detectors mounted on a small circuit board. As observed in Fig. 4-5, which is a pictorial representation of the test

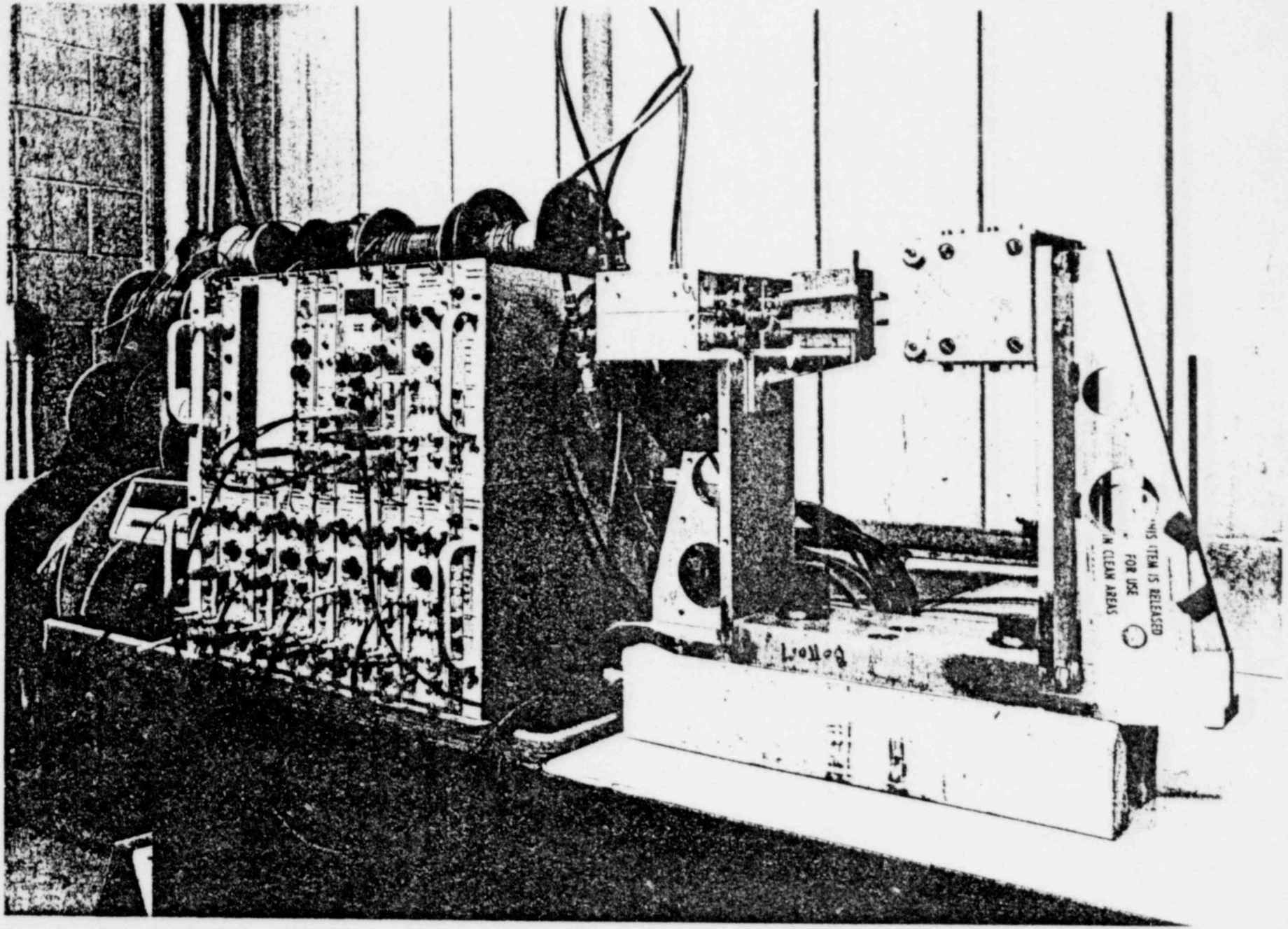

Figure 4-2 Photograph of the Five Beam Gamma Densitometer (BNL Neg. No. 6-1079-79).

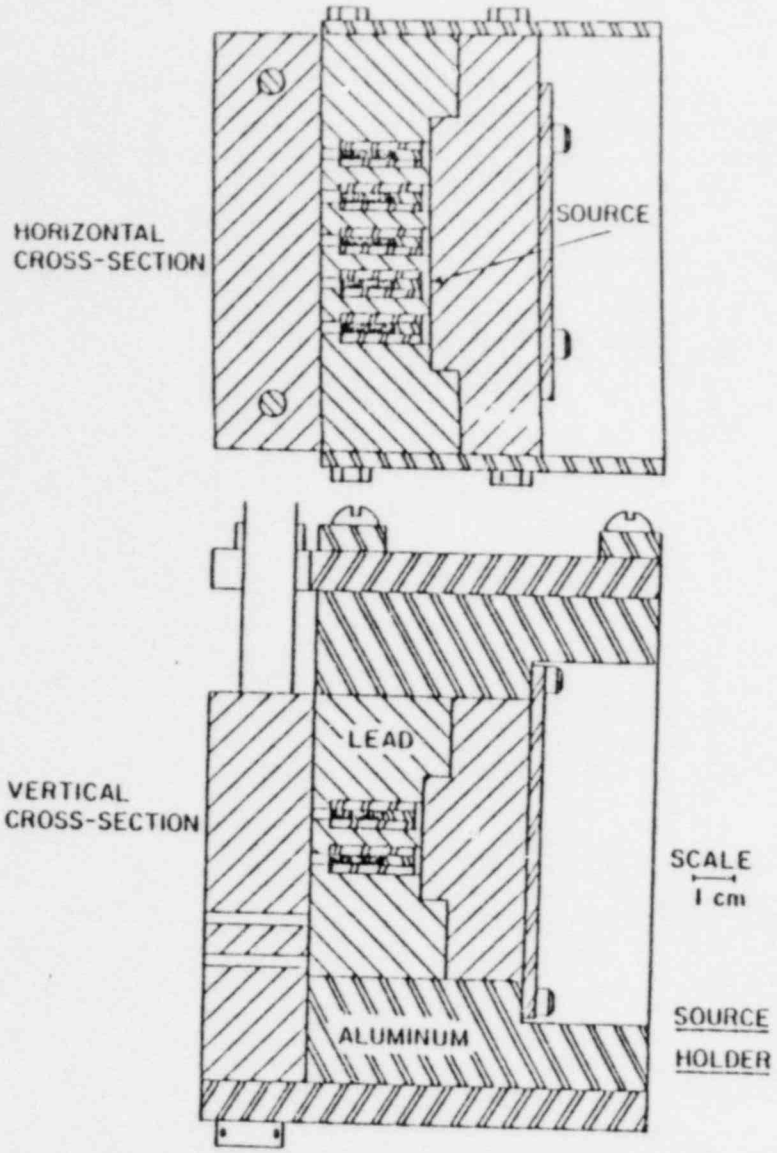

Figure 4-3 - Horizontal and Vertical Cross Sections of the Source Holder. (BNL Neg. No. 11-667-79).

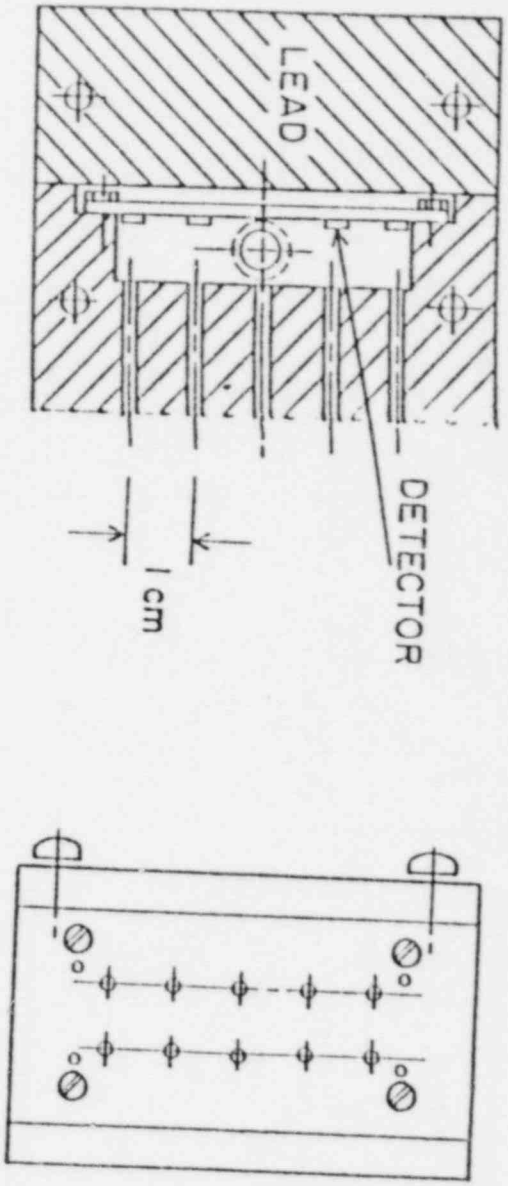

Figure 4-4 - Schematic Representation of the Detector Holder. (BNL Neg. No. 11-671-79).

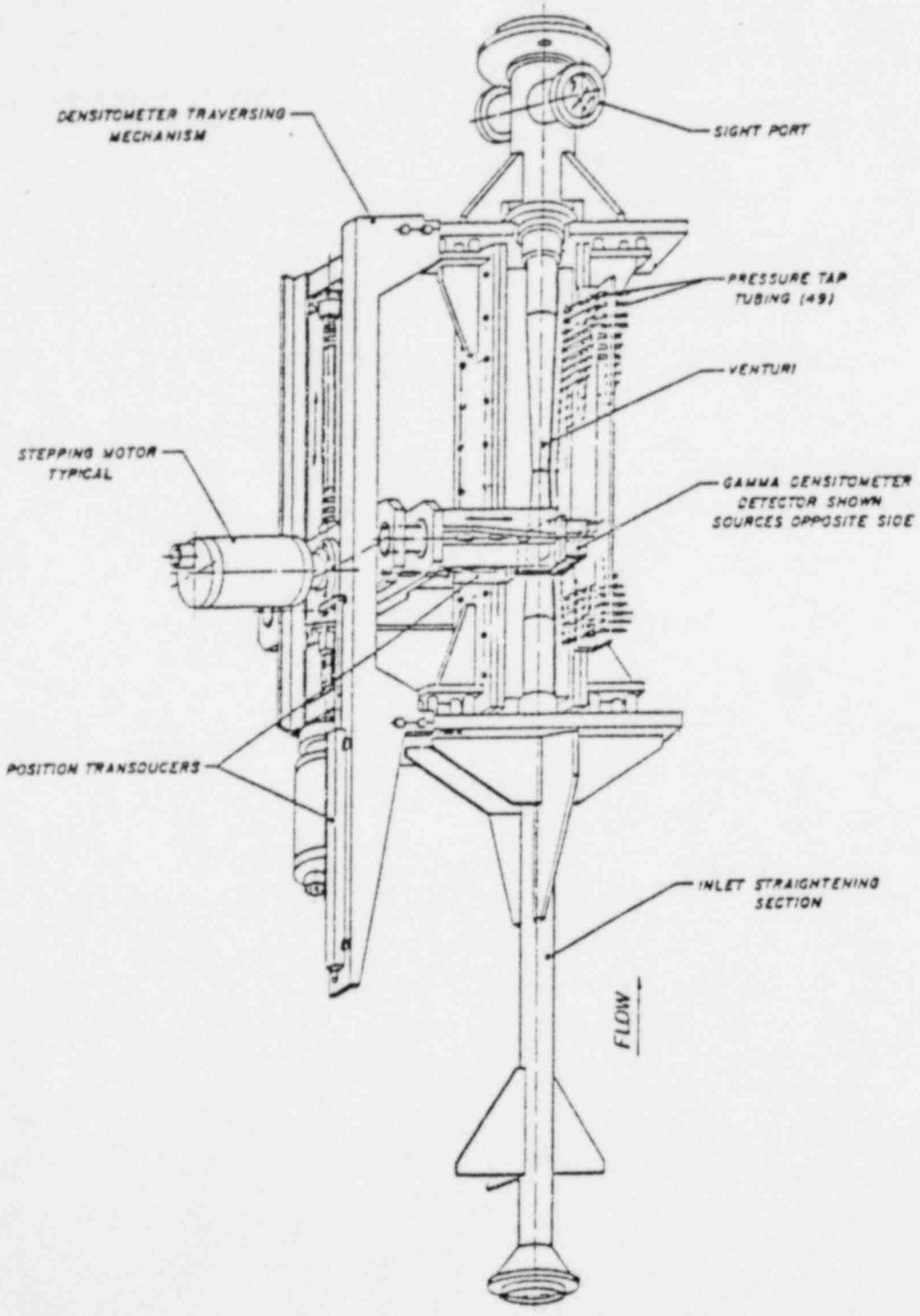

Figure 4-5 - Schematic Representation of the Test Section. (BNL-Neg. No. 10-1406-79).

section TS 2, the source and detector holders are connected to the two arms of the traversing mechanism, which is driven by two motors and which allows the controlled motion of the gamma densitometer system both in the axial and transverse directions.

During the experiment the computer would automatically control the γ-densitometer traversing mechanism to position it at pre-assigned locations along the test section. At each position, 10 sets of 9-second counts of the γ-densitometer would be taken, the corresponding chordal averaged void fraction and standard deviation would be calculated. The γ-densitometer was moved to the next position for new measurements. In the current set-up, 27 axial positions, each with 6 transverse positions at 2.5 mm intervals, were specified. The 27 axial positions covered the test section approximately between taps 3 and 47, generally at 2.54 cm intervals, except in the 10 cm near the throat where the spacing was 1.27 cm. After completing the transverse scan of the γ-densitometer, the computer calculated the cross sectional averaged value from the chordal fraction measured (see Section 5.3.2). Table 4-2 presents the typical output of void fraction measurements at one axial location.

RUN NUMBER 120	87 GPM, 212 DEG F., CTLL 20.				
AXIAL LOCATION FROM TAP 47	12.648				
RADIAL LOCATION FROM HOME	.030	1.046	2.062	3.078	4.094
AVERAGE CORRECTED COUNTS	0.	4515.	5644.	5284.	0.
STD. DEV. IN CORRECTED COUNTS	0.	66.	88.	70.	0.
AVERAGE ALPHA	-.00	.58	.42	.08	-.00
STD. DEV. IN ALPHA	0.00	.03	.03	.02	0.00
5 SOURCE AREA AVERAGED ALPHA	.35				
RADIAL LOCATION FROM HOME	.254	1.270	2.286	3.302	4.318
AVERAGE CORRECTED COUNTS	0.	4577.	5573.	5243.	0.
STD. DEV. IN CORRECTED COUNTS	0.	43.	83.	75.	0.
AVERAGE ALPHA	-.00	.58	.40	.06	-.00
STD. DEV. IN ALPHA	0.00	.02	.03	.03	0.00
5 SOURCE AREA AVERAGED ALPHA	.35				
RADIAL LOCATION FROM HOME	.508	1.524	2.540	3.556	4.572
AVERAGE CORRECTED COUNTS	0.	4601.	5363.	5291.	0.
STD. DEV. IN CORRECTED COUNTS	0.	71.	60.	67.	0.
AVERAGE ALPHA	-.00	.54	.32	.06	-.00
STD. DEV. IN ALPHA	0.00	.03	.02	.03	0.00
5 SOURCE AREA AVERAGED ALPHA	.34				
RADIAL LOCATION FROM HOME	.763	1.779	2.795	3.811	4.827
AVERAGE CORRECTED COUNTS	5262.	4563.	4851.	5200.	0.
STD. DEV. IN CORRECTED COUNTS	63.	49.	81.	71.	0.
AVERAGE ALPHA	.59	.54	.16	.07	-.00
STD. DEV. IN ALPHA	.03	.02	.03	.04	0.00
5 SOURCE AREA AVERAGED ALPHA	.35				

Table 4-2

5. EXPERIMENTAL RESULTS

In this section, results will be presented for the single phase nozzle calibration as well as pressure and void fraction distributions and photographic observations under various flashing regimes. All the experiments reported herein are tabulated in Table 5-1 with their respective inlet conditions, mass flux and corresponding condensing tank conditions.

5.1 Single Phase Calibration

5.1.1 Pressure

They hydrodynamic calibration of the test section was done to determine the performance characteristics under single phase flow conditions and to obtain the axial distribution of the effective nozzle cross-sectional area.

Three main parameters were varied during these calibration tests: the mass flux (1.6-7.9 Mg/m^2 sec), the inlet pressure (300-1000 kPa), and the inlet temperature (23-149°C). These experiments covered Reynolds numbers from 9×10^4 to 9×10^5, based on test section inlet conditions. The raw data for all the single phase calibration experiments are presented in Appendix A and summarized in Table 5-1. Typical pressure drop results with respect to the inlet and as a function of axial distance are presented in Figure 5-1 for several flow conditions. In the converging section, the flow acceleration is accompanied by a pressure drop. The deceleration in the diverging section results in an expected pressure recovery. The unrecovered pressure loss at the nozzle exit is representative of the friction losses.

Figure 5-2 is a plot of the nondimensionalized pressure drop data obtained from 19 different experiments. The quantities ρ and U_o are the density and th velocity at the inlet of the test section. The dots represent the average of the pressure drop, and the bars the standard deviation of all the experiments performed. This maximum deviation is < 5 percent in the converging section, reaches 6 percent at the throat, and reaches a maximum of 10 percent in the diverging section. The single curve corresponds to the pressure distribution due to acceleration only, and was calculated from the geometrical inside diameter measurements. This hydrodynamic calibration provides an effective hydrodynamic area distribution for the test section and will be used for comparison with the flashing data.

TABLE 5-1

SUMMARY OF EXPERIMENTAL CONDITIONS

A. COLD & HOT CALIBRATION

RUN	p_{in}(kPa)	T_{in}(^{o}C)	G(Mg/m^{2}s)	p_{ct}(kPa)	T_{ct}(^{o}C)
1	-----	-----	----	---	-----
2	371	26.4	1.56	354	26.3
3	368	26.8	3.13	345	26.2
4	361	27.2	4.71	331	26.6
5	351	27.6	6.28	311	27.4
6	682	27.7	7.01	647	27.2
7	691	27.3	6.30	657	27.3
8	695	26.9	4.71	652	26.8
9	709	27.1	3.13	674	26.6
10	711	27.0	1.56	683	27.0
11	688	27.7	6.26	632	27.6
12	1033	29.2	7.01	973	29.1
13	1031	29.4	7.88	961	29.3
14	337	23.0	6.25	316	22.9
15	348	22.9	4.74	339	22.9
16	365	66.3	3.08	309	66.1
17	367	64.1	1.56	322	63.9
18	-----	-----	----	---	-----
19	337	94.4	5.49	324	94.5
32	327	11.6	4.71	352	12.
33	315	11.9	6.29	326	11.9
34	336	12.3	3.15	369	12.3
36	293	69.1	3.08	308	68.9
62	692	148.4	2.33	646	148.4
70	213	54.0	3.35	201	48.6
71	211	54.4	3.34	203	48.8

TABLE 5-1

SUMMARY OF EXPERIMENTAL CONDITIONS

A. COLD & HOT CALIBRATION
(continued)

RUN	p_{in}(kPa)	T_{in}(^{o}C)	G(Mg/m^2s)	p_{ct}(kPa)	T_{ct}(^{o}C)
100	220.	21.3	1.57	102.	21.1
101	102.	42.0	3.09	102.	--
102	220.	19.5	3.11	203	19.8
103	212.	19.6	4.66	186.	19.9
109	218.	17.7	1.58	209.	17.9
110	224.	101.9	1.53	216.	102.5
111	226.	100.0	1.53	217.	100.5

TABLE 5-1

SUMMARY OF EXPERIMENTAL CONDITIONS

B. FLASHING EXPERIMENTS

(continued)

RUN	p_{in}(kPa)	T_{in}(°C)	G(Mg/m^{2}s)	p_{ct}(kPa)	T_{ct}(°C)
20	281.	98.3	4.90	245.	98.2
21	393.	100.6	6.01	136.	100.4
22	170.	100.2	3.04	125.	100.1
23	130.	99.4	1.81	121.	99.3
24	160.	98.0	3.05	122.	97.8
25	247.	97.4	4.52	125.	97.3
26	386.	97.8	6.02	132.	97.7
27	326.	130.0	2.95	299.	129.6
28	566.	131.7	5.90	316.	131.4
29	488.	123.5	5.77	210.	115.4
30	375.	125.1	4.50	206.	114.7
31	----	-----	----	----	-----
35	287.	99.4	4.96	250.	99.2
37	296.	100.3	4.94	170.	100.0
38	117.	100.3	2.05	112.	99.8
39	136.	100.5	2.25	112.	100.1
40	168.	100.3	3.02	112.	100.0
41	250.	100.2	4.54	115.	99.8
42	194.	99.6	3.79	114.	99.4
43	287.	100.2	4.97	121.	99.9
44	271.	99.9	4.50	101.	99.9
45	308.	99.8	4.97	99.	100.0
46	223.	99.9	3.79	99.	99.9
47	----	-----	----	----	-----

TABLE 5-1

SUMMARY OF EXPERIMENTAL CONDITIONS

B. FLASHING EXPERIMENTS

(Cont'd)

RUN	p_{in}(kPa)	T_{in}(^{o}C)	G(Mg/m^{2}s)	p_{ct}(kPa)	T_{ct}(^{o}C)
48	183.	99.9	3.04	100	99.9
49	146.	99.9	2.27	99	99.7
50	142.	99.8	2.04	101	99.9
51	----	-----	----	---	-----
52	381.	123.5	4.48	254	123.5
53	395.	123.6	4.45	249	123.6
54	525.	123.6	5.96	252	123.7
55	293.	123.6	2.99	251	123.6
56	261.	123.2	2.20	252	123.6
57	263.	124.7	2.04	256	123.9
58	254.	123.3	2.98	174	110.2
59	254.	123.1	2.98	174	110.2
60	264.	125.8	2.93	186	112.5
61	259.	123.8	2.98	162	108.8
63	739.	148.7	5.85	464	148.7
64	609.	148.8	4.40	463	148.8
65	----	-----	----	---	-----
66	521.	148.8	2.94	463	148.8
67	502.	148.6	2.22	463	148.7
68	395.	143.5	1.24	185	118.0
69	399.	144.3	1.23	188	118.5

SUMMARY OF EXPERIMENTAL CONDITIONS

B. FLAHSING EXPERIMENTS

(continued)

RUN	p_{in}(kPa)	T_{in}(^{o}C)	G(Mg/m^{2}s)	p_{ct}(kPa)	T_{ct}(^{o}C)
72	----	----	----	----	-----
73	275.	99.4	4.90	56.	87.9
731*	281.	99.4	4.88	52.	88.0
732*	285.	99.4	4.93	52.	87.9
733*	288.	99.4	4.91	53.	88.2
734*	287.	99.4	4.91	54.	88.0
735*	287.	99.4	4.91	55.	88.1
736*	287.	99.4	4.90	54.	88.0
737*	287.	99.4	4.91	54.	87.9
74	285.	99.3	4.90	56.	87.9
75	395.	99.3	6.04	57.	88.5
761	396.	99.3	6.04	60.	88.7
762	393.	99.3	6.05	62.	88.0
763	392.	99.3	6.06	65.	88.0
77	157.	99.3	3.06	65.	88.7
771	157.	99.4	3.03	69.	88.3
78	138.	99.3	2.61	71.	88.0
782	138.	99.3	2.61	71.	88.1
79	124.	99.4	2.27	72.	88.2
791	126.	99.4	2.26	73.	88.1
792	126.	99.4	2.26	83.	88.1
80	585.	148.3	4.36	436.	143.5
803	579.	148.3	4.32	432.	143.5
81	493.	148.3	2.91	432.	144.0
811	493.	148.3	2.91	432.	144.7
814	492.	148.3	2.91	428.	144.1
82	376.	142.3	2.36	174.	111.6
823	377.	142.4	2.32	176.	110.9
83	352.	140.0	2.30	150.	107.9
833	348.	139.5	2.29	145.	107.1

*Runs 731 through 737 are subsets of Run 73 as are other runs in the hundreds subsets of their decade base.

TABLE 5-1

SUMMARY OF EXPERIMENTAL CONDITIONS

B. FLASHING EXPERIMENTS

(Cont'd)

RUN	p_{in}(kPa)	T_{in}(^{o}C)	G(Mg/m^{2}s)	p_{ct}(kPa)	T_{ct}(^{o}C)
116	143.	99.9	2.28	127.	100.4
119	151.	100.1	2.63	127.	100.5
122	171.	100.2	3.01	133.	100.7
125	251.	99.9	4.50	165.	100.4
128	248.	100.0	4.49	127.	100.5
129	382.	100.1	5.98	128.	100.6
132	377.	99.6	5.96	125.	100.2
133	350.	121.2	4.43	233.	121.7
136	348.	121.2	4.44	233.	121.7
137	463.	121.2	5.88	233.	121.6
140	465.	121.2	5.91	234.	121.6
141	240.	121.3	2.97	236.	121.6
144	242.	121.3	2.97	237.	121.7
145	306.	121.2	3.70	234.	121.7
148	304.	121.2	3.70	233.	121.6

SYMBOL	RUN	G(Mg/m^{2}s)	p_{in}(kPa)	T_{in}(C)	$p_{c.t.}$(kPa)
○	10	1.56	711	27	683
□	9	3.13	709	27.1	674
◇	8	4.71	695	26.9	652
△	7	6.30	691	27.3	657
×	6	7.01	682	27.7	647

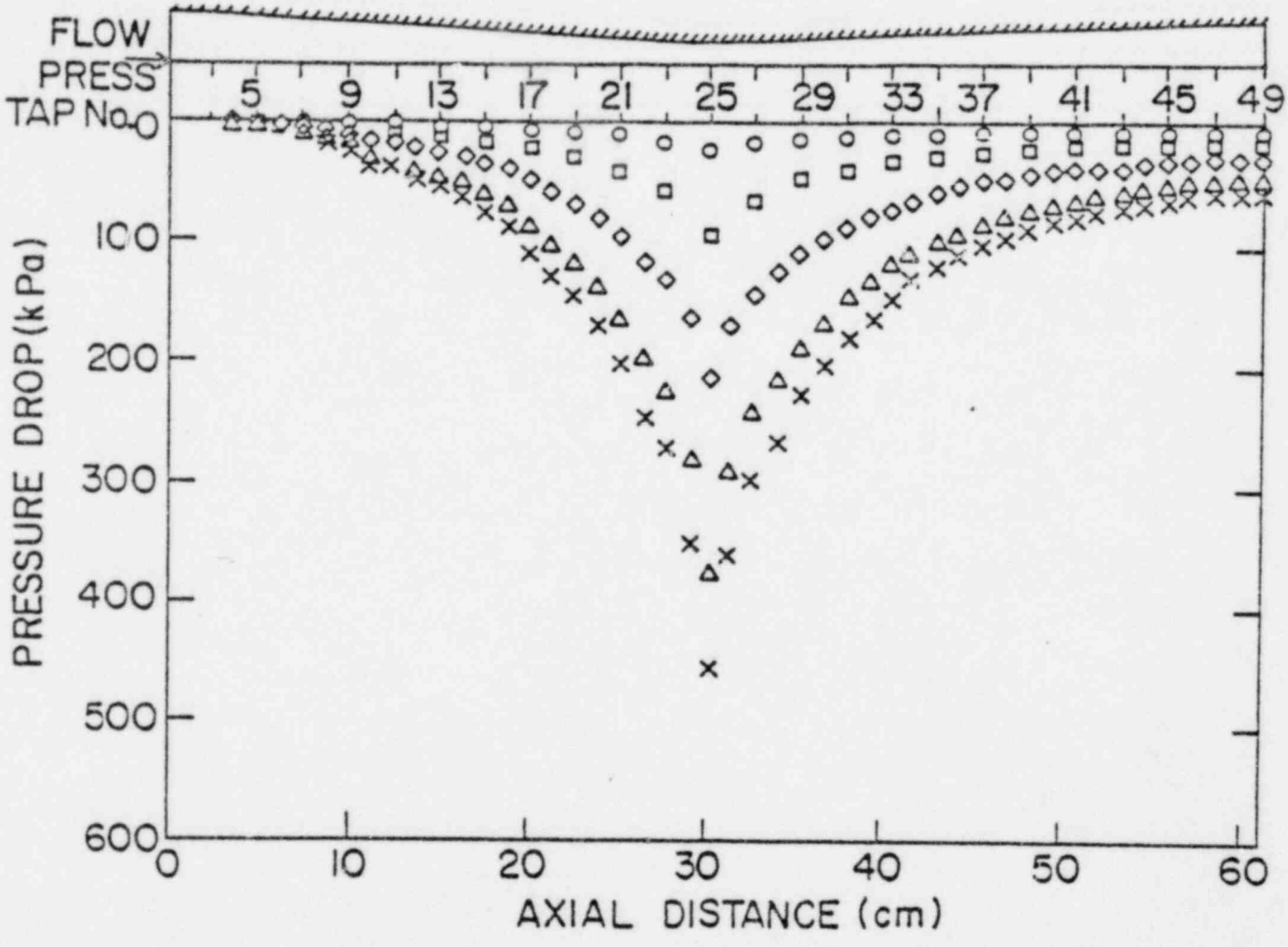

Figure 5-1 Typical Pressure Distributions Along TS-2 for the Single-Phase Flow Hydrodynamic Calibration Runs (BNL Neg. No. 3-1017-79)

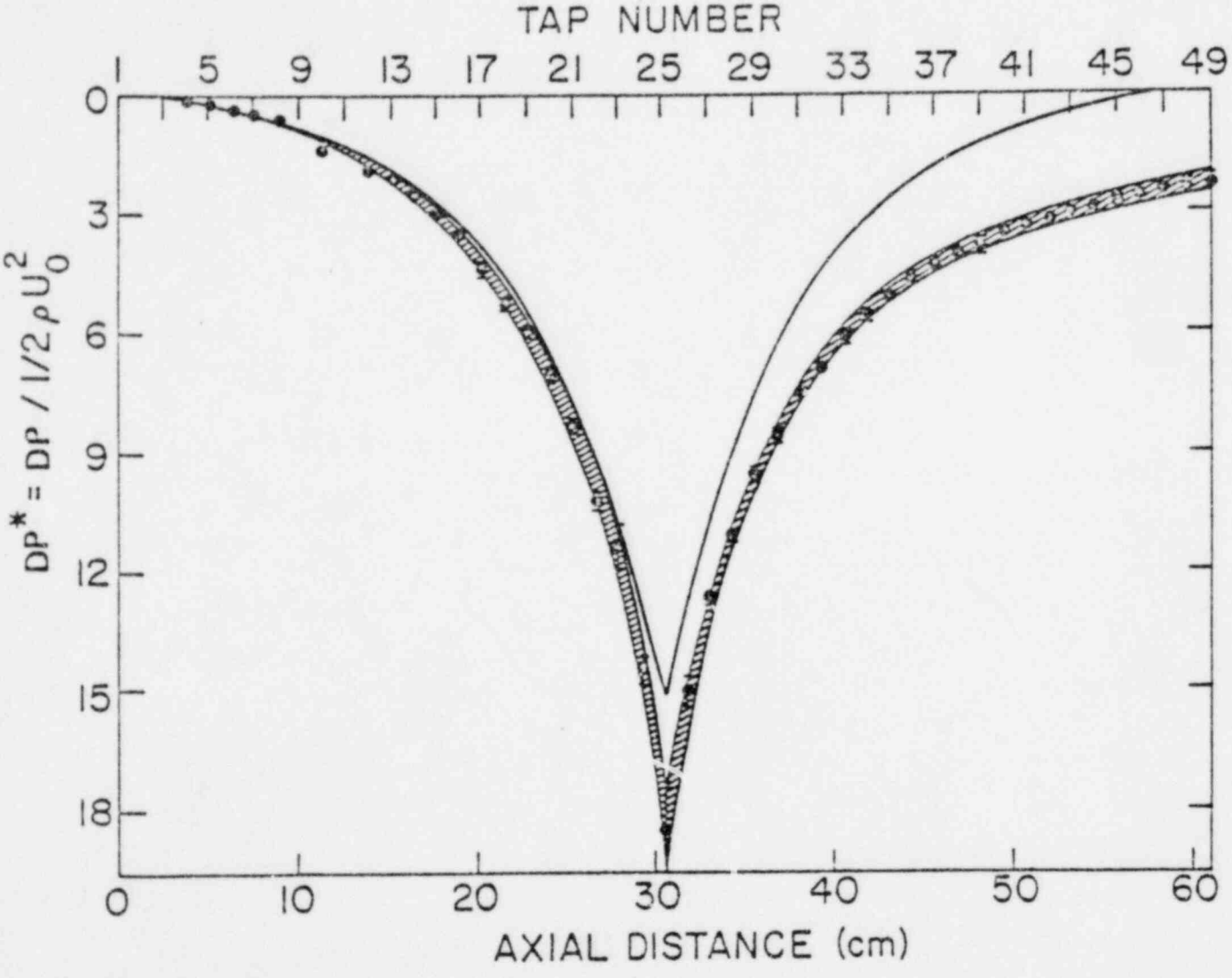

Figure 5-2 Dimensionless Pressure Distribution for TS-2. Data is Averaged for all the Hydrodynamic Calibration Runs Performed (BNL Neg. No. 3-1022-79)

5.1.2 γ-Densitometer

The calibration of the test section along the axis was performed first with the test section empty and full of water at 20°C (Table 5-2), using the single-beam γ-densitometer. Figure 5-3 presents the calibration data, as well as the calculated values (solid squares) derived from the physical measurements of wall thickness and inside diameter along the nozzle. For these calculations, the attenuation coefficients for steel was taken as $\mu_{st} = 2.7\ cm^{-1}$ and for water $\mu_w = 0.167\ cm^{-1}$, both values are listed for a 100 keV γ-energy level (Reactor Physics Constants, 1963). All calculated values were normalized to the entrance of the nozzle when the test section was empty, which provided a value of $I_o = 2854$ c/54 s. The calibrations were also repeated on different days, and the repeatability of the results are satisfactory, as long as the source decay is taken into consideration.

In Figure 5-3 the bars present the standard deviations of ten consecutive measurements. The accuracy of the system (~ 4 percent) is still governed by the statistical error $\frac{dI}{I} = \frac{I}{\sqrt{I}}$, due to the low rate of counts which in turn is caused by the low source activity. Increasing the source strength to higher activity level in the multi-beam case, improved the statistical errors by increasing the number of counts per second.

The nozzle was also calibrated while empty (full of air) at 27 axial locations with the five-beam γ-densitometer. At every axial location the five sources-detectors system was moved in 2.54 mm steps in the transverse direction to cover a total distance of 1.27 cm for each source. Figures 5-4 A, B, C, D, and E show the results of this calibration normalized with respect to the centerline value as a function of radial distance at five different

TABLE 5-2

CALIBRATION OF THE TEST SECTION BOTH EMPTY (AIR), I_E, AND FULL OF WATER, I_F. (Date 1-19-79)

AXIAL LOCATION Z(mm)	I_F counts/54s	I_E counts/54s	AXIAL LOCATION Z(mm)	I_F counts/54s	I_E counts/54s
5.1	941	2045	304.8	1239	1856
30.5	964	2053	307.2	1286	1944
55.7	976	1994	309.8	1307	2061
81.3	1019	2027	312.3	1360	2088
106.7	1017	1974	314.8	1371	2122
132.1	1110	2047	317.6	1374	2165
157.4	1125	2035	319.9	1396	2161
182.9	1147	2009	322.5	1419	2220
208.1	1206	2021	325.2	1427	2199
233.7	1260	2031	327.7	1406	2189
259.1	1260	1989	330.2	1354	2155
271.8	1328	2060	332.6	1337	2077
274.3	1337	2062	335.1	1280	2076
276.9	1341	2059	360.8	1210	2025
279.4	1313	2039	386.0	1196	2019
281.9	1338	2031	411.4	1180	2044
284.4	1352	2061	436.8	1113	2013
287.0	1366	2071	462.3	1081	1989
289.5	1378	2101	488.6	1039	2002
292.0	1367	2027	513.1	1003	2011
294.5	1355	2063	538.5	1009	2038
297.1	1338	2009	563.8	957	2082
299.6	1318	1986	576.5	961	2078
302.2	1278	1932			

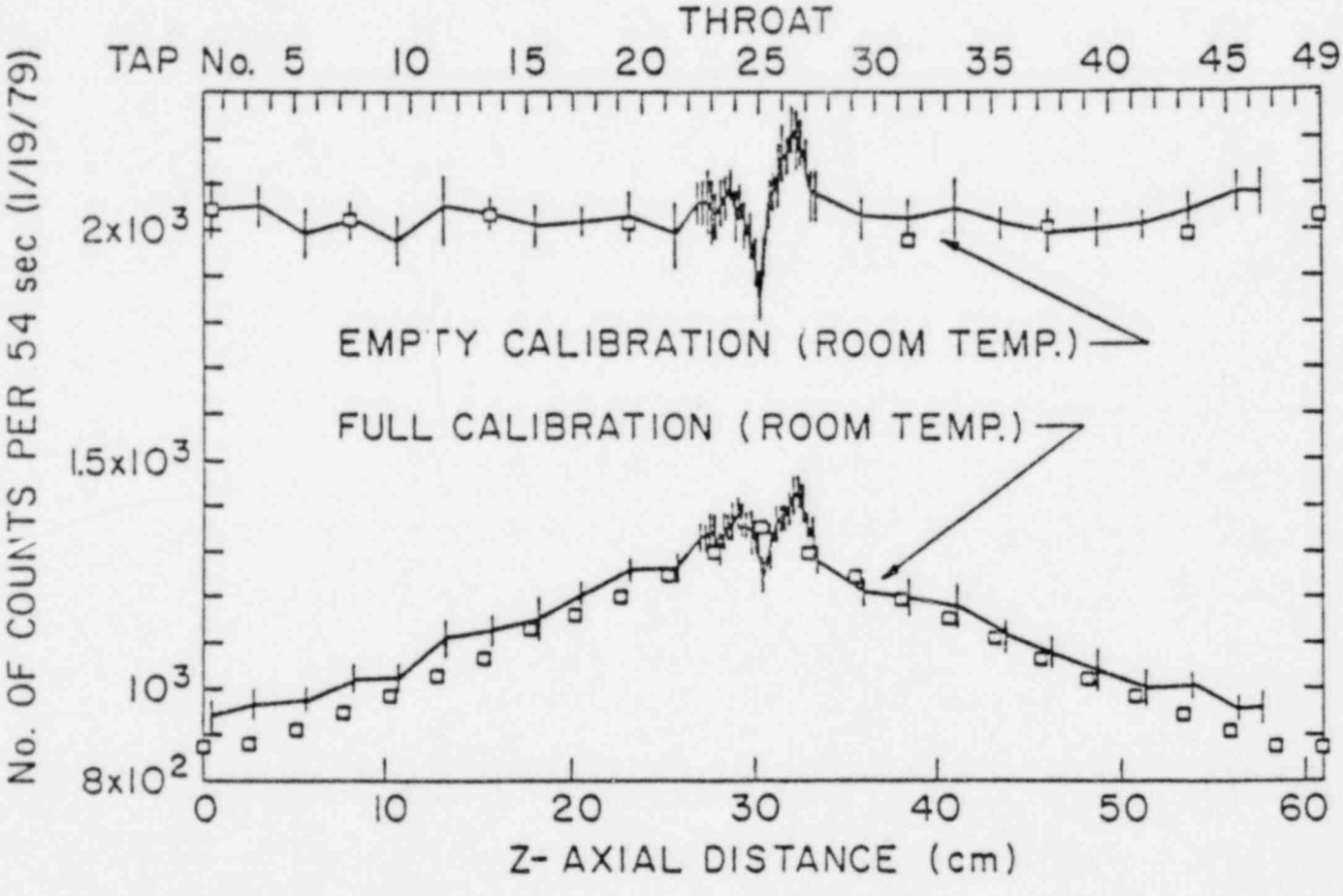

Figure 5-3 Calibration of the Test Section Both Empty (Air) and Full of Water as a Function of Axial Distance (BNL Neg. No. 3-1018-79)

axial locations. The output of each source is represented by a different symbol. The fifth and sixth measurements for each source provide a repetition of the first and second measurements of the next source. Thus, during each run there are some measurements which are repeated at the same location by two different source-detector systems. As one moves from the test section inlet to the throat, the effect of the tube radius becomes more important on the distributions. Each data point presented was an average of 10 consecutive γ-measurements of nine seconds duration each. The full calibrations of the nozzle at the same axial locations were also performed with the nozzle full of cold water (20°C), with and without the pump running to check if there were any vibration problems with the electronics. The results of the full cold (room temperature) calibration are presented in Figure 5-5 A, B, C, D and E at the same axial locations as presented in Figure 5-4. Here also the counts of the five sources were normalized by the value at the centerline. In these figure, the repeatability of the results with two consecutive sources at the same location is clearly observable. One fact to be pointed out in these calibration runs is the symmetry in the results as the sources and detectors move across the test section, both in the empty and full calibrations. Another important observation is the lack of scatter in the results and the source detector overlap repeatability.

The full calibration of the test section was also repeated while the loop was running at low flow rates and 100°C inlet temperature conditions, (Figure 5 - 6). The automatic, computer-controlled positioning of the sources included the information to calculate the linear expansion of the test section, and this information was utilized to determine the absolute location at which data were obtained. At this time, however, only the cold calibration information has been used for data reduction purposes.

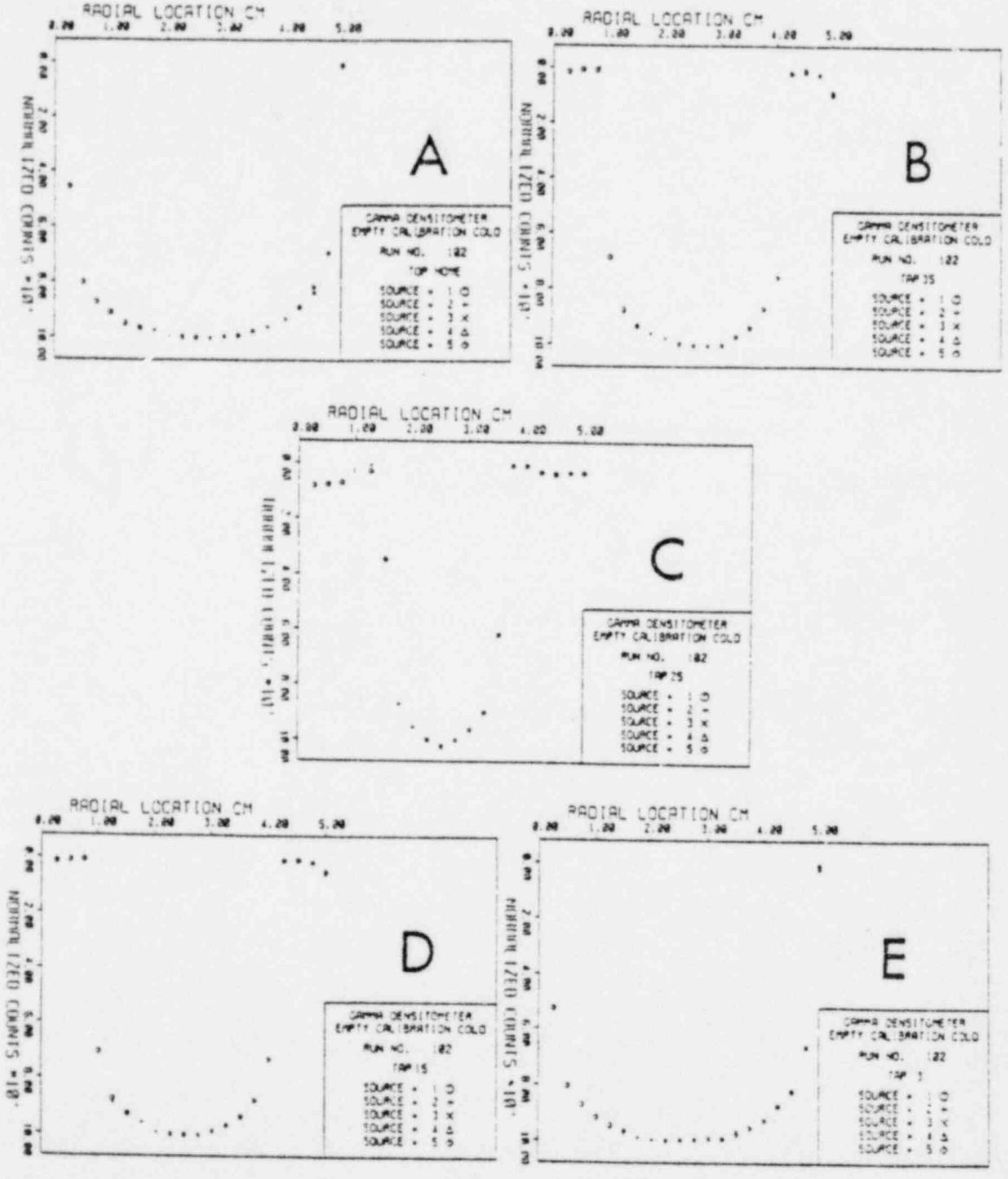

Figure 5-4 - Normalized Empty Calibrations of the Test Section at Five Different Axial Locations. (BNL Neg. No. 10-1413-79).

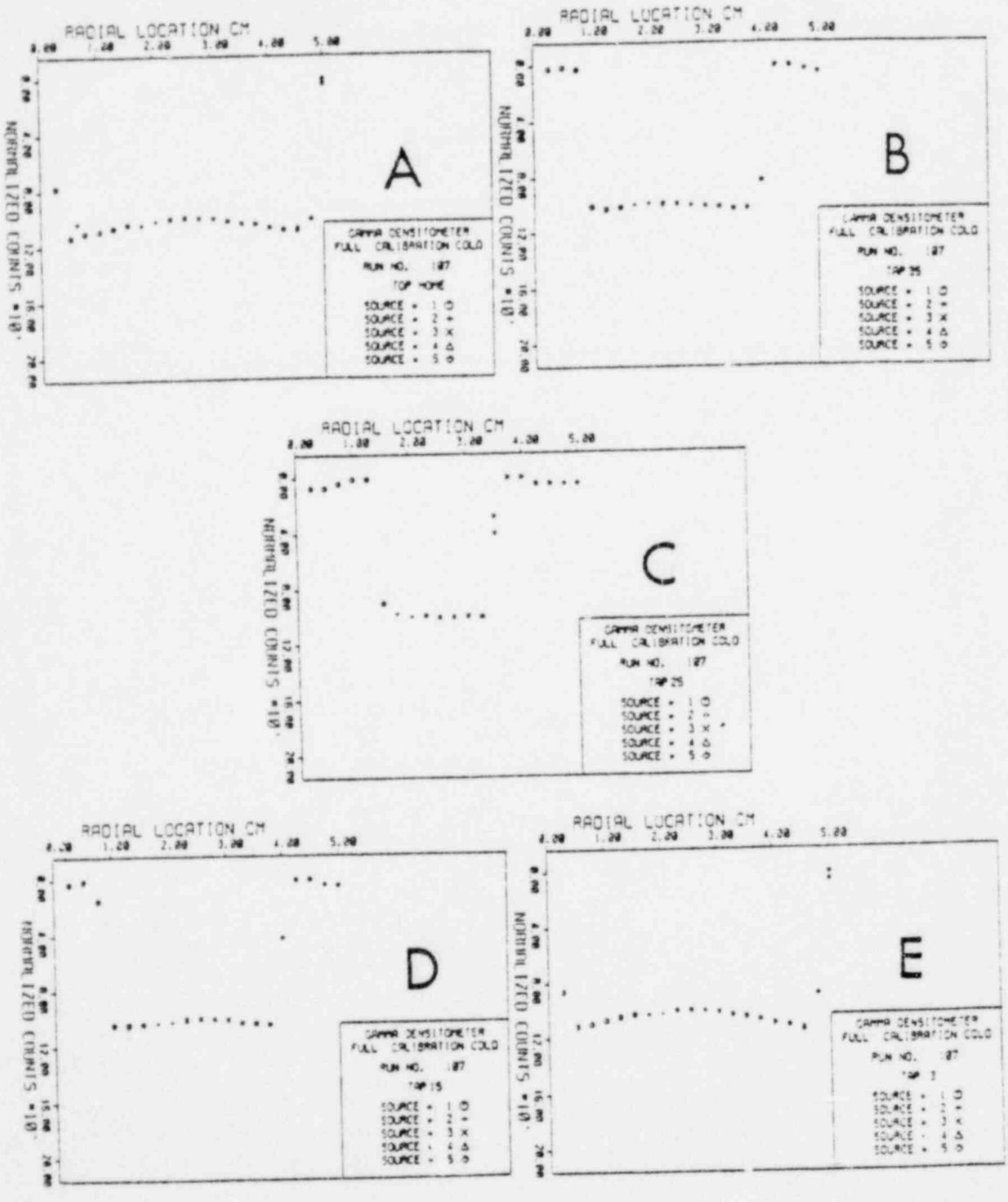

Figure 5-5 - Normalized Full Calibrations of the Test Section at Five Different Axial Locations. (BNL Neg. No. 10-1414-79).

5.2 Pressure Distributions Under Flashing Conditions

Referring to a p-T diagram such as that in Fig. 5-6, showing the equilibrium vapor pressure p_{sat} of the liquid, the isothermal expansion of the test liquid in the nozzle may be represented by a vertical line A-B. Here, point A designates the nozzle inlet condition (p_{in},T_{in}) and point B that at the throat. The distance A-B is directly related to the mass flux G through the nozzle. Thus, for a given inlet condition, the saturation line may be crossed in the expansion if G is above a certain value.

Figure 5-7 presents typical pressure distributions obtained at inlet temperature of 100°C and four flow rates. At the low mass flux, 1.81 Mg/m^2s (Run 23), very little or almost no flashing was observed at all, and the results are very similar to the single phase calibration data. At the highest mass flux, 6.01 Mg/m^2s (Run 21), the pressure is observed to drop in the converging section up to the throat and level off from there onwards in the diverging section. At intermediate mass fluxes, 4.90 Mg/m^2s (Run 20) and 5.90 Mg/m^2s (Run 28) the results show a constant pressure region downstream of the throat followed by a pressure recovery region in the diverging section of the test section. This sudden pressure increase in the diverging section is caused by a condensation region to accommodate the back pressure imposed on the system. The dimensionless form of the pressure drop data presented in Fig. 5-7 are plotted in Fig. 5-8 vs the axial distance along the test section. The observations about the pressure recovery regions in the diverging section mentioned above are more obvious in this figure. The good agreement of the low mass flux pressure distribution results with the single phase calibration curve was interpreted to mean that no vapor was present in the pressure lines after the flashing experiments.

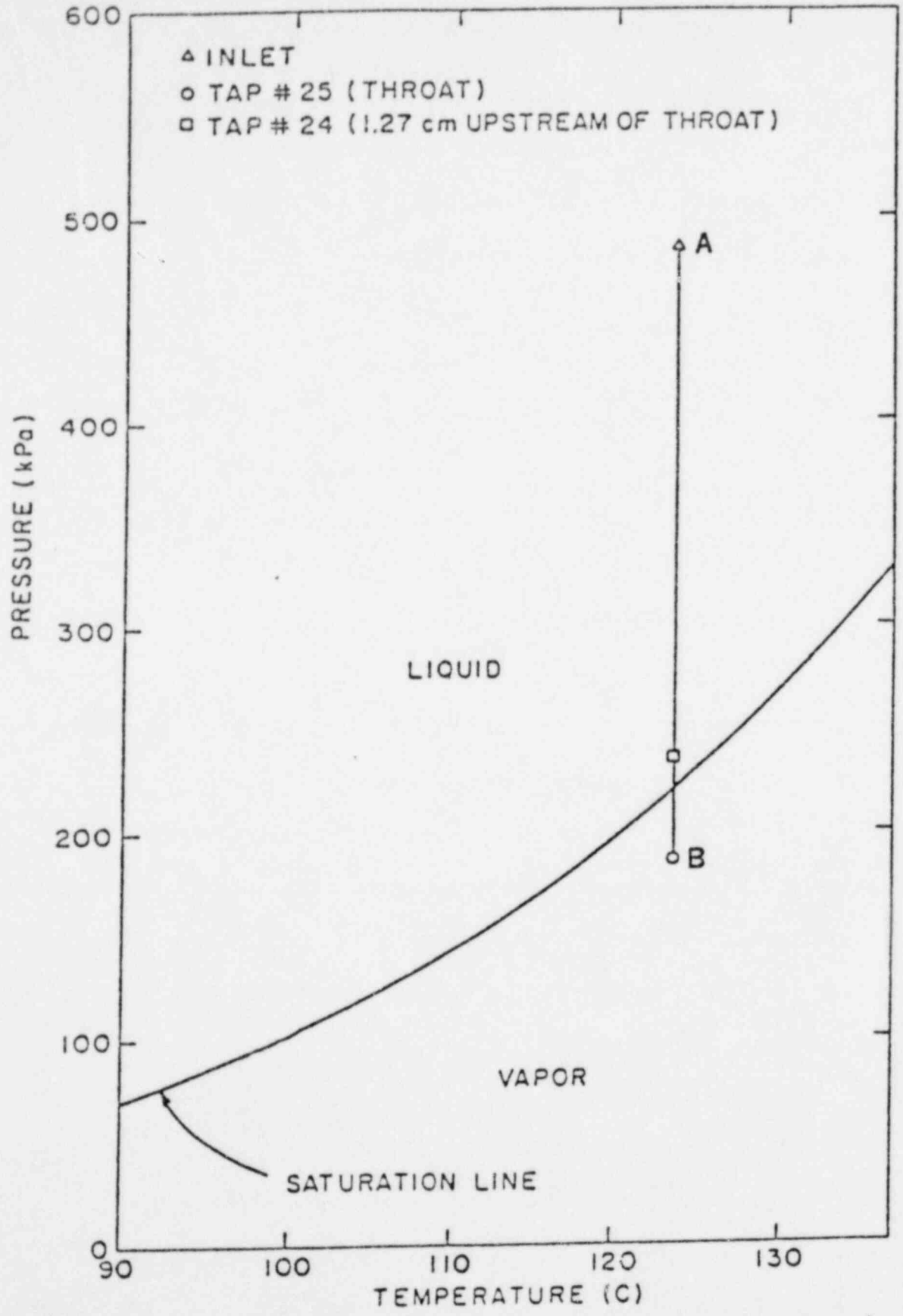

Figure 5-6 Typical Representation of an Isothermal Flashing Experiment in the p-T Diagram (BNL Neg. No. 3-1027-79)

SYMBOL	RUN	G(Mg/m^{2}s)	p_{in}(kPa)	T_{in}(C)	$p_{c.t.}$(kPa)
◇	23	1.81	130	99.4	121
□	22	3.04	170	100.2	125
△	20	4.90	281	98.3	245
○	21	6.01	393	100.6	136

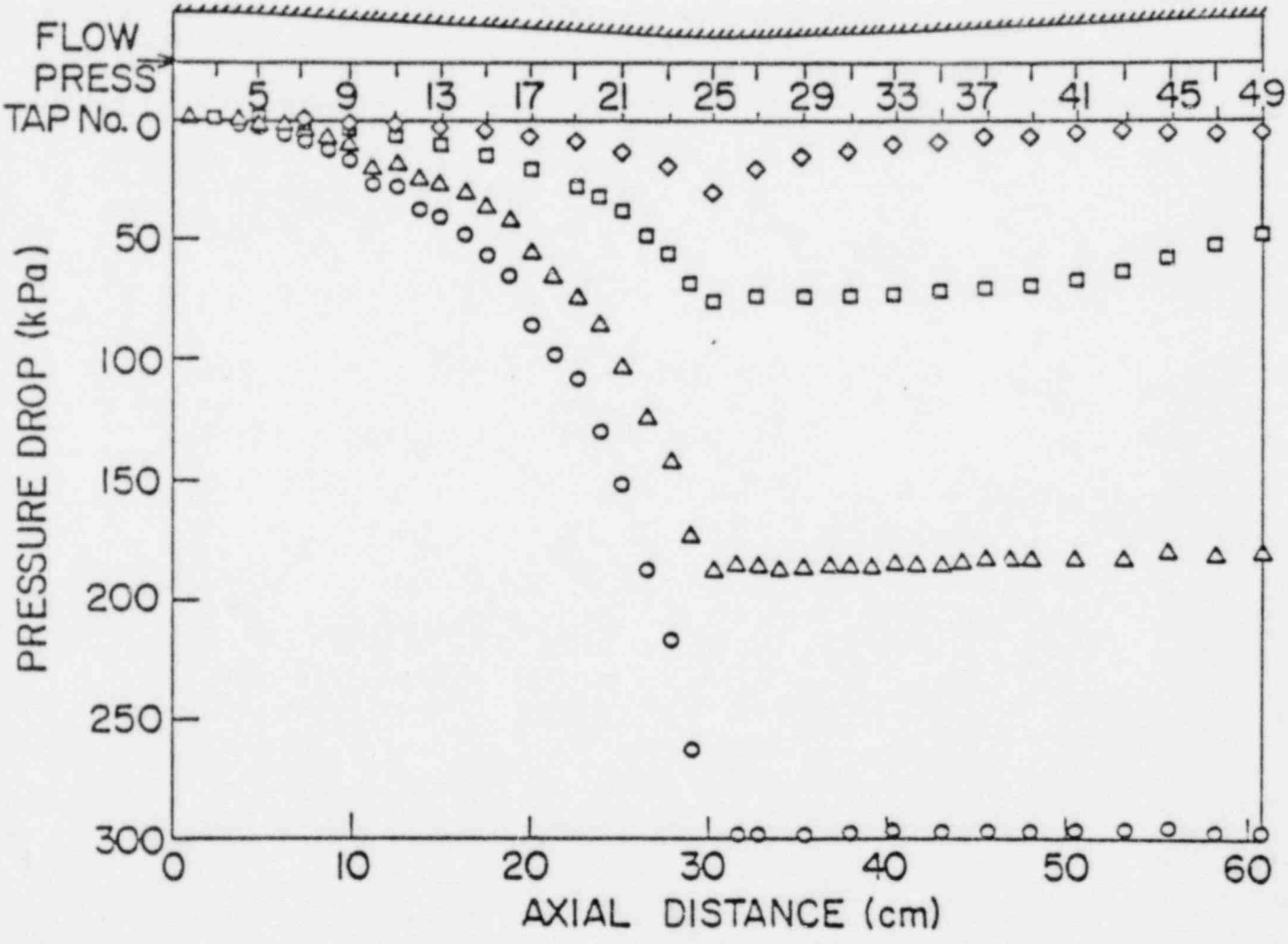

Figure 5-7 Pressure Distributions Under Flashing and Nonflashing Conditions in TS-2 (BNL Neg. No. 3-1019-79)

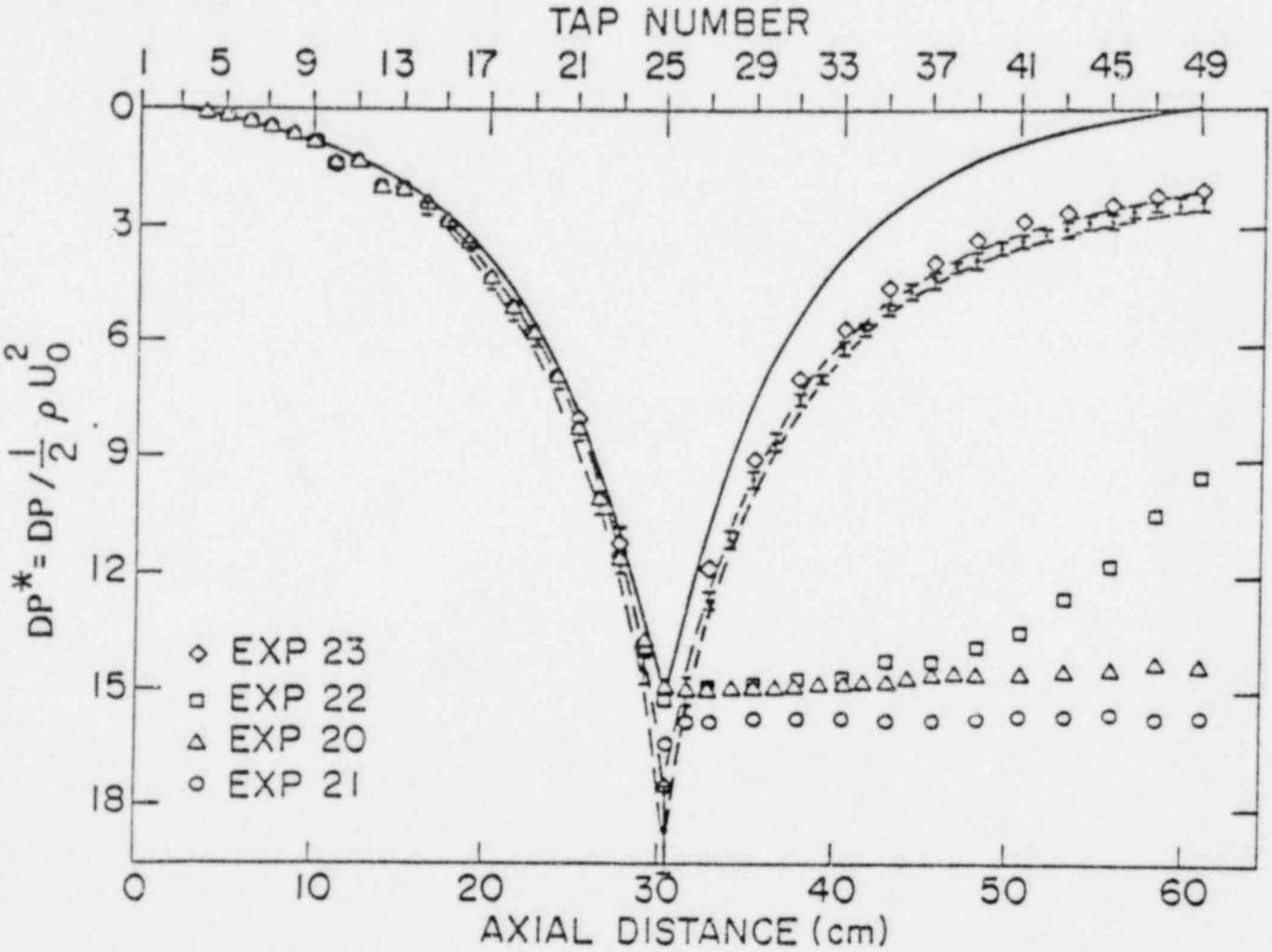

Figure 5-8 Dimensionless Pressure Distributions in TS-2 Under Flashing Conditions as Compared to Single-Phase Hydrodynamic Calibration Data (BNL Neg. No. 3-1021-79)

Similar experiments with flashing flows were also conducted at inlet temperatures of 124, 130, and 150°C for various flow rates and are tabulated in Appendix B. If one were to plot all these experiments on a p-T diagram like Fig. 5-6, it would be found that the saturation line was crossed at a location upstream and close to the throat in each experiment. Thus we concluded that in most of the experiments reported, flashing occurred at a location upstream but close to the throat. In some later experiments, the flashing front was moved well upstream of the throat.

5.2.1. Reproducibility Studies

To check the repeatability of the data, several runs were performed at nearly identical inlet conditions and flow rates. Figure 5-9 shows the comparison between the pressure distributions obtained in the two experiments for p_{in} = 168 kPa, T_{in} = 100°C, and mass flux of 3.03×10^3 kg/m^{2}sec. Experiments were also performed at a higher mass flux 4.45×10^3 kg/m^{2}sec and T_{in} = 123°C and p_{in} = 390 kPa. Figure 5-10 depicts the pressure distributions for these latter cases, i.e., Exps. 52 and 53. The results at these mass fluxes are reproducible to within 2 percent.

5.2.2. Operational Effects (Effect of Back Pressure)

In one set of experiments, flashing was initiated with the condensing tank liquid level (defined as the location of the free surface below the top of the tank) equal to zero, i.e., almost a solid loop condition. Decreasing the condensing tank liquid level, i.e., increasing the size of the steam cavity in the condensing tank, changed the downstream (condensing tank) pressure and affected the flashing conditions and pressure distriubutions

RUN	G(Mg/m^2s)	p_{in}(kPa)	T_{in}(C)	$p_{c.t.}$(kPa)
22	3.04	170	100.2	125
40	3.02	168	100.3	112

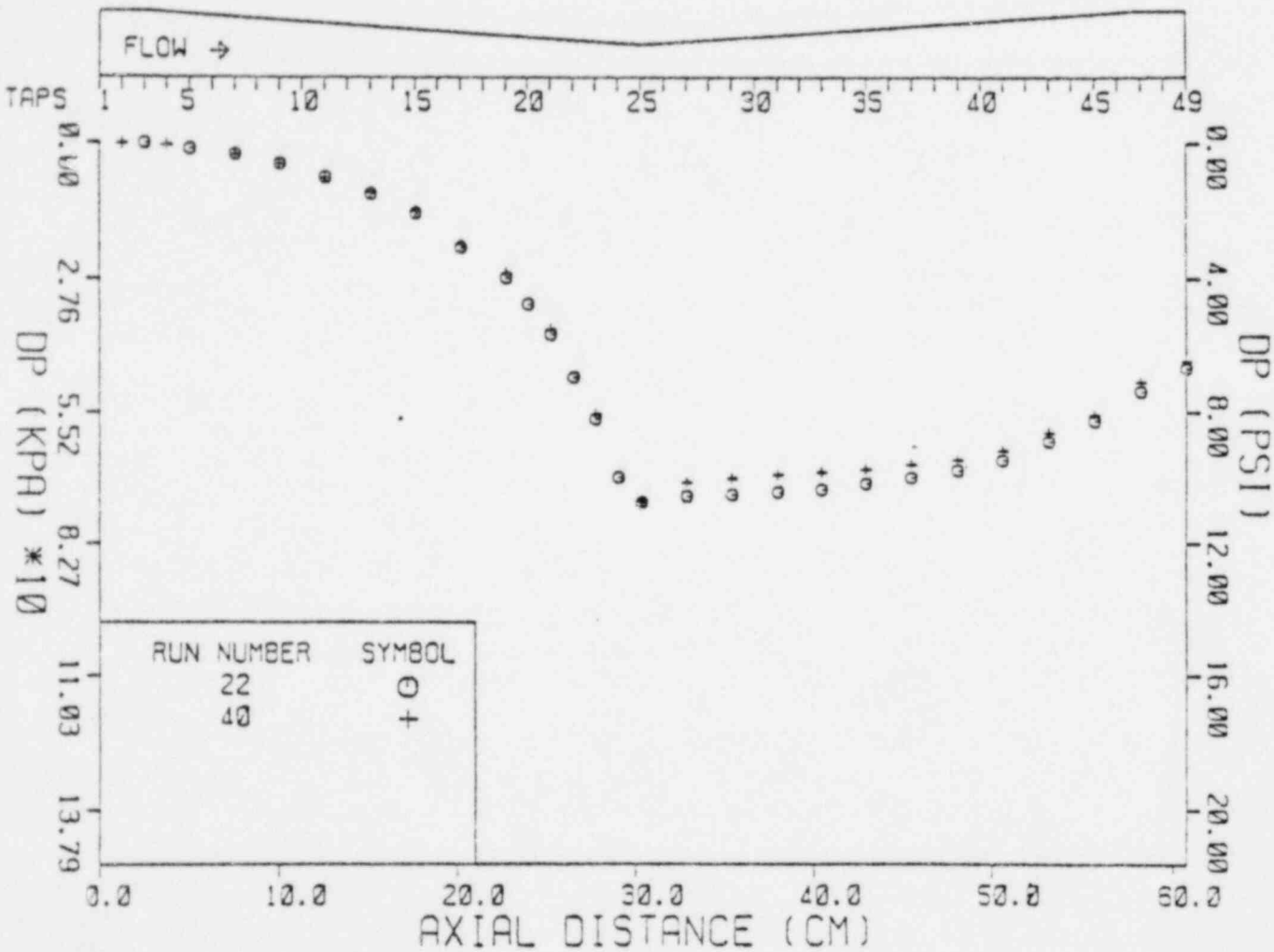

Figure 5-9 Comparison of Pressure Distribution in Two Experiments to Show the Reproduciblity of the Results at Low Mass Fluxes, G = 3.03 Mg/m^2s (BNL Neg. No. 3-1029-79)

RUN	G(Mg/m^{2}s)	p_{in}(kPa)	T_{in}(C)	$p_{c.t.}$(kPa)
52	4.48	381	123.5	254
53	4.45	395	123.6	249

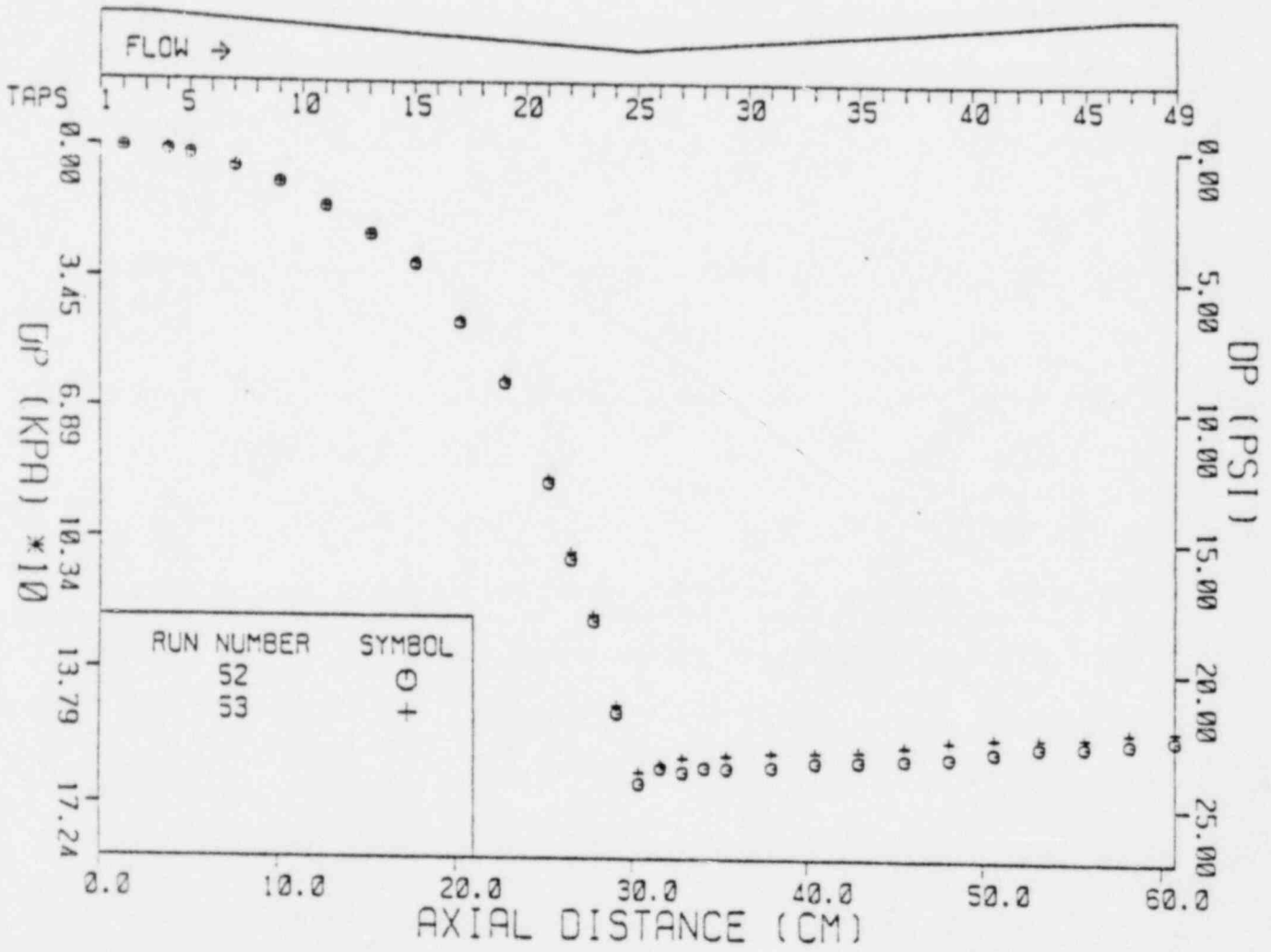

Figure 5-10 Comparison of Pressure Distributions in Two Experiments to Show Reproducibility of the Results at High Mass Flux, G = 4.45 Mg/m^{2}s (BNL Neg. No. 3-1028-79)

although the flow rate and inlet conditions were held constant. Figure 5-11 depicts the pressure distribution results for these experiments, Runs 35, 37, and 43. The pressure distributions in the converging section and mass flux are observed to be independent of the downstream pressure, which imply that the flow is choked. Run 35 depicts the above-mentioned constant pressure region downstream of the throat followed by a sudden pressure rise, which seems to correspond to a condensation region as previously described. Runs 37 and 43 are almost identical although the condensing tank pressure is lower in Run 43.

The photographic observations performed during these experiments are presented in Fig. 5-12. For Run 35, the bubble sizes are minute, and their number density is very large. Decreasing the back pressure increases the vapor generated in Runs 37 and 43. During Run 43, the windows were covered with a water film, and the interior of the tube was invisible. This drastic difference in observed appearance between Runs 37 and 43, does not noticeably affect the pressure distributions presented in Fig. 5-11.

5.2.3. Parametric Effects

The effects of the flow parameters, i.e., inlet pressure, p_{in}, inlet temperature, T_{in}, and mass flux, G, in the flashing regimes and pressure distributions were also investigated and will be presented below. Figure 5-13 presents the results when p_{in} and T_{in} were kept constant and the mass flux was varied close to conditions of flashing onset in the nozzle. This is equivalent to lengthening or shortening the line A-B in Fig. 5-6, moving the point B near the p_{sat} curve. The pressure distribution in the converging part follows very closely the single phase calibration. Downstream of the throat the vapor generation manifests itself as a deviation in

RUN	G(Mg/m^{2}s)	p_{in}(kPa)	T_{in}(C)	$p_{c.t.}$(kPa)
35	4.96	287	99.4	250
37	4.94	296	100.3	170
43	4.97	287	100.2	120

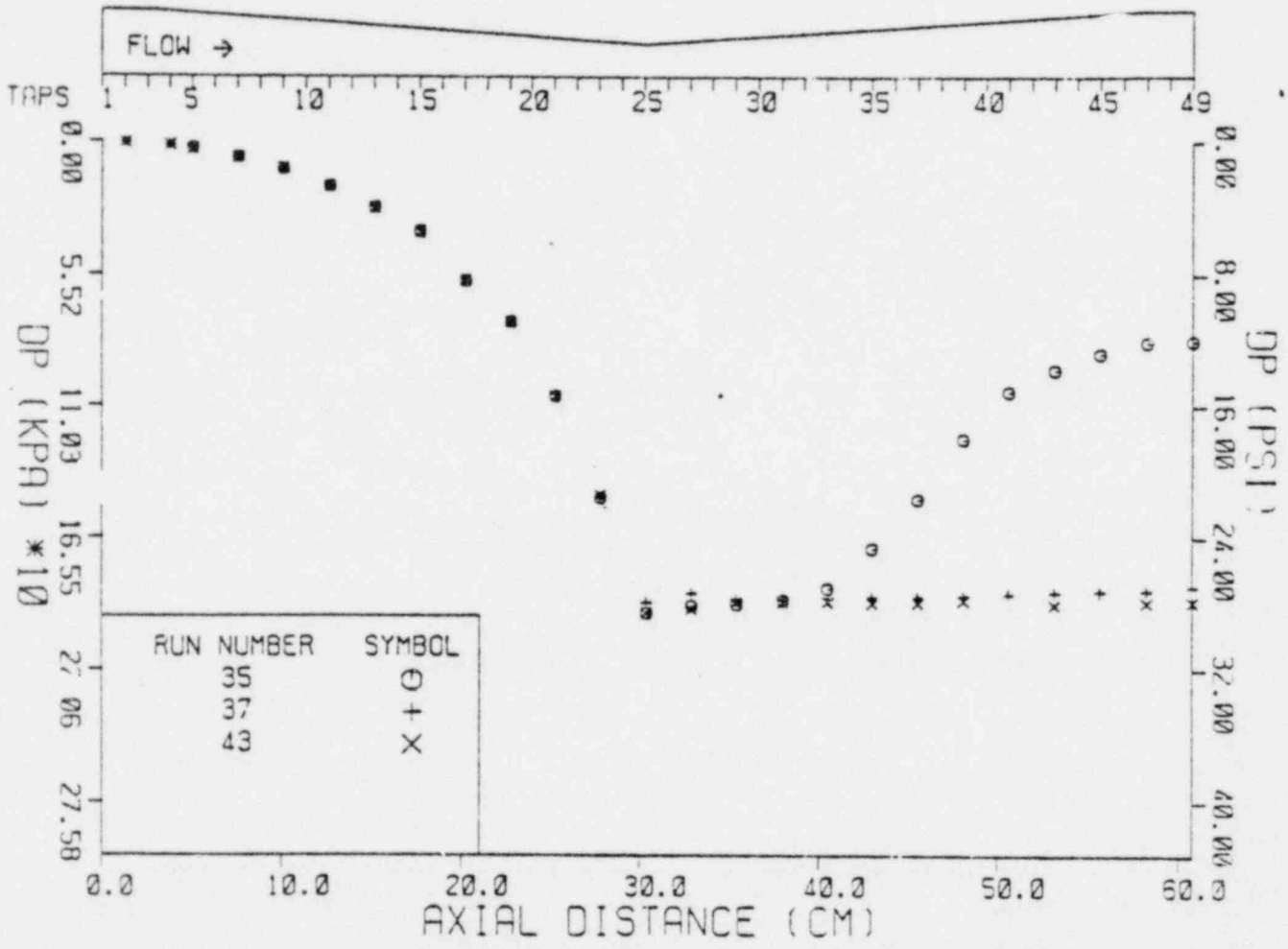

Figure 5-11 Pressure Distributions Showing the Effect of Condensing Tank Back Pressure for Identical Nozzle Inlet Conditions (BNL Neg. No. 3-1031-79)

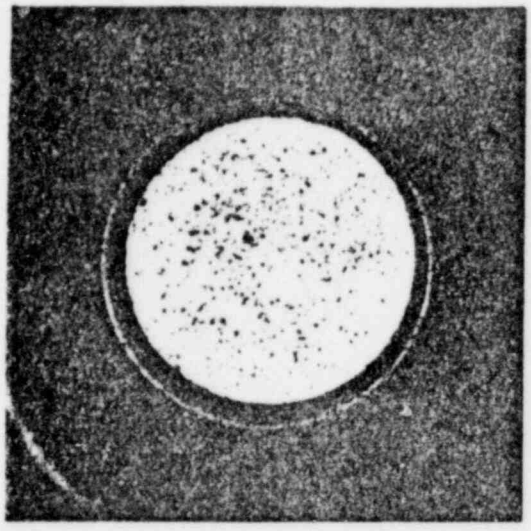

A. RUN NO. 35

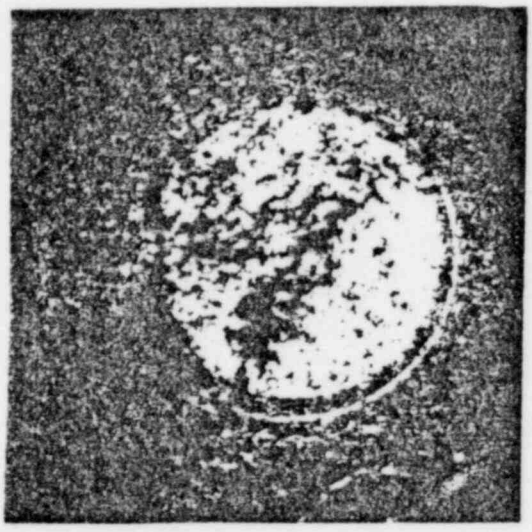

B. RUN NO. 37

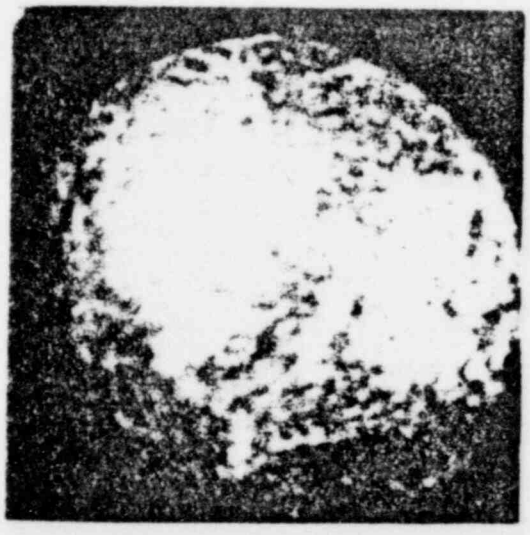

C. RUN NO. 43

SCALE 1:1

Figure 5-12 Photographic Observations for the Experimental Conditions Presented in Fig. 5-11. In these and all the following photographs, the diameter of both the front and rear windows is 50 mm. (BNL Neg. No. 1-919-79).

RUN	G(Mg/m^2s)	p_{in}(kPa)	T_{in}(C)	$p_{c.t.}$(kPa)
49	2.27	146	99.9	99
50	2.04	142	99.8	101

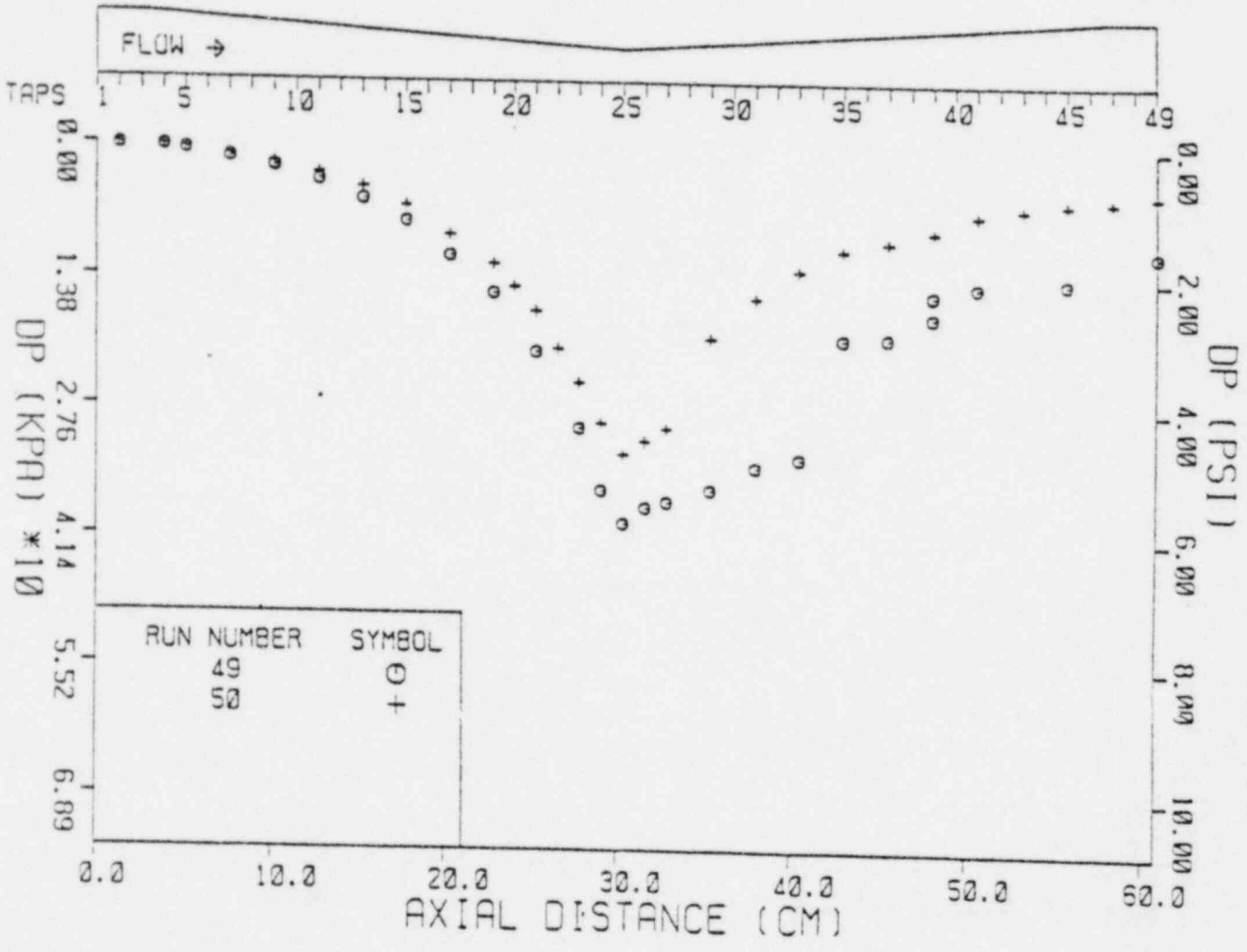

Figure 5-13 Effect of Mass Flux on Pressure Distributions for Identical Nozzle Inlet Conditions Which are Close to the Onset of Flashing in the Test Section (BNL Neg. No. 3-1032-79).

the pressure distribution. This region is followed by a pressure increase caused by the sudden collapse of the bubbles and followed by a pressure recovery zone typical of single phase flows in divergent pipes. Figure 5-14 depicts the photographic observations for these two cases. Although the appearance of the bubbles was found to be intermittent, this fact was not apparent in the pressure measurements due to the time response of our pressure manifolds and to our long averaging times. In Fig. 5-15, we present the typical effect of a more substantial change in mass flux for an inlet temperature of 123°C and an inlet pressure of 260 kPa. At a mass flux of 2.04 Mg/m^2s (Run 57), one observes the onset of flashing, which intensified to violent flashing at a mass flux of 2.98 Mg/m^2s (Run 61). The corresponding photographic observations are presented in Fig. 5-16. .

The effect of changing the inlet temperature from 100 to 150 °C was also investigated while maintaining a fixed initial overpressure, $p_{in} - p_{sat}(T_{in})$. This corresponds to moving the point A parallel to the saturation curve p_{sat} in Fig. 5-6 and keeping the mass flux unchanged. For constant values of the pressure difference between the inlet pressure and the saturation pressure at the inlet temperature, i.e., $p_{in} - p_{sat}(T_{in})$, the effect of inlet temperature on the pressure distributions was not very pronounced for the various flashing experiments. This behavior was to be expected, since the driving potential, i.e., $(p - p_{sat})$ was not changed in these runs. Figure 5-17 represents these results for Exp. 67 (T_{in} = 149.2°C, p_{in} = 503.3 kPa) Exp. 56 (T_{in} = 123.5°C, p_{in} = 136.5 kPa) and Exp. 39, while the mass flux is 2.20×10^3 kg/m^2sec for the experimental conditions close to the onset of flashing. The photographic observations for Exps. 39 and 56 are presented in Fig. 5-18. . One observes that the effect of inlet temperature is small as long as the inlet pressure is adjusted for constant subcooling at the inlet. The same observation will be valid for the following results. Figures 5-19, 5-20, and 5-21 show similar results for progressively higher mass fluxes, and Fig. 5-22 show

SCALE 1:1

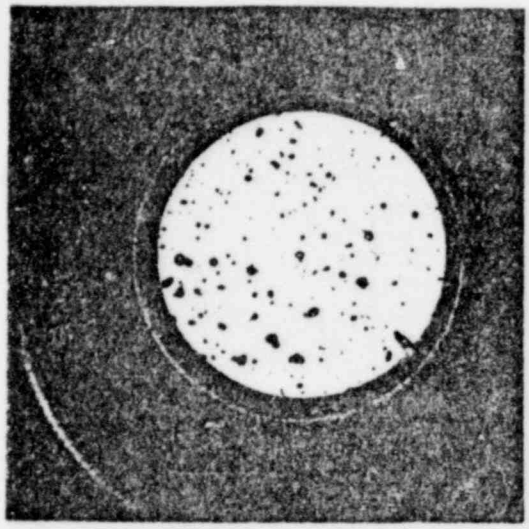

RUN NO. 49

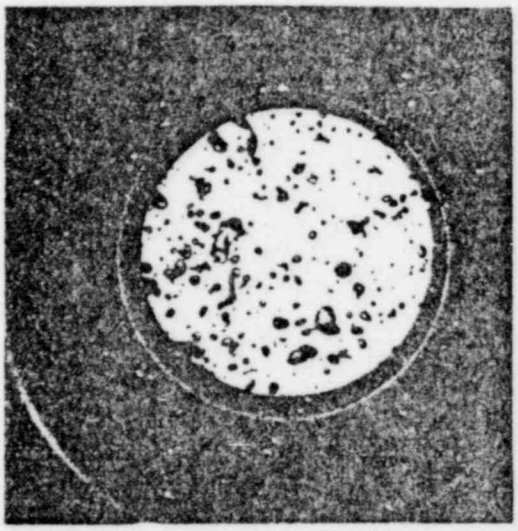

RUN NO. 49

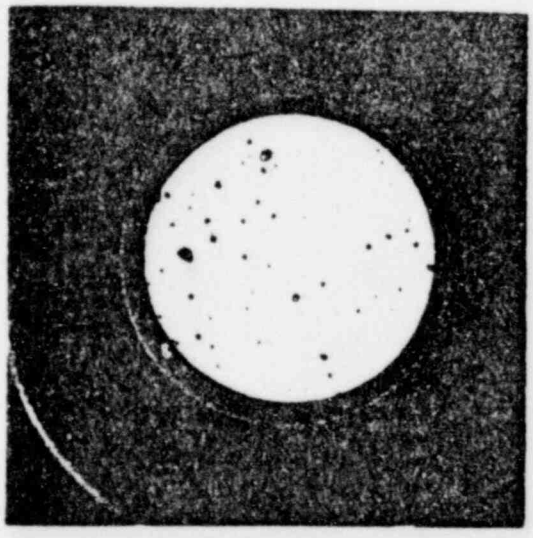

RUN NO. 50

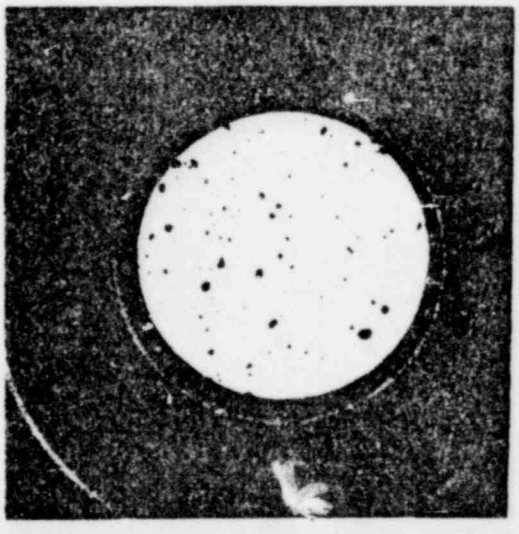

RUN NO. 50

Figure 5-14 Photographic Observations for the Experimental Conditions Presented in Fig. 5-13 (BNL Neg. No. 1-922-79).

RUN	G(Mg/m^{2}s)	p_{in}(kPa)	T_{in}(C)	$p_{c.t.}$(kPa)
57	2.04	263	124.7	256
58	2.98	254	123.3	174
61	2.98	259	123.8	162

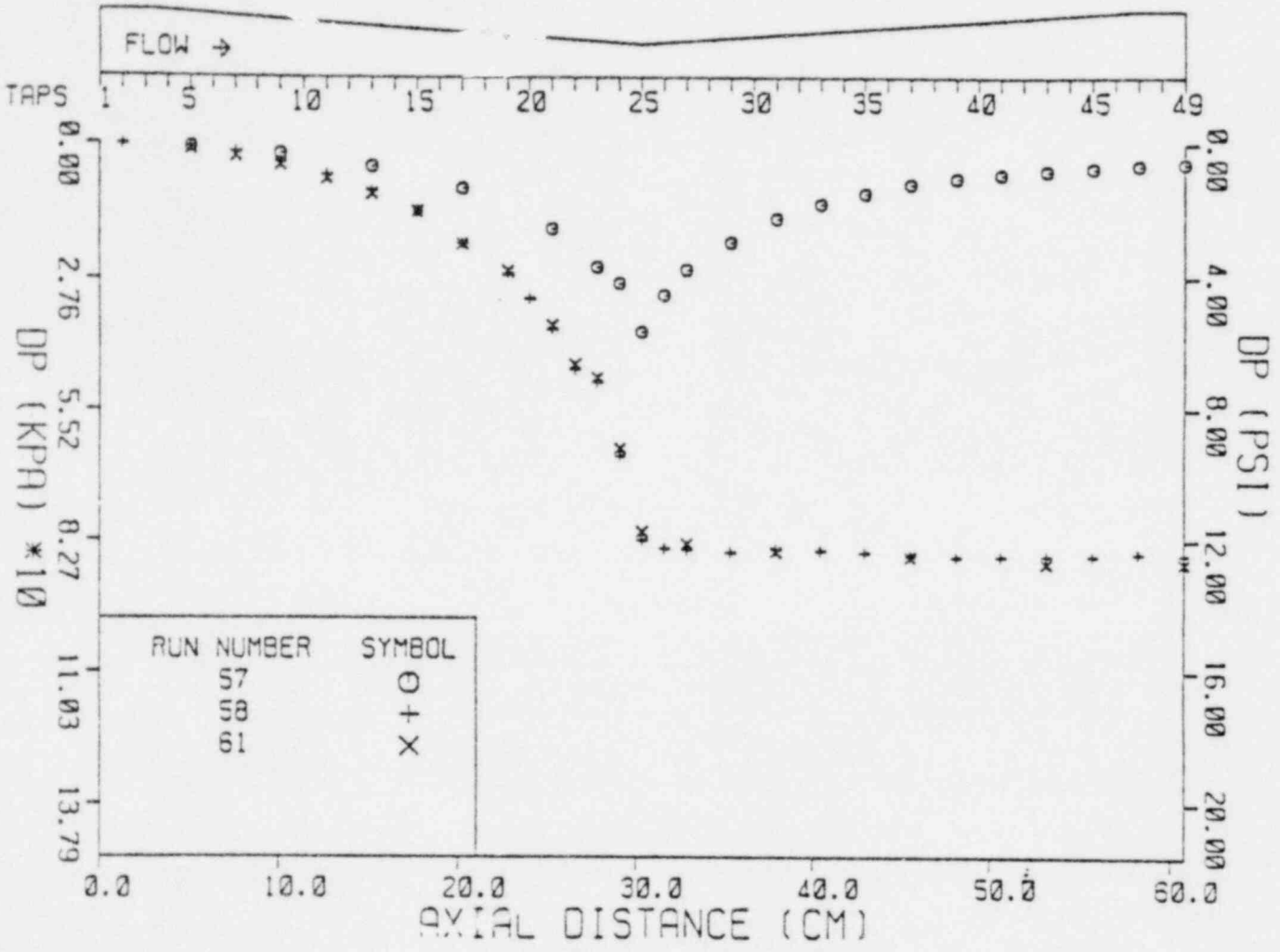

Figure 5-15 Effect of Mass Flux on the Pressure Distributions in the Test Section (BNL Neg. No. 3-1033-79)

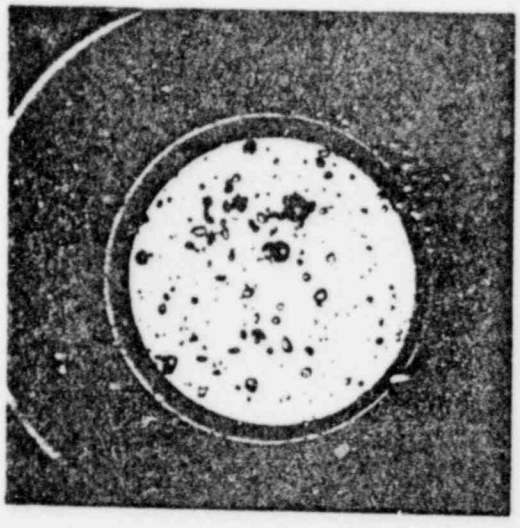

RUN NO. 57

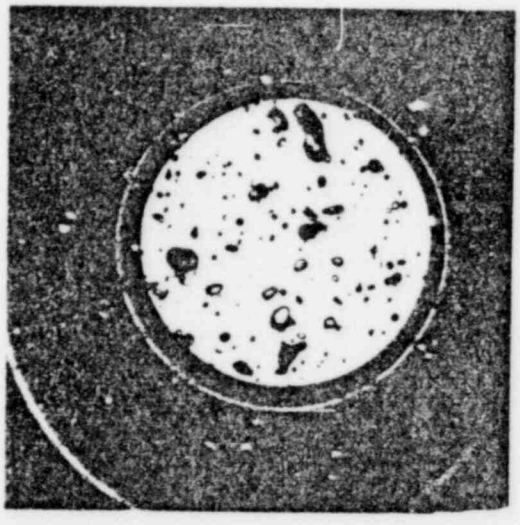

RUN NO. 57

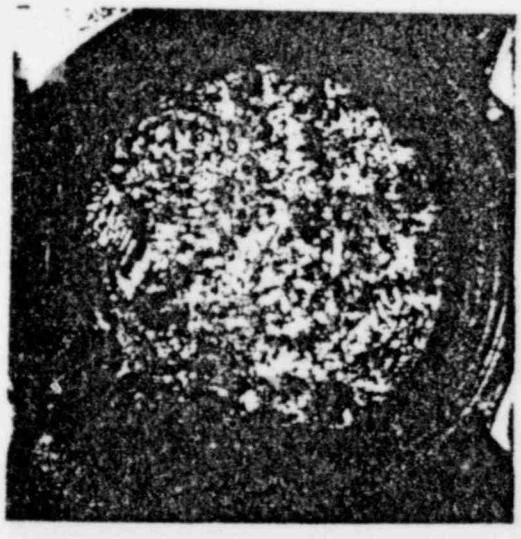

RUN NO. 61

SCALE 1:1

Figure 5-16 Photographic Observations for the Experimental Conditions Presented in Fig. 5-15 (BNL Neg. No. 1-918-79).

RUN	$G(Mg/m^2s)$	p_{in}(kPa)	T_{in}(C)	$p_{c.t.}$(kPa)
67	2.22	502	148.6	463
56	2.20	261	123.2	252
39	2.25	136	100.5	112

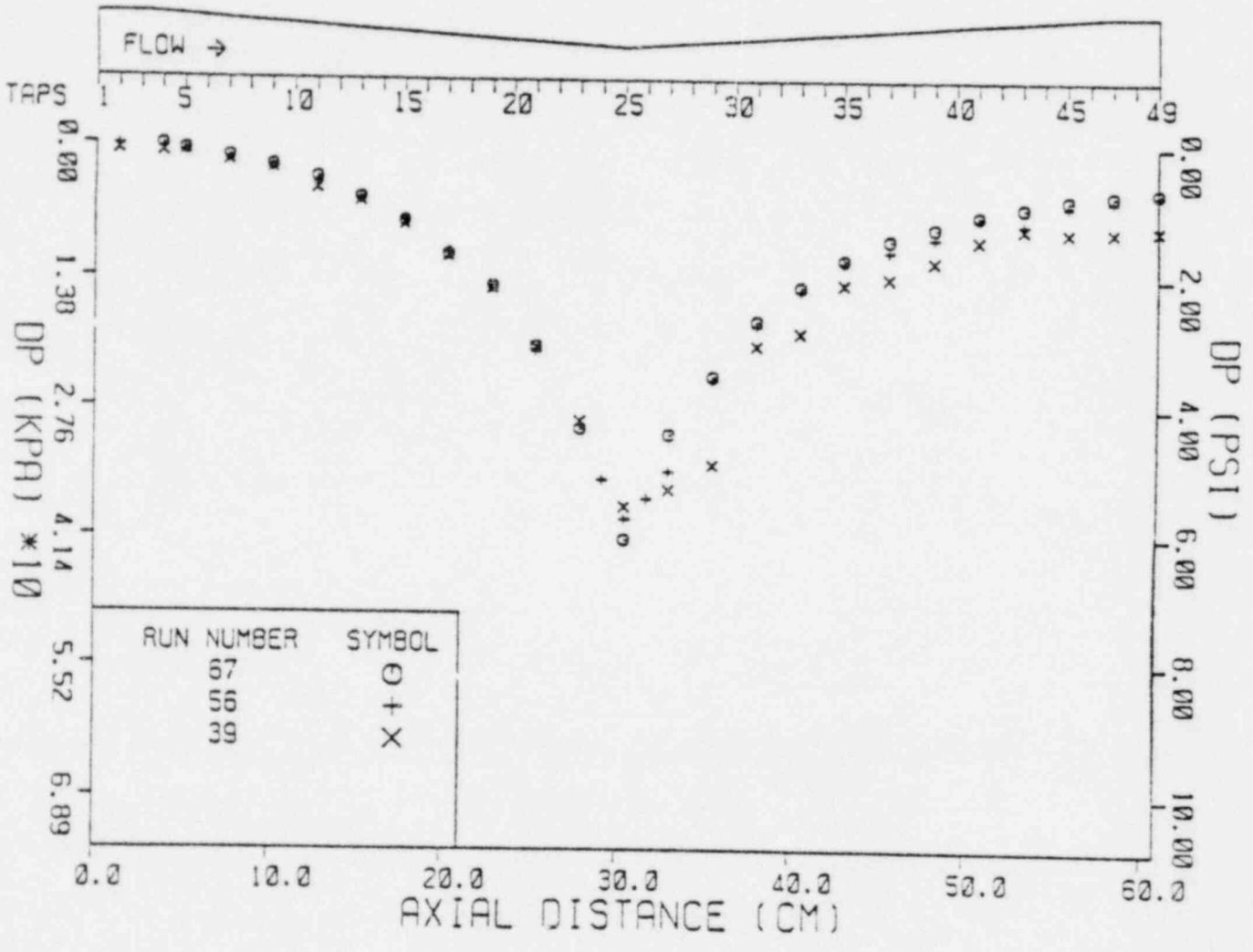

Figure 5-17 Effect of Nozzle Inlet Temperature at Constant ($p_{in} - p_{sat}(T_{in})$) on the Pressure Distribution in the Test Section (BNL Neg. No. 3-1030-79).

SCALE 1:1

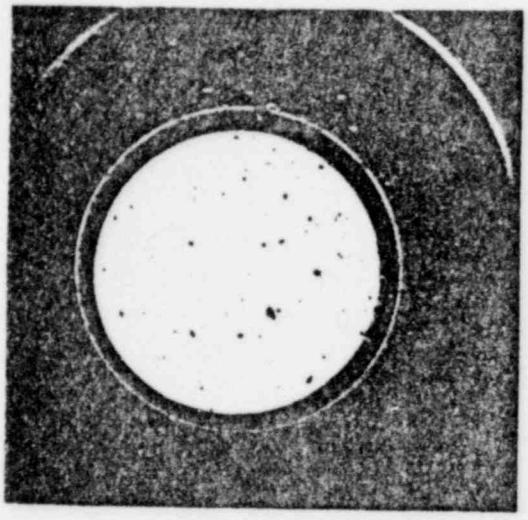

RUN NO. 56

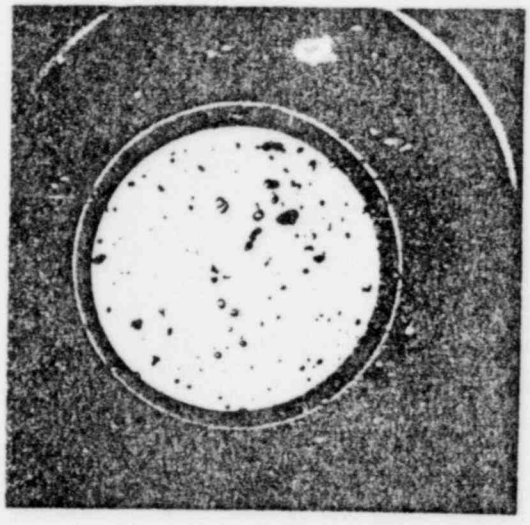

RUN NO. 56

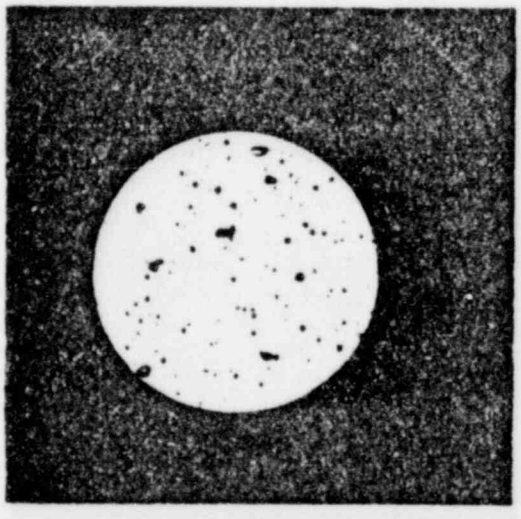

RUN NO. 39

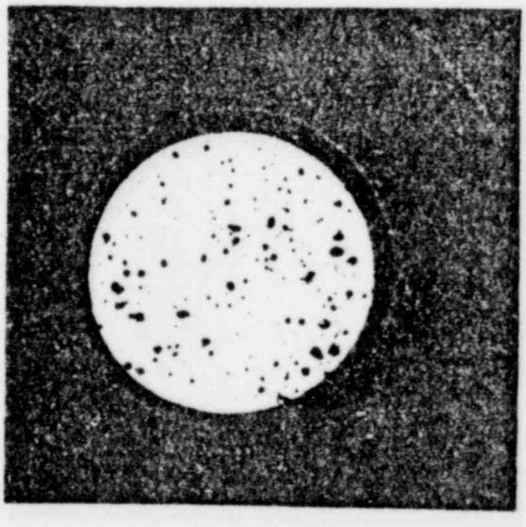

RUN NO. 39

Figure 5-18 Photographic Observations for Experimental Conditions Presented in Fig. 5-17 (BNL Neg. No. 1-921-79).

RUN	G(Mg/m^{2}s)	p_{in}(kPa)	T_{in}(C)	$p_{c.t.}$(kPa)
66	2.94	521	148.8	463
55	2.99	293	123.6	251
27	2.95	326	130.0	299

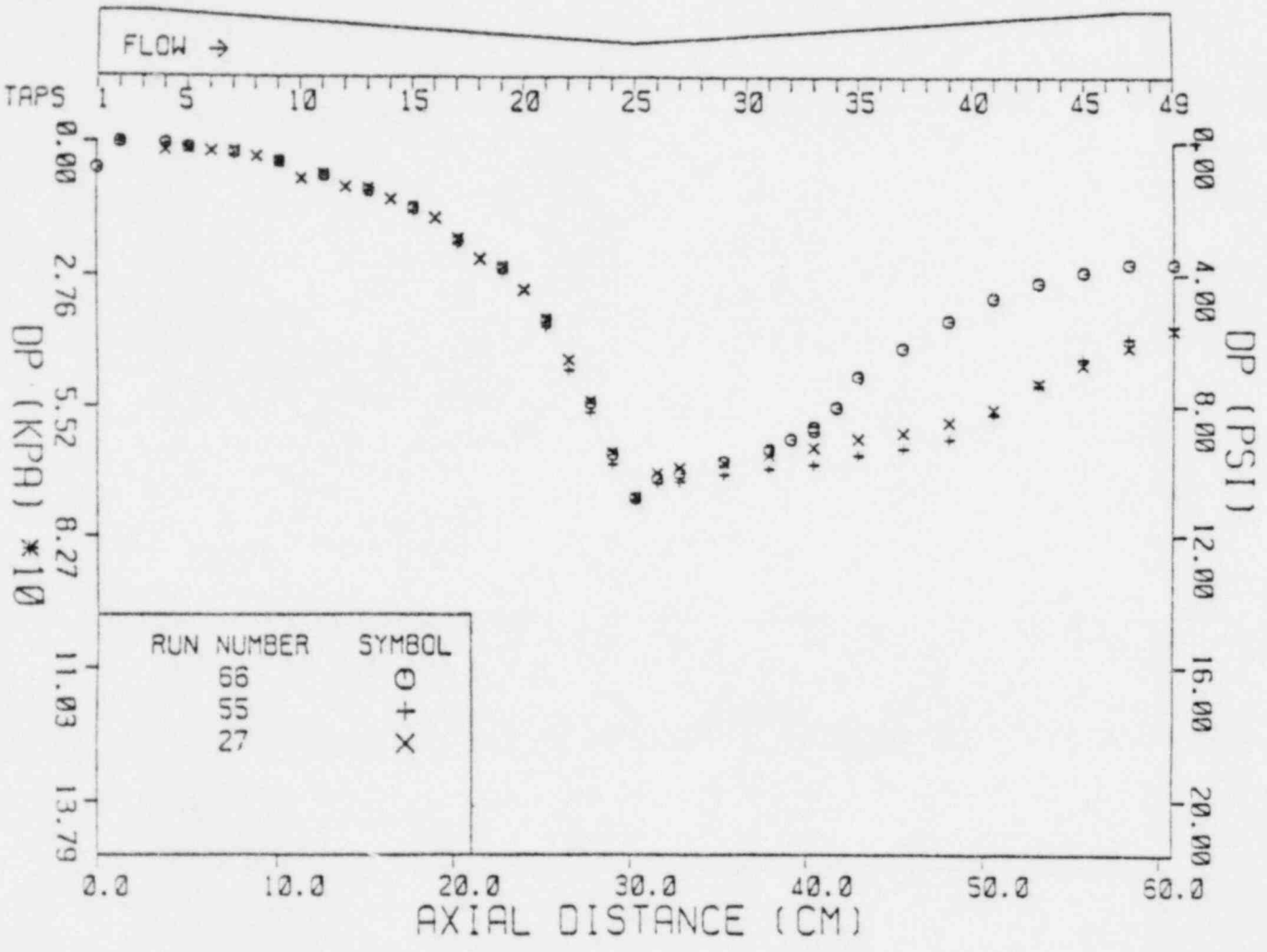

Figure 5-19 Effect of Nozzle Inlet Temperature at Constant (p_{in} - p_{sat}(T_{in})) on the Pressure Distribution in the Nozzle (BNL Neg. No. 3-1037-79).

RUN	G(Mg/m^{2}s)	p_{in}(kPa)	T_{in}(C)	$p_{c.t.}$(kPa)
22	3.04	170	100.2	125
24	3.05	160	98	122

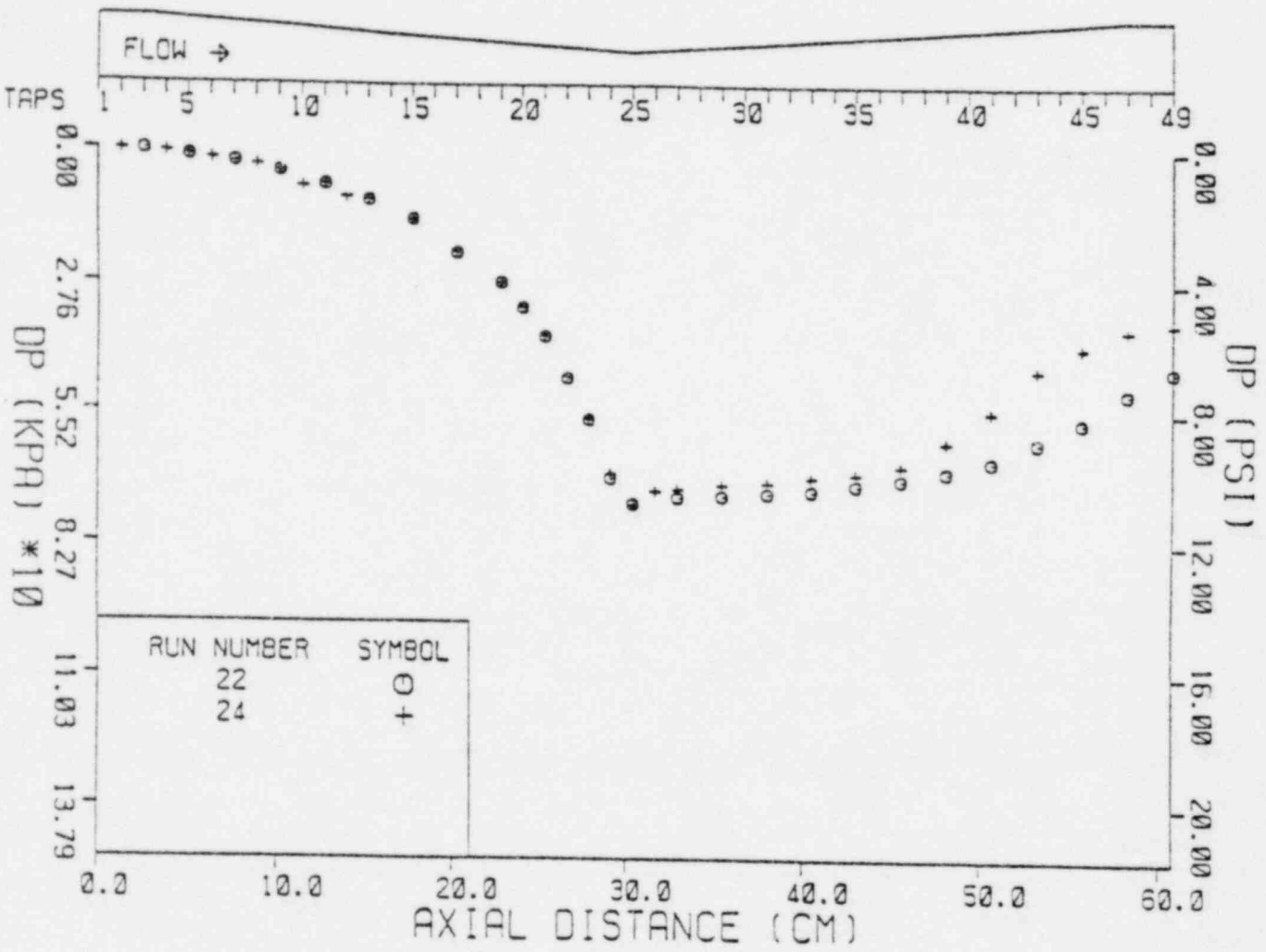

Figure 5-20 Effect of Nozzle Inlet Temperature at Constant $[p_{in} - p_{sat}(T_{in})]$ on the Pressure Distribution in the Nozzle (BNL Neg. No. 3-1035-79).

RUN	G(Mg/m^{2}s)	p_{in}(kPa)	T_{in}(C)	$p_{c.t.}$(kPa)
44	4.50	271	99.9	101
52	4.48	381	123.5	254
64	4.40	609	148.8	463

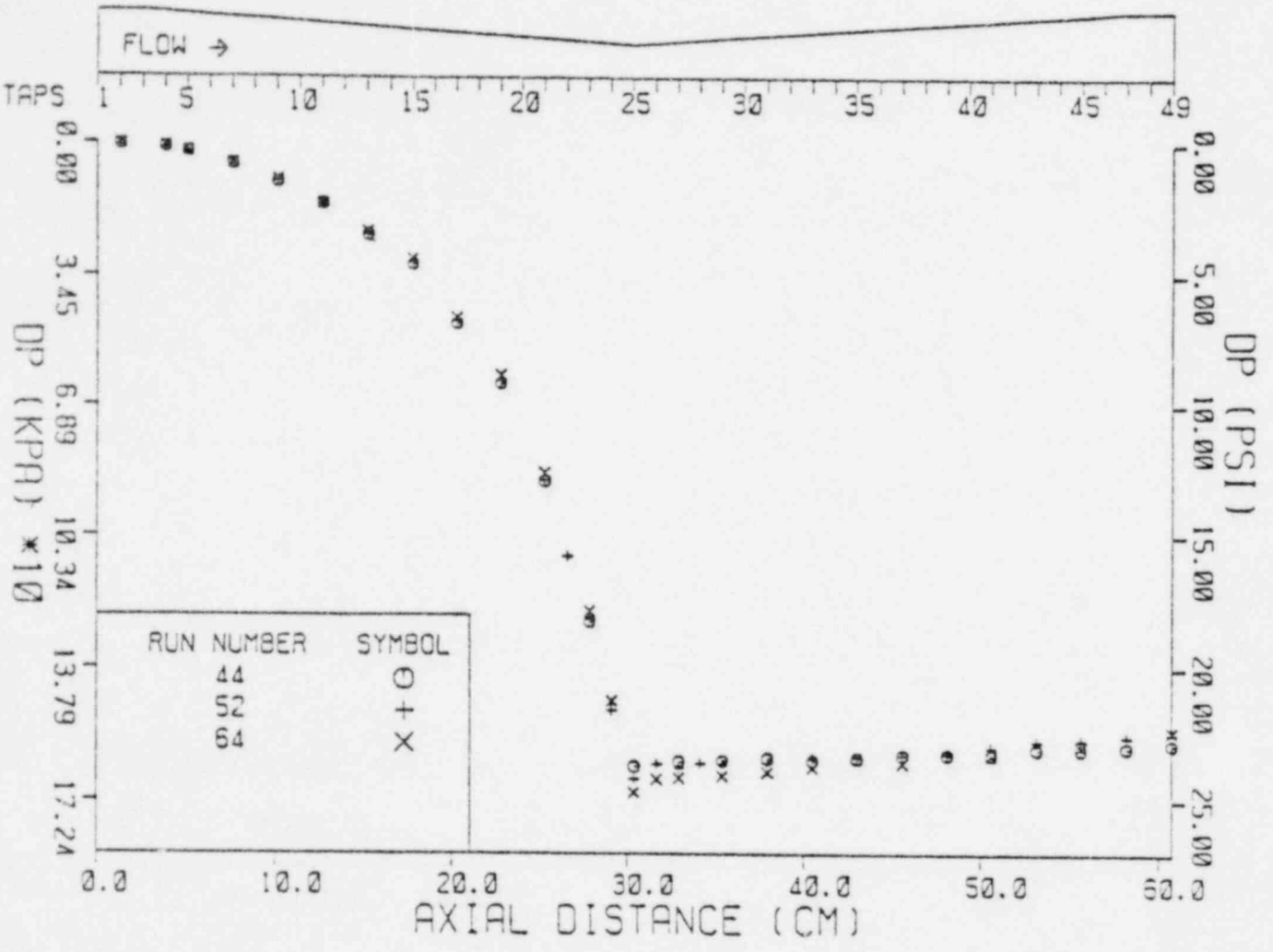

Figure 5-21 Effect of Nozzle Inlet Temperature at Constant $(p_{in} - p_{sat}(T_{in}))$ on the Pressure Distribution in the Nozzle (BNL Neg. No. 3-1034-79).

SCALE 1:1

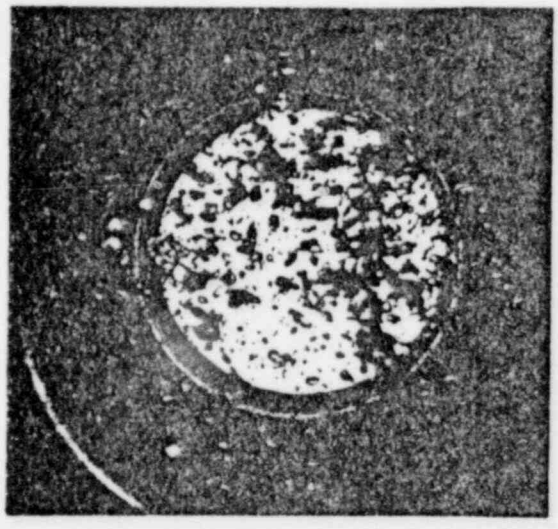

RUN NO. 55

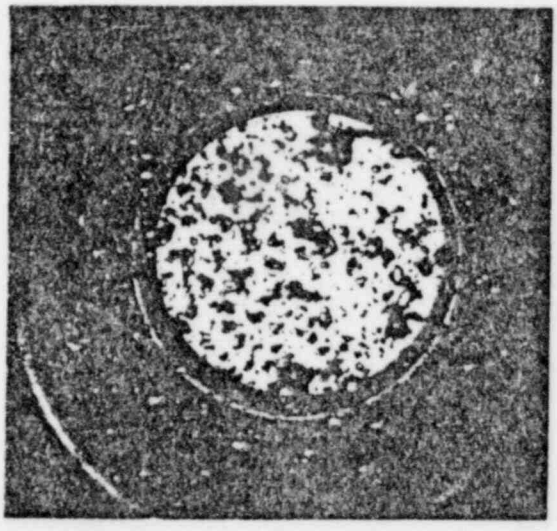

RUN NO. 55

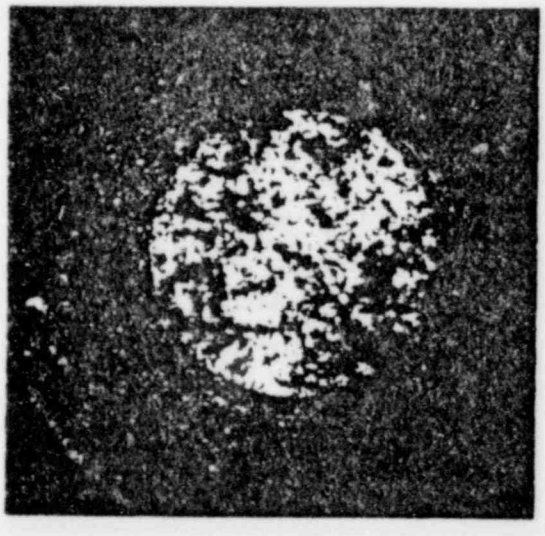

RUN NO. 52

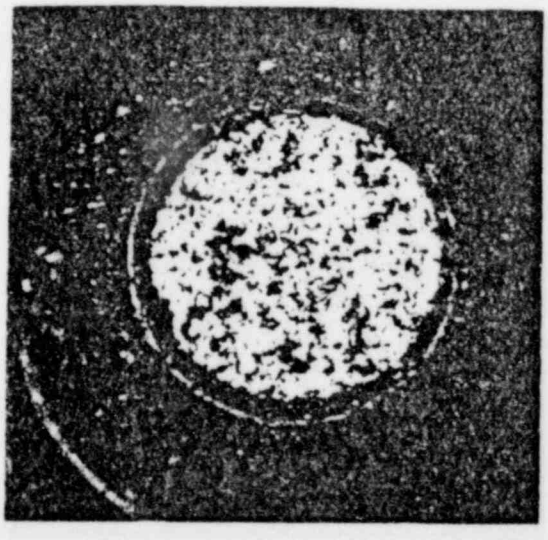

RUN NO. 52

Figure 5-22 Photographic Observations for Experimental Conditions Presented in Fig. 5-19 and 5-21 (ANL Neg. No. 1-920-79).

photographic observations for Exp. 55 and 52.

Finally, the influence of variation of p_{in}, i.e., moving the point A in Fig. 5-6 up and down without changing anything else, was studied. A slight variation of the inlet pressure was found to affect the pressure distributions and flashing regimes for identical inlet temperatures and mass fluxes. This dependence and sensitivity is more pronounced at low mass fluxes, Fig. 5-23 (Runs 55 and 58 with an inlet temperature of 123.5°C and mass flux of 2.98 Mg/m^2s). A variation of the inlet pressure from 293 kPa (Run 55) to 254 kPa (Run 58) shows a marked variation in the pressure distributions in the diverging section of the nozzle.* This strong dependence observed for the low mass fluxes does not repeat itself at the higher mass fluxes, 3.04 and 4.96 Mg/m^2sec, as presented in Figs. 5-24 and 5-25 for an inlet temperature of 100 °C.

5.2.4 Flashing Upstream of the Throat

In all the experiments presented above, flashing occurred in the vicinity of the throat. By controlling the flow conditions, we were able to approach saturation conditions at the inlet of the test section. The pressure distribution recorded under this condition is presented in Fig. 5-26. The continuous pressure decrease in the converging, as well as the diverging sections of the nozzle, is reminiscent of the supercritical flows in supersonic nozzles in classical gasdynamics. The onset of flashing, which is accompanied with a strong deviation in the pressure distribution as compared to the single phase calibration, is depicted in Fig. 5-27.

*Note that in these two experiments, the condensing tank pressure also varied from 174 kPa (Exp. 58) to 251 kPa (Exp. 55).

RUN	$G(Mg/m^2s)$	p_{in}(kPa)	T_{in}(C)	$p_{c.t.}$(kPa)
55	2.99	293	123.6	251
58	2.98	254	123.3	174

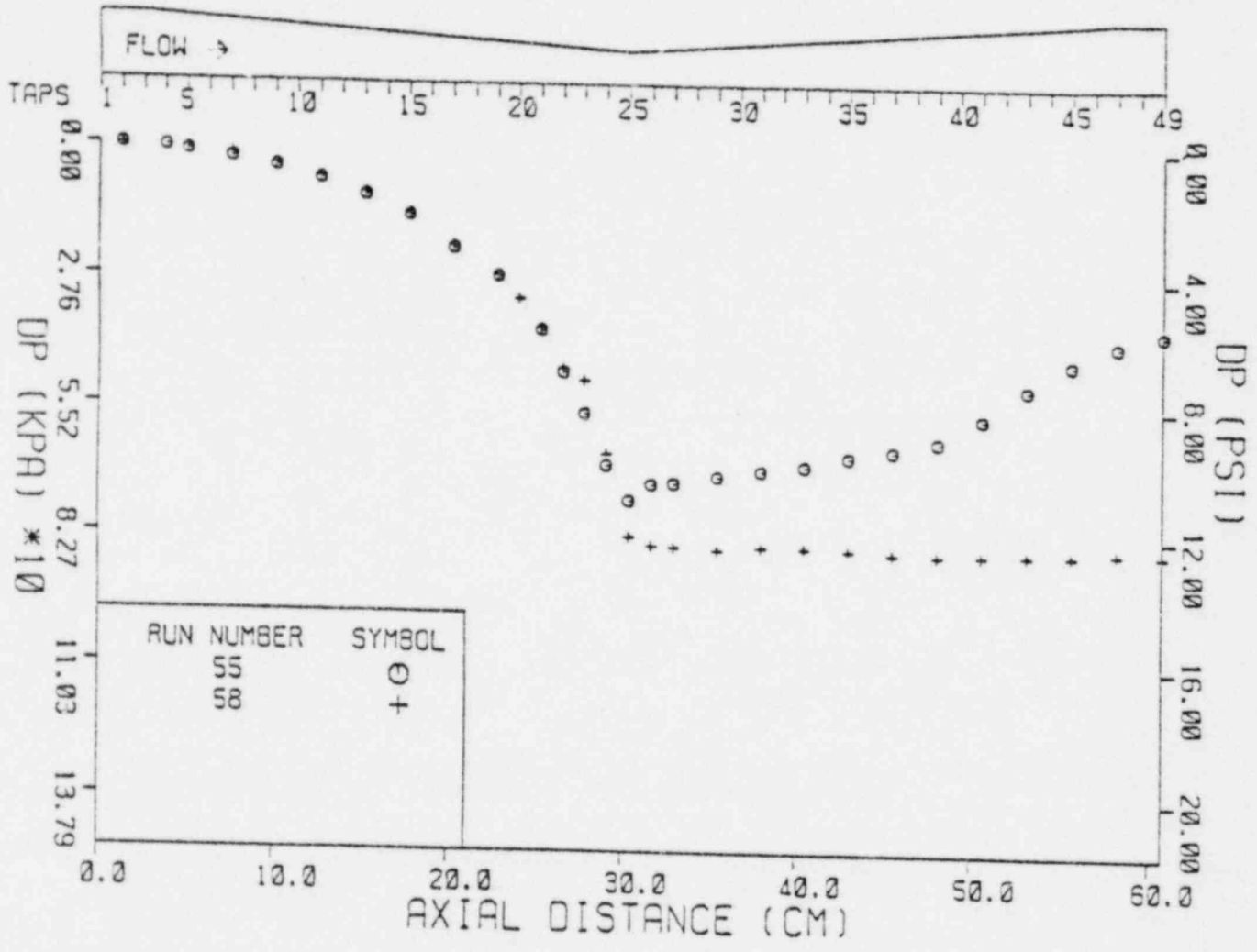

Figure 5-23 Effect of Nozzle Inlet Pressure on the Pressure Distributions in the Test Section (BNL Neg. No. 3-1036-79)

RUN	G(Mg/m^{2}s)	P_{in}(kPa)	T_{in}(C)	$P_{c.t.}$(kPa)
22	3.04	170	100.2	125
48	3.04	183	99.9	100

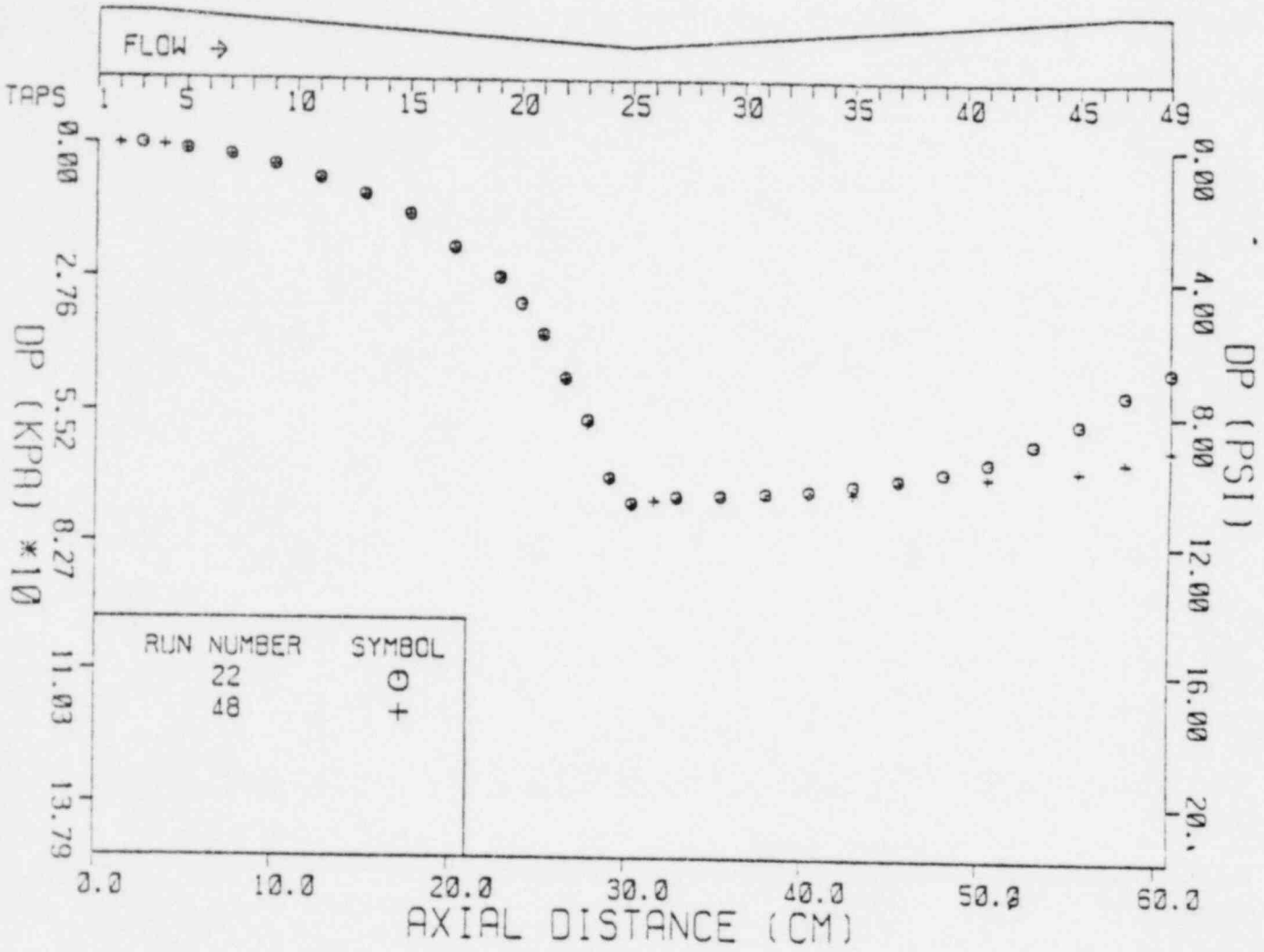

Figure 5-24 Effect of Nozzle Inlet Pressure on the Pressure Distributions in the Test Section (BNL Neg. No. 3-1023-79)

RUN	$G(Mg/m^2s)$	p_{in}(kPa)	T_{in}(C)	$p_{c.t.}$(kPa)
45	4.97	308	99.8	99
37	4.94	296	100.3	170
43	4.97	287	100.2	121

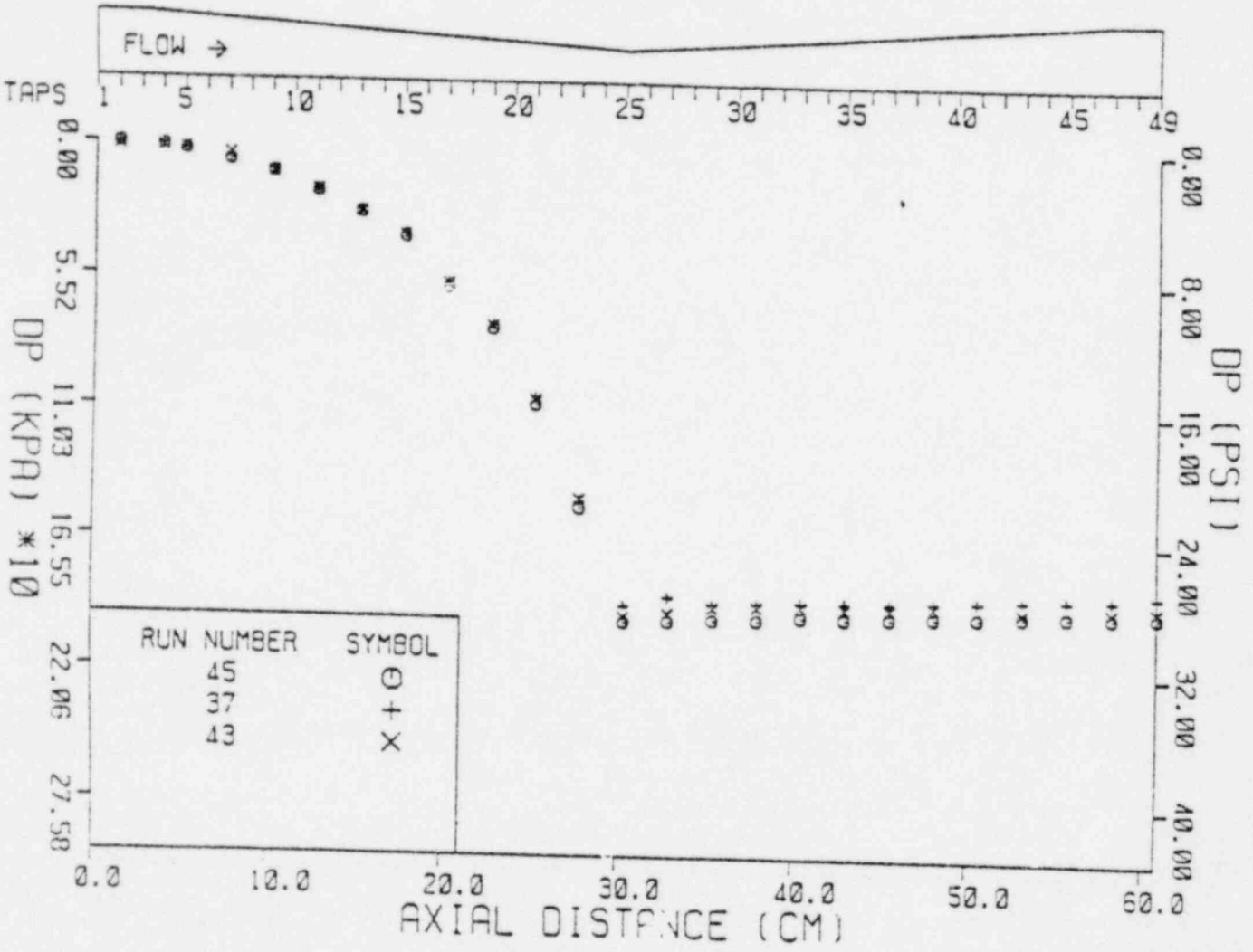

Figure 5-25 Effect of Nozzle Inlet Pressure on the Pressure Distributions in the Test Section (BNL Neg. No. 3-1025-79)

RUN	G(Mg/m^2s)	p_{in}(kPa)	T_{in}(C)	$p_{c.t.}$(kPa)
69	1.23	399	144.3	188

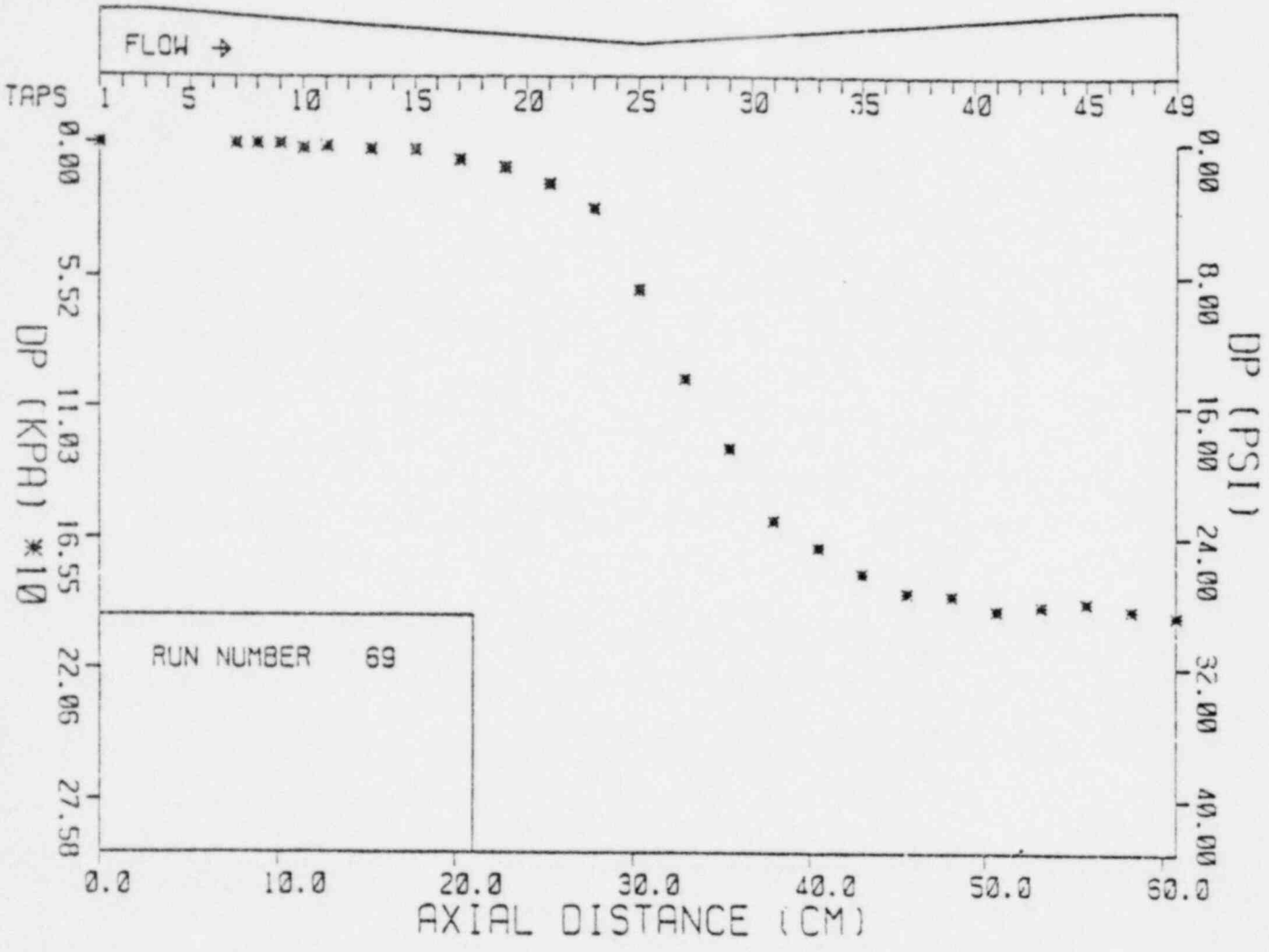

Figure 5-26 Pressure Distributions in the Test Section While Flashing Onset is Upstream of the Nozzle Throat (BNL Neg. No. 3-1024-79)

RUN	G(Mg/m^{2}s)	p_{in}(kPa)	T_{in}(C)	$p_{c.t.}$(kPa)
69	1.23	399	144.3	188

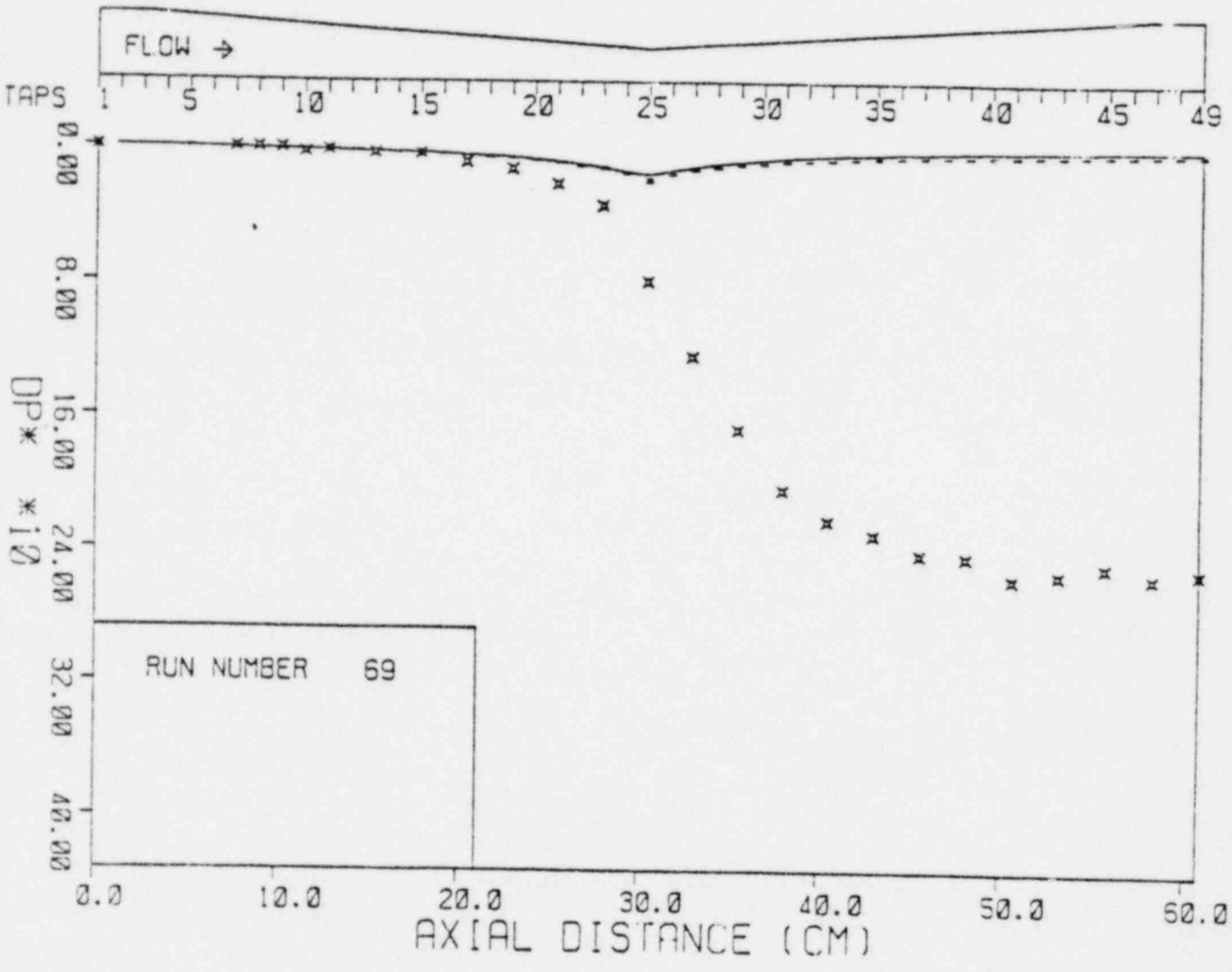

Figure 5-27 Nondimensional Pressure Distribution $DP^* = DP/\frac{1}{2}\rho U_o^2$ in the Test Section While the Flashing Onset is Upstream of the Nozzle Throat (BNL Neg. No. 3-1026-79)

5.3 Void Fraction Measurements Under Flashing Conditions

Both axial centerline traverses of the void fraction were undertaken and, for the later runs, traverse profiles were determined at selected locations. The axial distributions of the diametrical averaged void fractions, together with the static pressures under various flashing conditions, are presented in Sections 5.3.1 and 5.3.2 (Table 5-3). The transverse void distributions are discussed in Section 5.3.3.

5.3.1. Flashing Close to the Throat (Axial Scan)

Figures 5-28A and 5-28B present the results for an inlet temperature and pressure of 99°C and 394 kPa and a mass flux of 6.05 Mg/m^2s. The pressure profile is constant in the diverging section, and the void profiles follow an almost linear variation in Fig. 5-28B. The (+) symbols are the void fraction data, and the crossed circles in Fig. 5-28B give the difference between the two-phase and single phase dimensionless pressure distributions. The dimensionless pressure was defined as the local pressure drop divided by the inlet dynamic pressure of the flow. DP_m^* is the dimensionless local pressure drop with respect to the nozzle inlet measured under flashing conditions and DP_c^* is the corresponding pressure drop measured during the single phase calibration experiments. The onset of flashing can be determined either from the void fraction measurements or from the point of departure of the dimensionless pressure distribution from the single phase calibration curve.

Reducing the mass flux to 4.91 Mg/m^2s and to 3.06 Mg/m^2s while keeping

TABLE 5-3

VOID FRACTION DISTRIBUTION DATA

FLASHING EXPERIMENTS

RUN	P_{in}(kPa)	T_{in}(^{o}C)	G(Mg/m^{2}s)	P_{ct}(kPa)	T_{ct}(^{o}C)
730	285	99.4	4.91	54	88.0
740	285	99.4	4.91	54	88.0
762	394	99.3	6.05	61	88.3
770	157	99.3	3.05	67	88.5
771	157	99.3	3.05	67	88.5
780	138	99.3	2.61	71	88.1
781	138	99.3	2.61	71	88.1
792	125	99.4	2.26	76	88.1
793	125	99.4	2.26	76	88.1
801	582	148.3	4.34	434	143.5
802	582	148.3	4.34	434	143.5
812	493	148.3	2.91	431	144.4
813	493	148.3	2.91	431	144.4
821	376	142.3	2.34	175	111.3
822	376	142.3	2.34	175	111.3
831	350	140.0	2.30	147	107.5
832	350	140.0	2.30	147	107.5

TABLE 5-3

VOID FRACTION DISTRIBUTION DATA

FLASHING EXPERIMENTS
(continued)

RUN	p_{in}(kPa)	T_{in}(^{o}C)	G(Mg/m^{2}s)	p_{ct}(kPa)	T_{ct}(^{o}C)
117, 118	143.	99.9	2.28	127.	100.4
120, 121	151.	100.1	2.63	127.	100.5
123, 124	171.	100.2	3.01	133.	100.7
126	251.	99.9	4.50	165.*	100.4
127	248.	100.0	4.49	127.	100.5
130, 131	380.	99.9	5.97	127.	100.4
134, 135	349.	121.2	4.43	233.	121.7
138, 139	464.	121.2	5.90	234.	121.6
142, 143	241.	121.3	2.97	237.	121.7
146, 147	305.	121.2	3.70	234.	121.7

*P_{ct} is uncertain

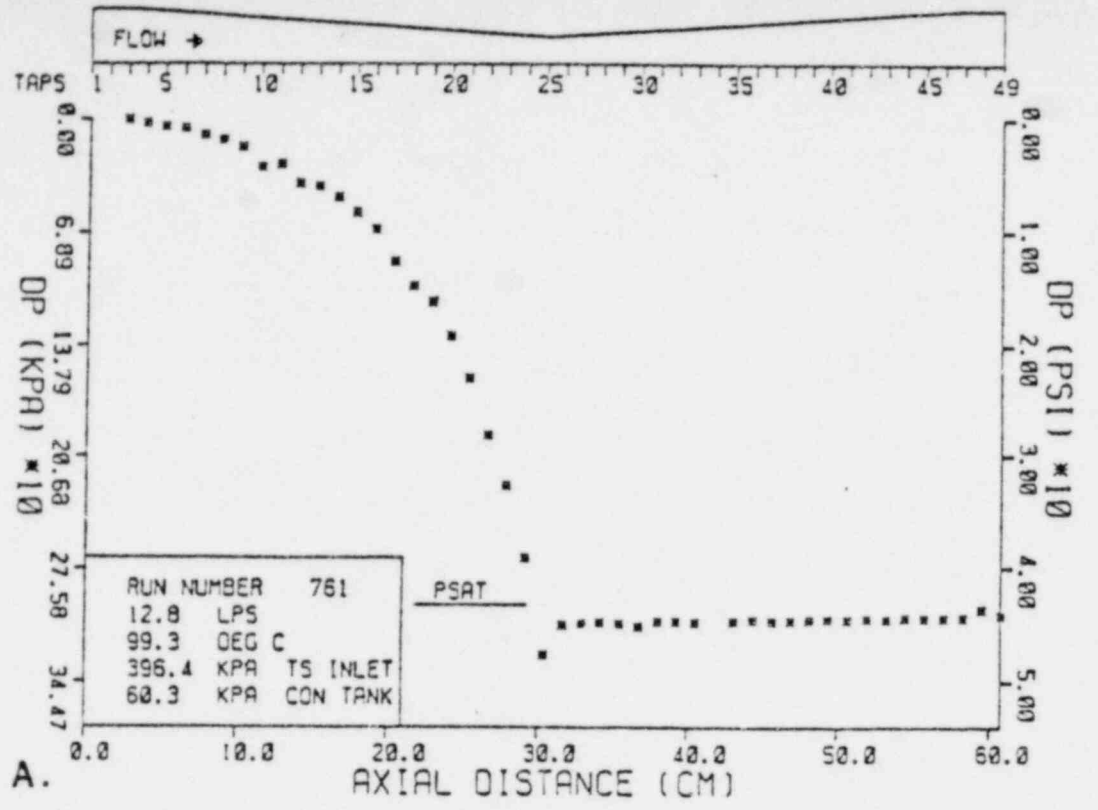

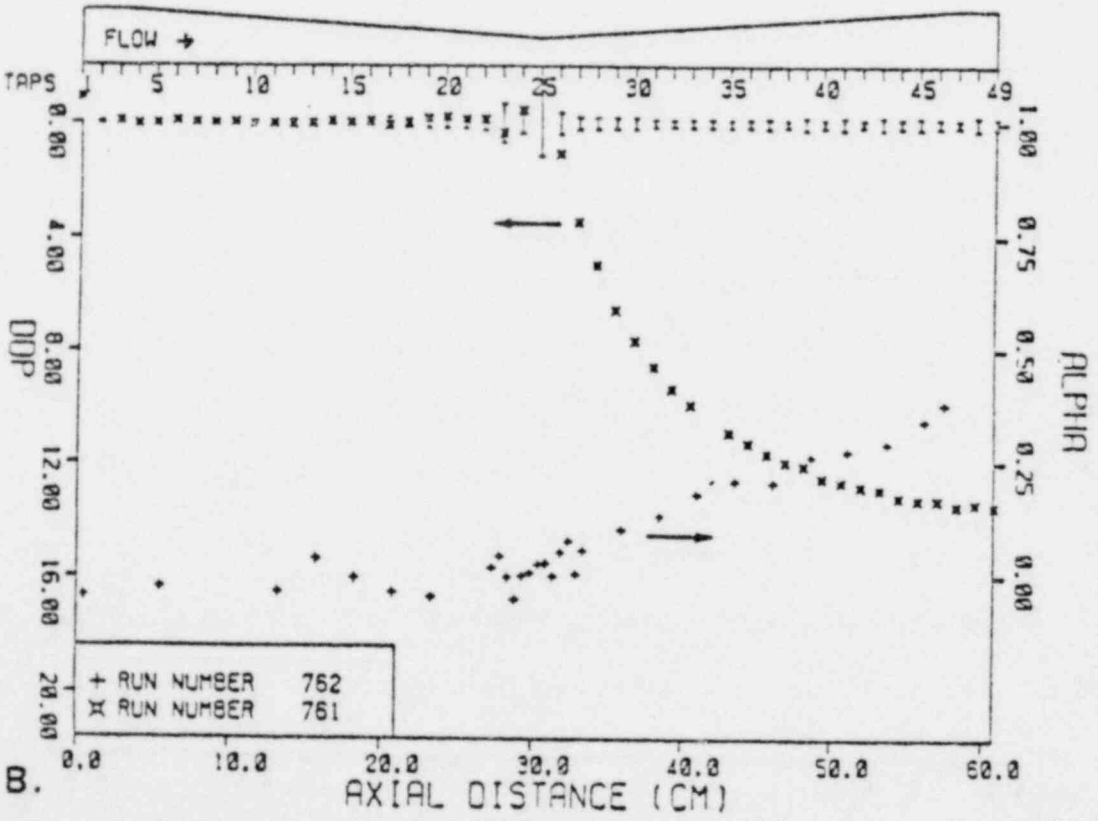

Figure 5-28 Pressure and axial void fraction distributions in the test section. Plot of the difference between the dimensionless measured pressure drop and the nondimensional pressure drop measured in the single phase calibration ($DDP = DP^*_m - DP^*_c$) as function of axial distance. (BNL Neg. No. 3-1644-79).

the inlet temperature constant ~ 99°C we obtained similar results, which are presented in Figs. 5-29 and 5-39. The onset of flashing is close to, but upstream of the nozzle throat. The linear variation of the void fraction with axial distance in the diverging section, combined with the constant pressures observed in Fig. 5-29A and the fact that the test section diameter also varied linearly, seems to imply the presence of a nearly constant area liquid jet at the core surrounded by a steam envelope. When the mass flux is further reduced to 3.05 Mg/m^2s, the pressure profile in the diverging section starts to show a slight recovery (Fig. 5-30A), which is accompanied in the void fraction profiles by a region where the voids are constant (Fig. 5-30B). If one still reduces the mass flux to 2.61 Mg/m^2s, the pressure distributions observed in Fig. 5-31A, show a sudden pressure recovery in the diverging section which may be considered as a condensation front. This fact is clearly observed in Fig. 5-31B, which shows an increase in the void fraction followed by a decrease to the all liquid situation. The dimensionless profiles of DDP plotted on the same figure also show the pressure deviations from the single phase calibration which closely follow the evaporation and condensation fronts. Still lowering the mass flux to 2.26 Mg/m^2s brings us to a situation which is close to the onset of flashing. Figure 5-32A depicts the pressure distribution which is very close to the single phase calibration results, and the void fraction distribution presented in Fig. 5-32B shows a very slight rise close to the throat, but otherwise remains mostly liquid throughout the test section. A similar sequence of events was also observed in experiments at an inlet temperature of 148.3°C for two mass fluxes 4.34 Mg/m^2s (Fig. 5-33A and 5-33B) and 2.91 Mg/m^2s (Fig. 5-34A and Fig. 5-34B). The high mass flux

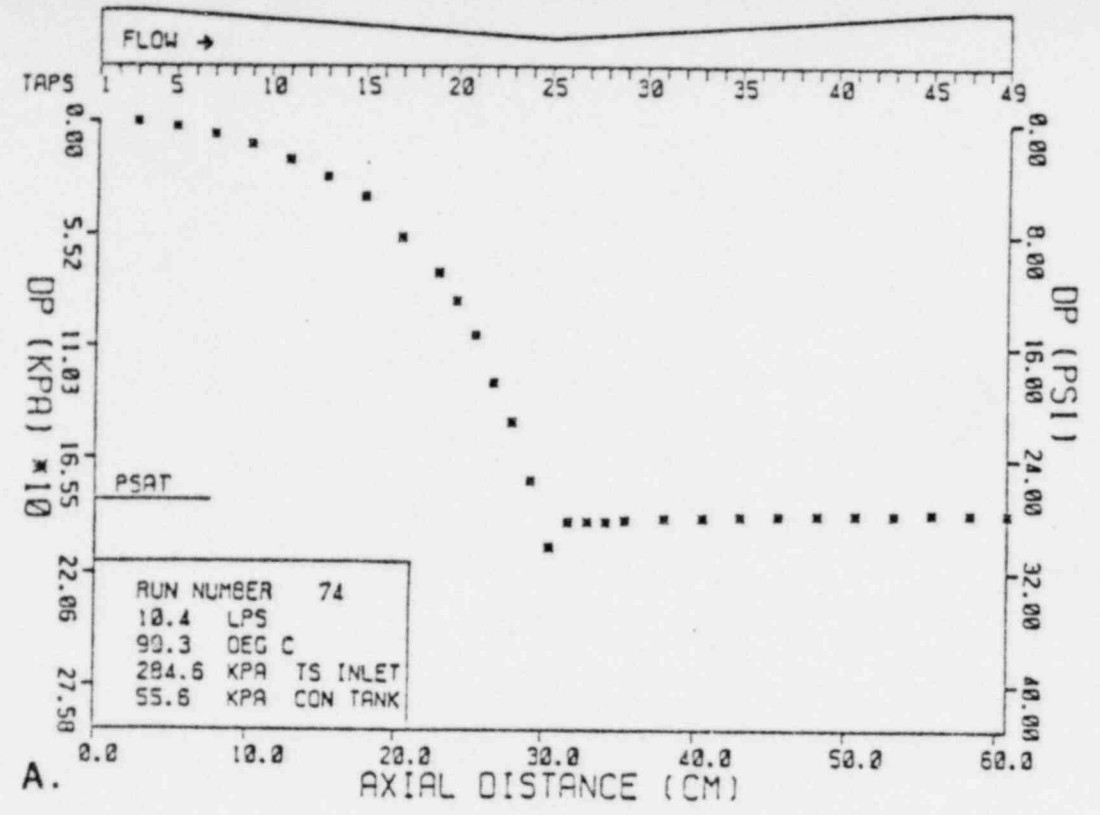

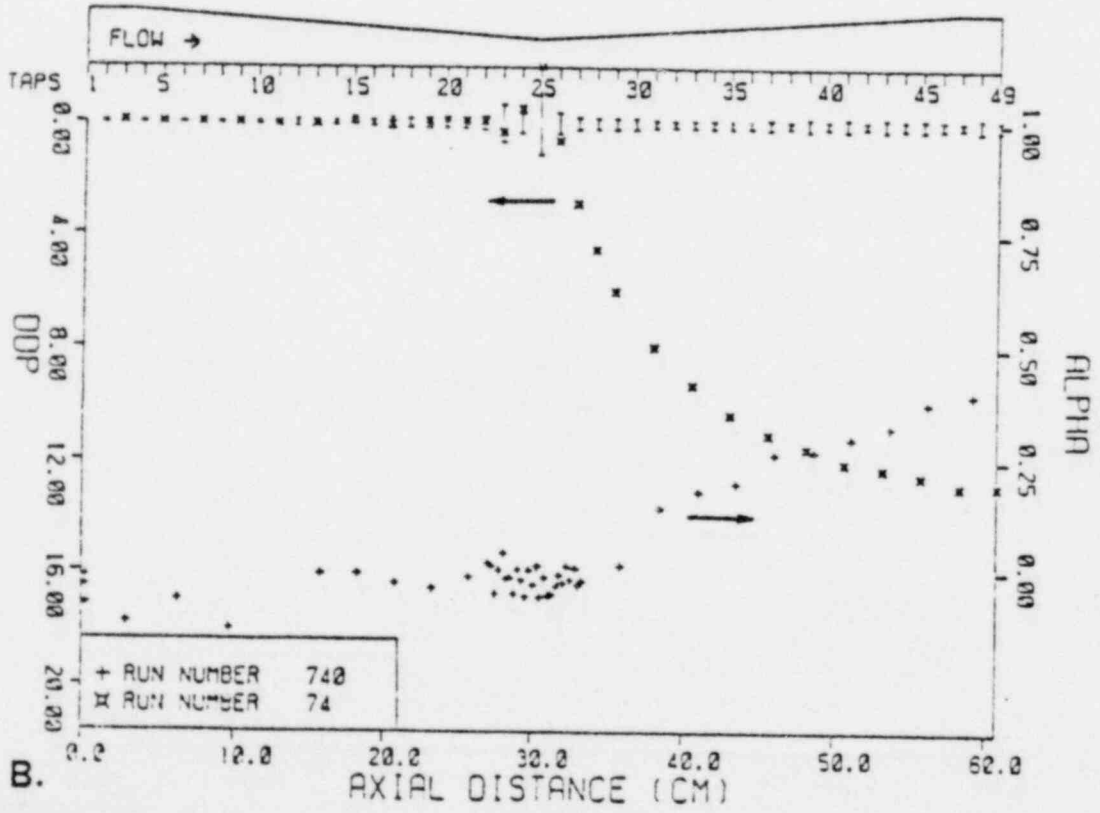

Figure 5-29 Pressure and axial void fraction distributions in the test section. Plot of the difference between the dimensionless measured pressure drop and the nondimensional pressure drop measured in the single phase calibration ($DDP = DP^{*}_{m} - DP^{*}_{c}$) as function of axial distance. (BNL Neg. No. 3-1645-79).

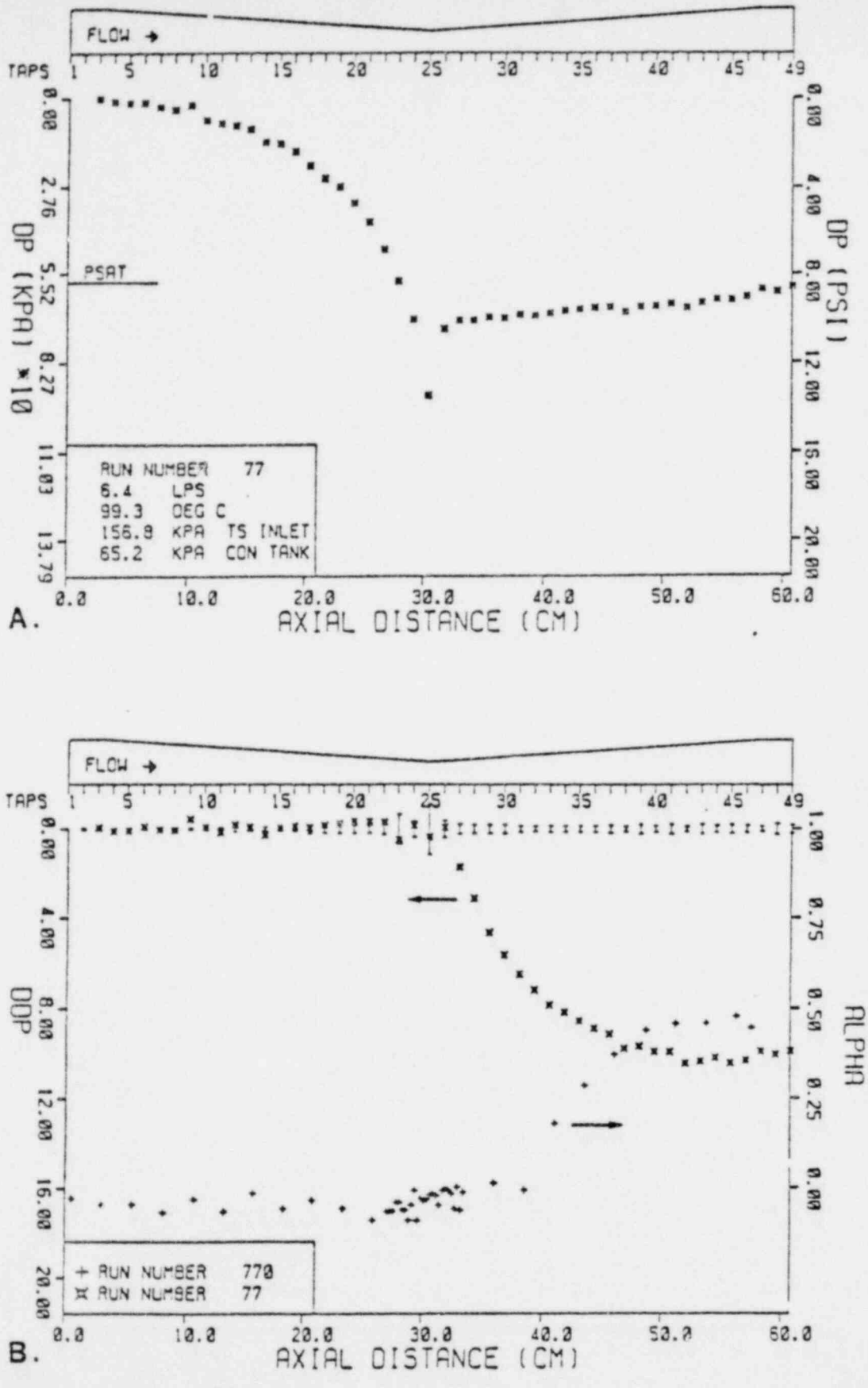

Figure 5-30 Pressure and axial void fraction distributions in the test section. Plot of the difference between the dimensionless measured pressure drop and the nondimensional pressure drop measured in the single phase calibration ($DDP = DP_m^* - DP_c^*$) as function of axial distance. (BNL Neg. No. 3-1643-79).

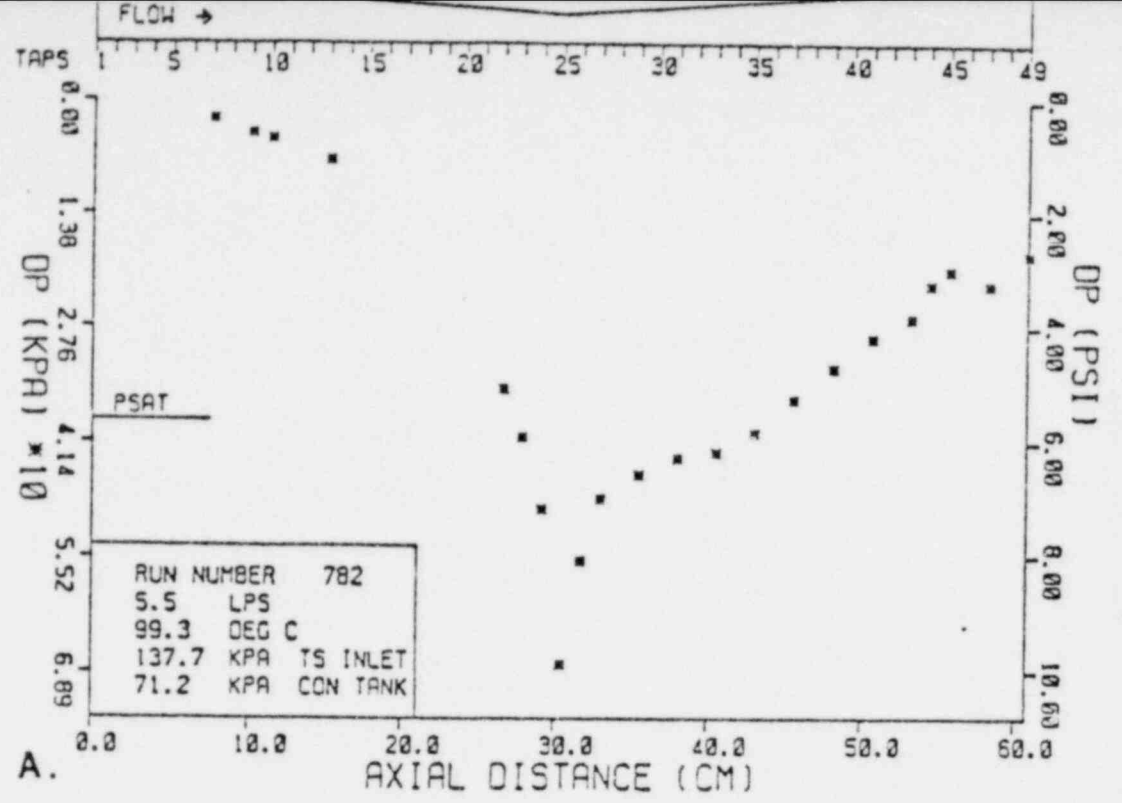

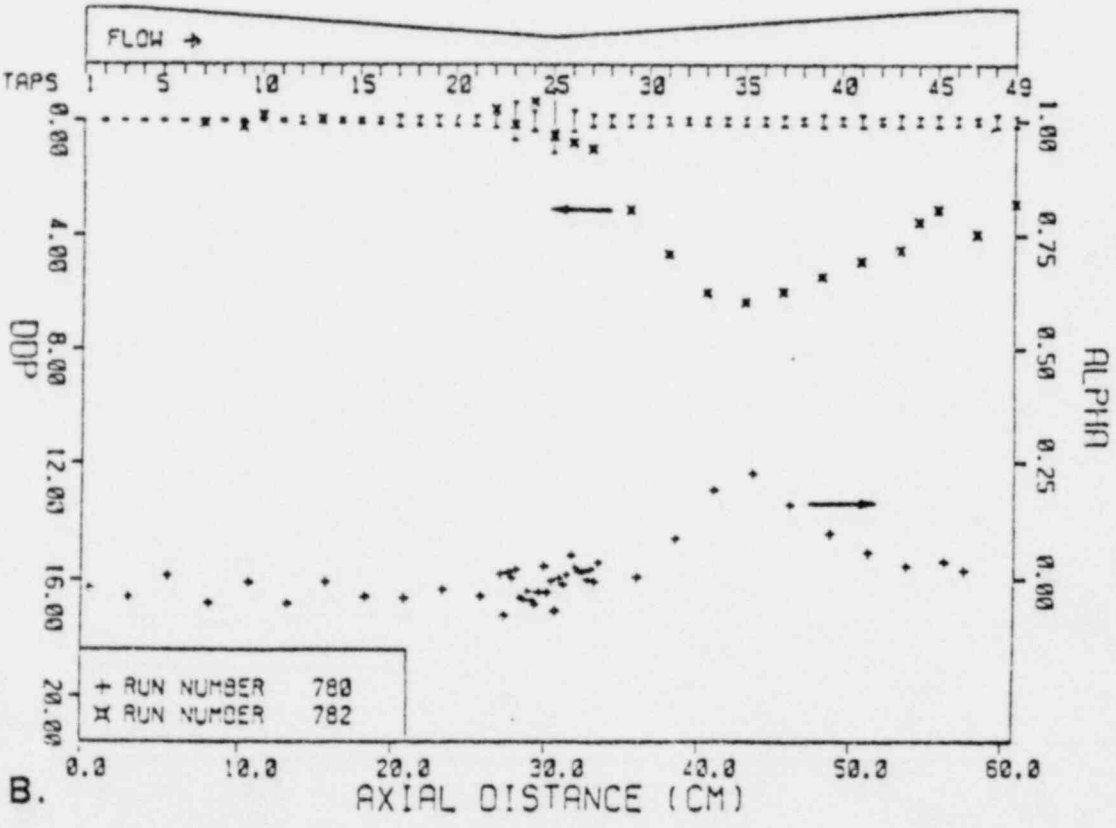

Figure 5-31 Pressure and axial void fraction distributions in the test section. Plot of the difference between the dimensionless measured pressure drop and the nondimensional pressure drop measured in the single phase calibration ($DDP = DP^*_m - DP^*_c$) as function of axial distance. (BNL Neg. No. 3-1642-79).

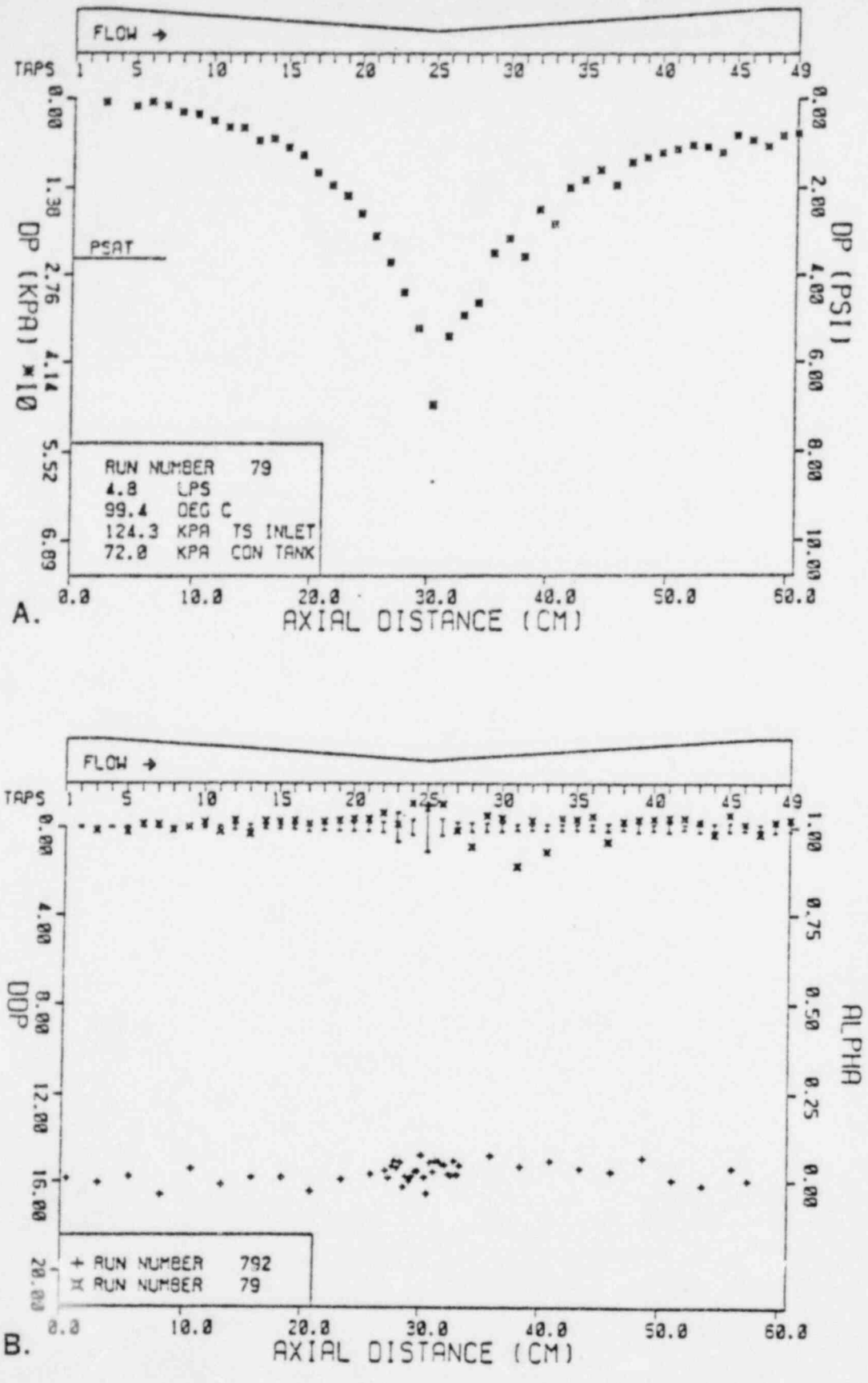

Figure 5-32 Pressure and axial void fraction distributions in the test section. Plot of the difference between the dimensionless measured pressure drop and the nondimensional pressure drop measured in the single phase calibration ($DDP = DP_m^* - DP_c^*$) as function of axial distance. (BNL Neg. No. 3-1110-79).

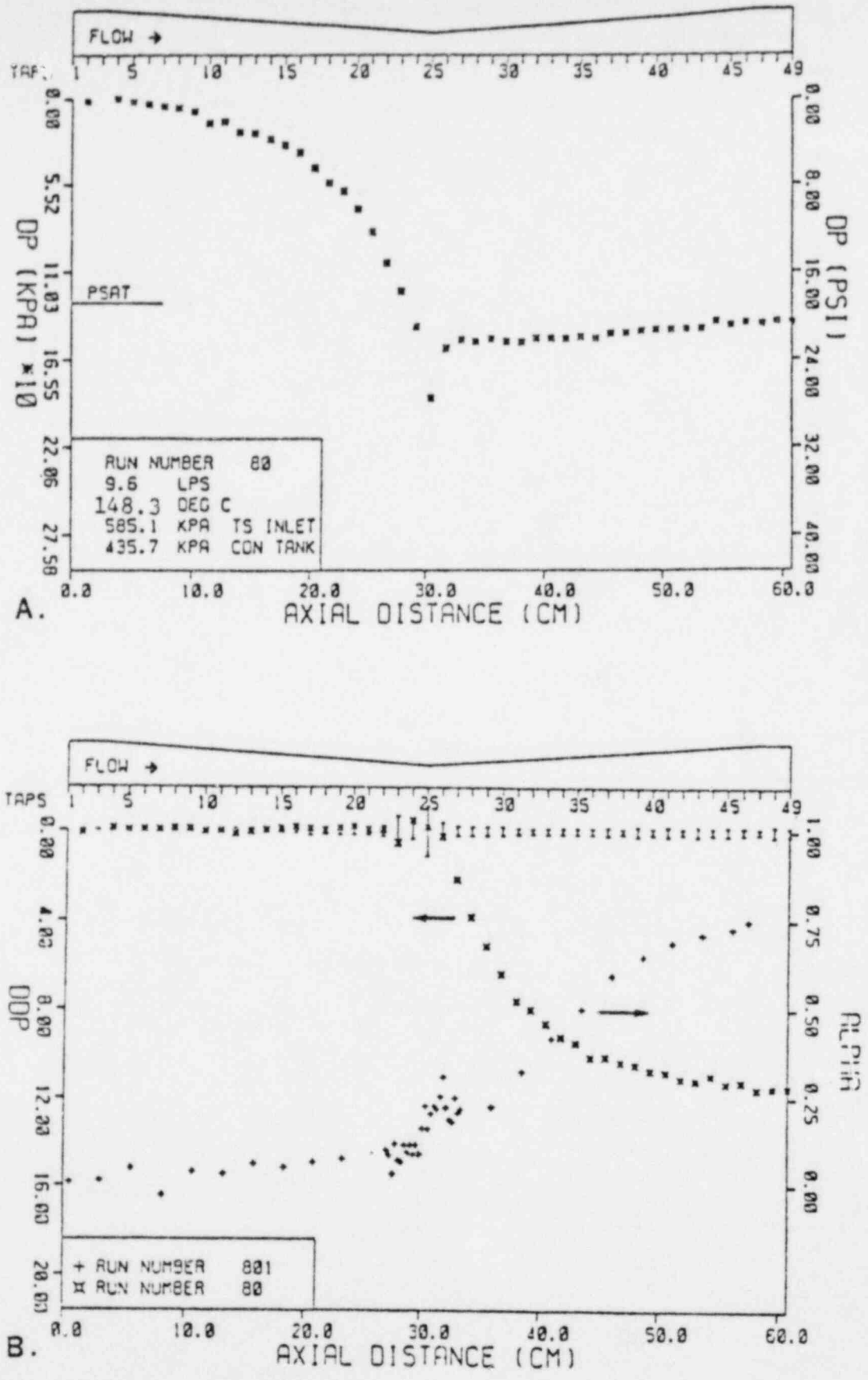

Figure 5-33 Pressure and axial void fraction distributions in the test section. Plot of the difference between the dimensionless measured pressure drop and the nondimensional pressure drop measured in the single phase calibration ($DDP = DP_m^* - DP_c^*$) as function of axial distance. (BNL Neg. No. 3-1111-79).

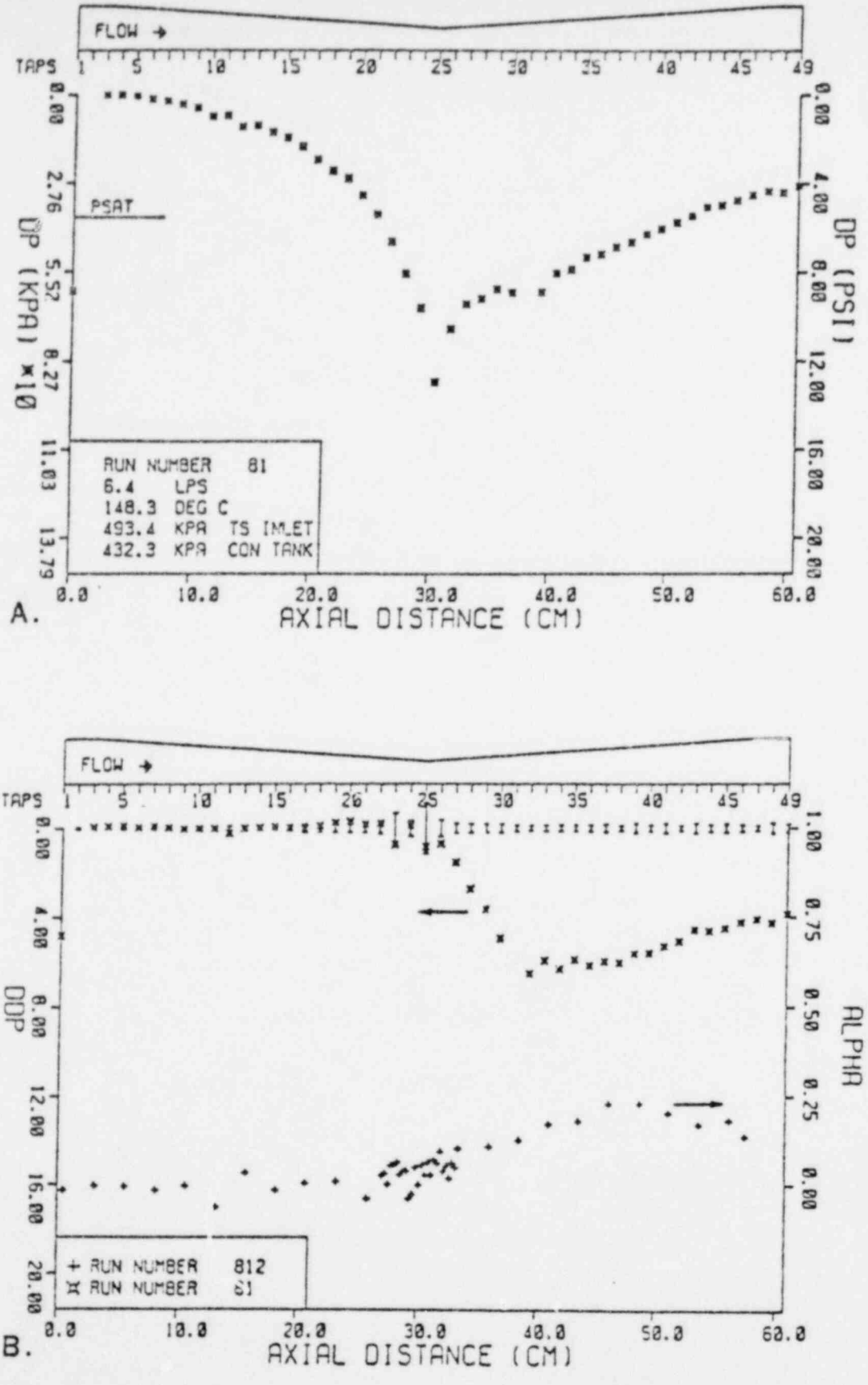

Figure 5-34 ssure and axial void fraction distributions in the test section. Pl of the difference between the dimensionless measured pressure drop and the nondimensional pressure drop measured in the single phase calibration ($DDP = DP_m^* - DP_c^*$) as function of axial distance. (BNL Neg. No. 3-1112-79).

run presented in Fig. 5-33A and 5-33B shows an almost constant pressure distribution in the diverging section with a steeper rise in the void fraction profiles and higher void fraction values at the exit of the nozzle. The lower mass flux run presented in Fig. 5-34A and 5-34B depicts a vaporization zone in the diverging section downstream of the throat followed by a condensation region which reduces the void fraction (Fig. 5-34B) and causes a pressure recovery close to the test section exit (Fig. 5-34A).

5.3.2. Flashing Upstream of the Throat (Axial Scan)

Additional data was also recorded with the flashing front upstream of the throat. Figures 5-35 and 5-36 present the results for two mass fluxes 2.34 and 2.30 Mg/m^2s at an inlet temperature of 140°C. Figure 5-35A depicts the pressure distribution for which Fig. 5-35B presents the void fraction profiles. The pressure distribution shows a decrease in the converging, as well as in the diverging sections of the nozzle. However, the slope seems not to be continuous at the throat in contrast to what is usually presented in the literature. The void fraction profiles show that at the test section inlet, the void fraction was around 10 percent, and the vapor generation increases along the test section, causing a void fraction of almost unity at the exit of the venturi. The DDP plot shows clearly the drastic deviation of the dimensionless pressure profiles from the single phase calibration curve. Figures 5-36A and 5-36B present similar results obtained at a mass flux of 2.22 Mg/m^2s and an inlet temperature of 140 °C. The results of those two experiments were used to calculate the net vapor generation rates under nonequilibrium conditions, and the methodology followed will be presented in the next section.

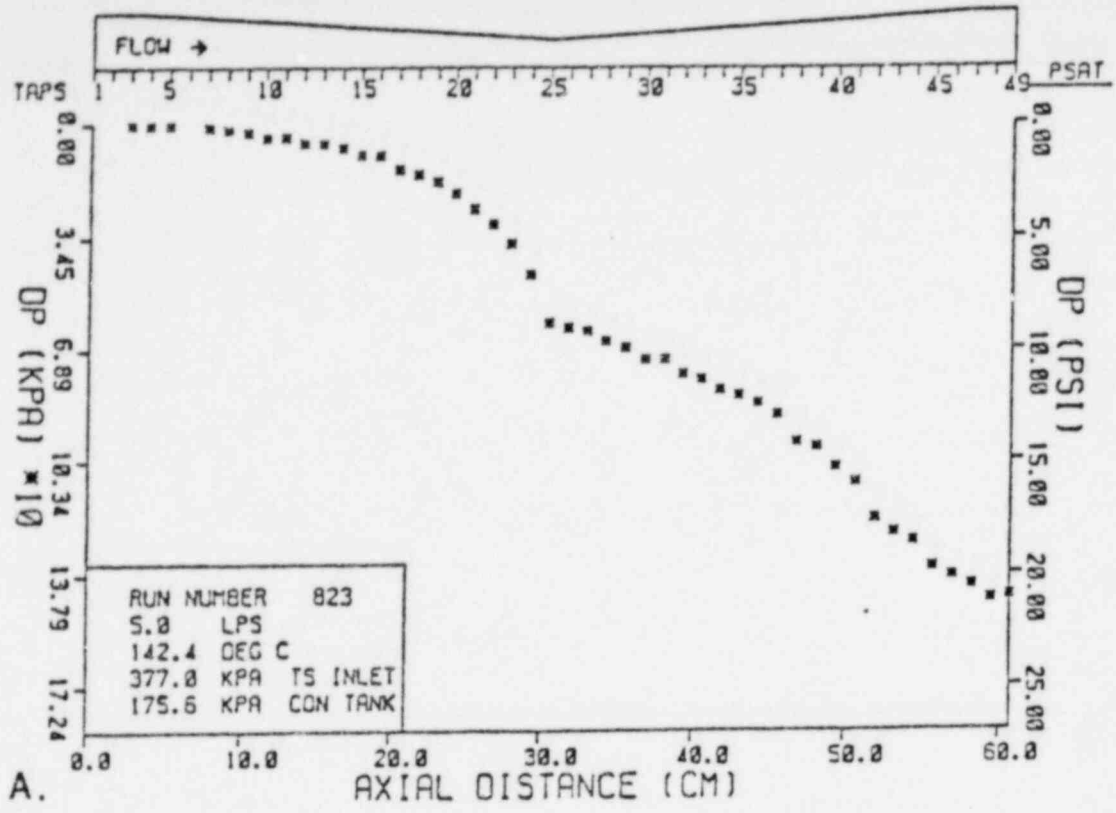

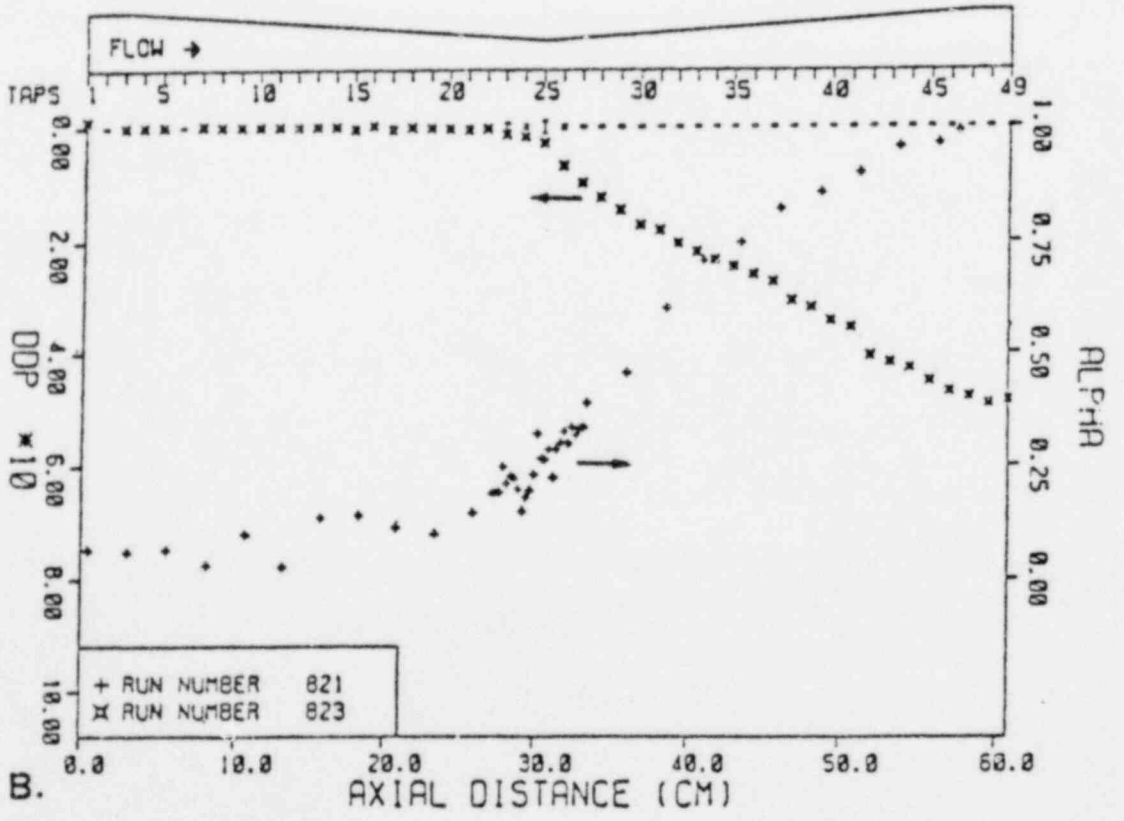

Figure 5-35 Pressure and axial void fraction distributions in the test section with flashing occurring upstream of the nozzle throat. Plot of the difference between the dimensionless measured pressure drop and the nondimensional pressure drop measured in the single phase calibration, ($DDP = DP^*_m - DP^*_c$) as a function of axial distance (BNL Neg. No. 3-1108-79).

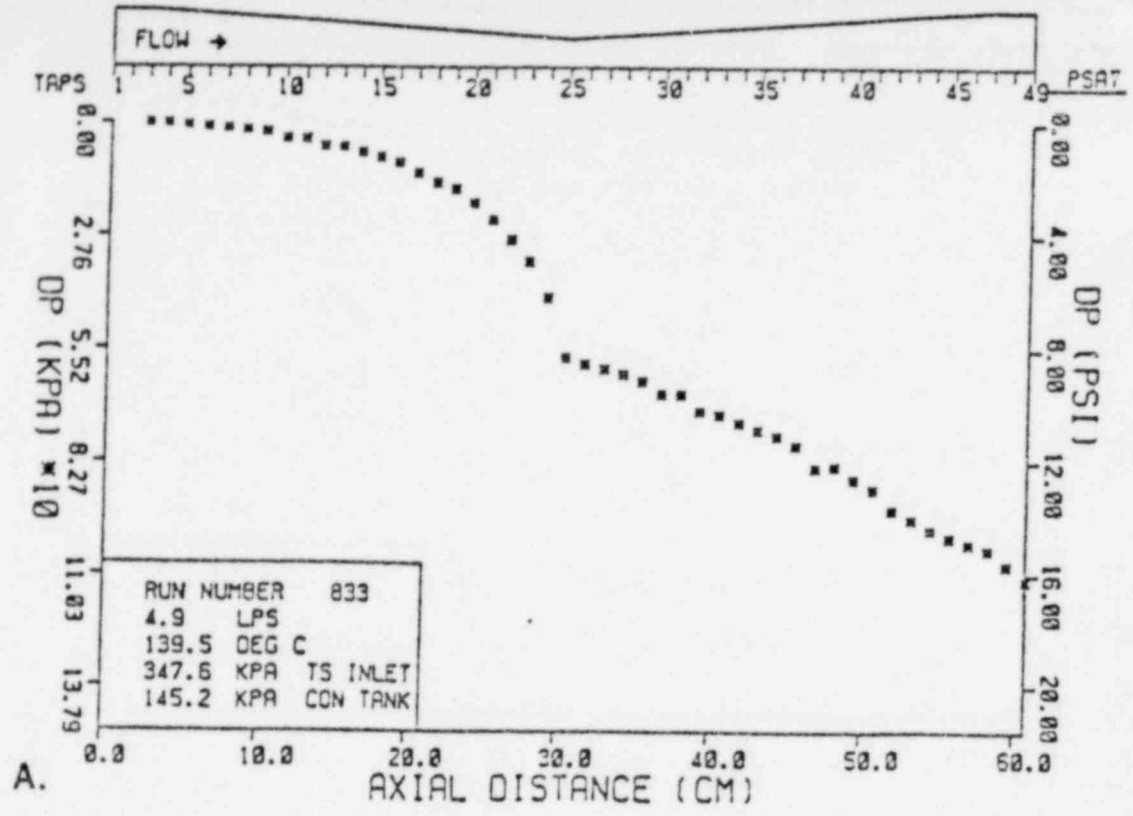

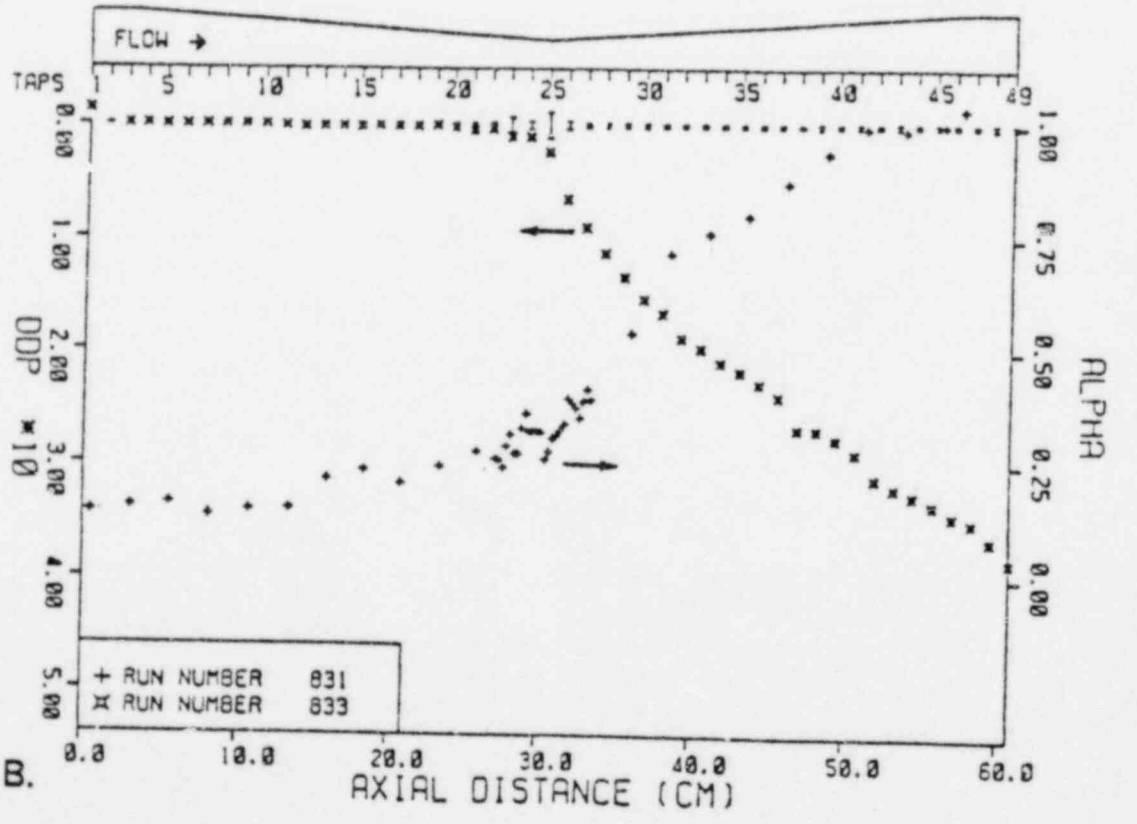

Figure 5-36 Pressure and axial void fraction distributions in the test section with flashing occurring upstream of the nozzle throat. Plot of the difference between the dimensionless measured pressure drop and the nondimensional pressure drop measured in the single phase calibration, ($DDP = DP_m^* - DP_c^*$) as a function of axial distance. (BNL Neg. No. 3-1109-79).

5.3.3 Transverse Void Distributions and Area Averaged Void Fractions

Transverse distribution of chordal averaged α's and area averaged α's have been measured under flashing conditions at 100° C and 125° C inlet temperatures and several mass fluxes according to the general test matrix. Typical results of Run 130 will be presented in this section. The transverse distributions of all the chordal-averaged void fractions are presented in Fig. 5-37, 5-38, 5-39, 5-40, 5-41, 5-42, and 5-43. In these figures, the chordal void fraction averaged from the ten sets of 9-s measurements are plotted vs. the radial (transverse) location. Once again, different symbols are used to represent each source. The dashed lines represent the boundaries of the nozzle at the axial location and the horizontal line depicts the area-averaged void fraction for that axial location, calculated from

$$\bar{\alpha} = \frac{\Sigma \alpha_i \Delta A_i}{\Sigma \Delta A_i} \qquad (5\text{-}1)$$

where ΔA_i is the chordal area defined by the gamma beam thickness at a given transverse location and α_i is the chordal averaged void fraction measured at the same location. It should be mentioned that while the errors in local chordal void fraction increase logarithmically as the traverse moves from the axial centerline to the outer wall, the areas associated with these increasingly inaccurate void fraction measurements decrease roughly quadratically to zero near the wall. Thus the effects on the average void fraction is minimal.

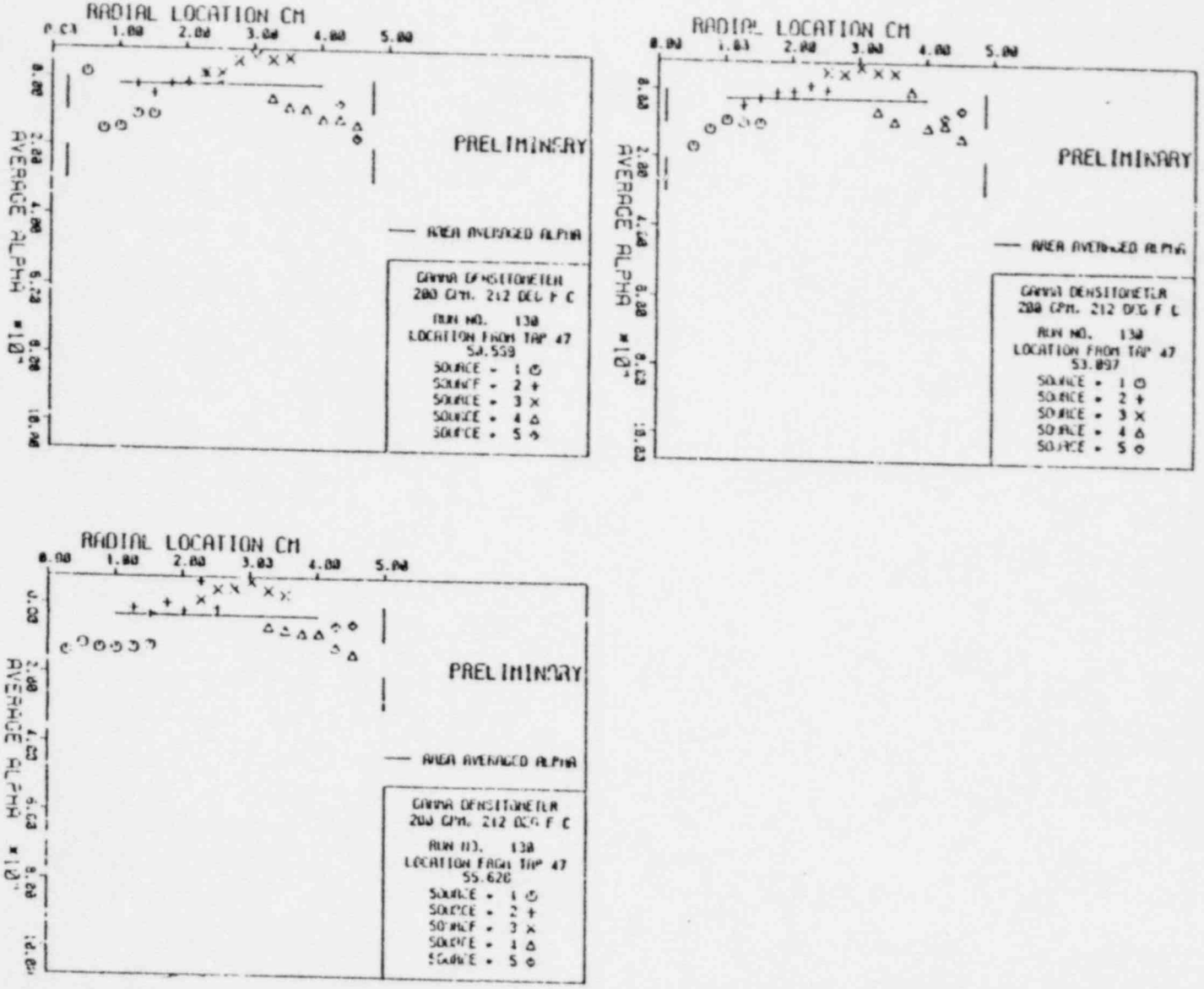

Figure 5-37 - Radial Distributions of the Chordal Averaged Void Fractions at Various Axial Locations Obtained by the Five Beam Gamma Densitometer for Run 130. (BNL Neg. No. 10-1405-79).

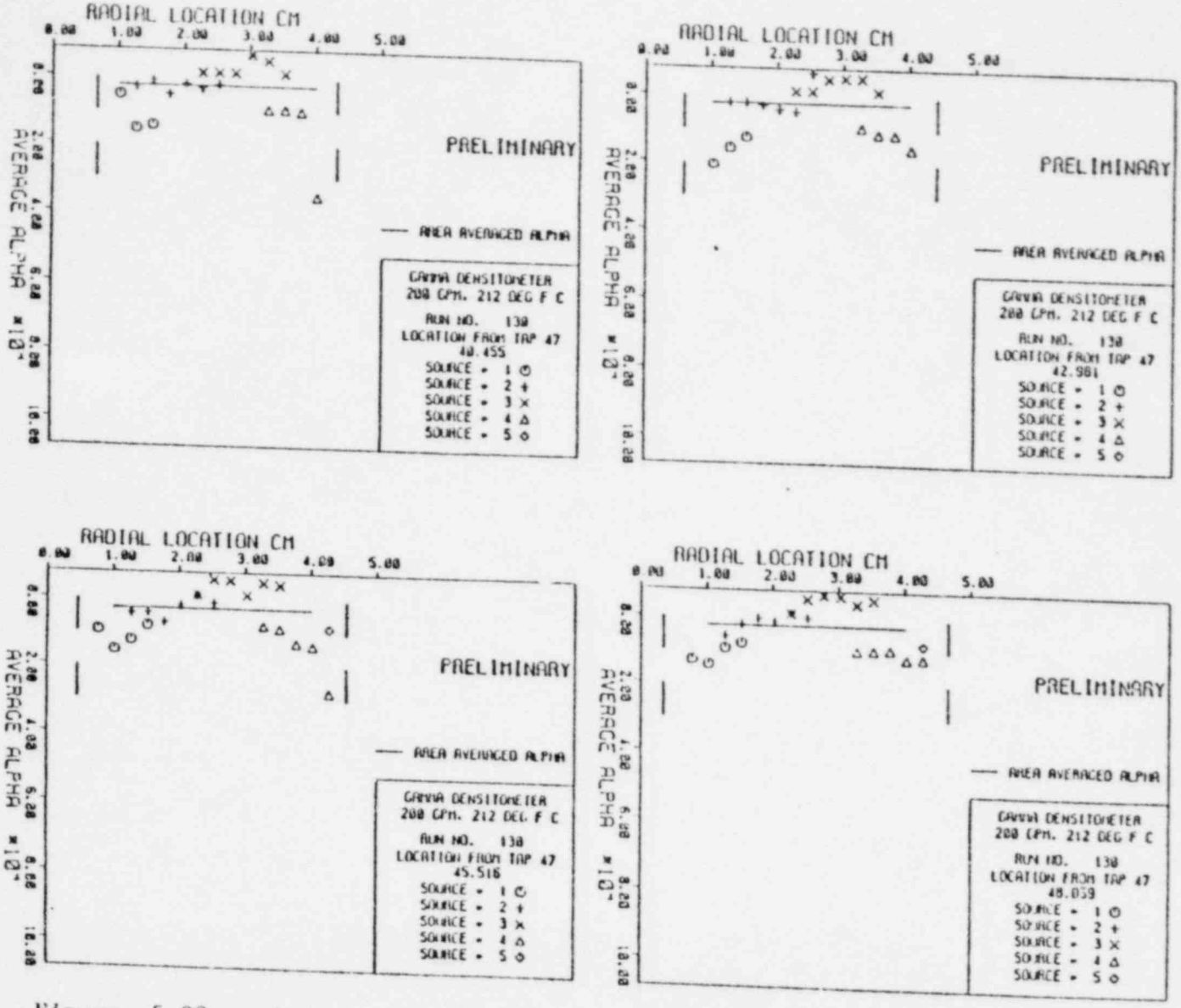

Figure 5-38 - Radial Distributions of the Chordal Averaged Void Fractions at Various Axial Locations Obtained by the Five Beam Gamma Densitometer for Run 130. (BNL Neg. No. 10-1411-79).

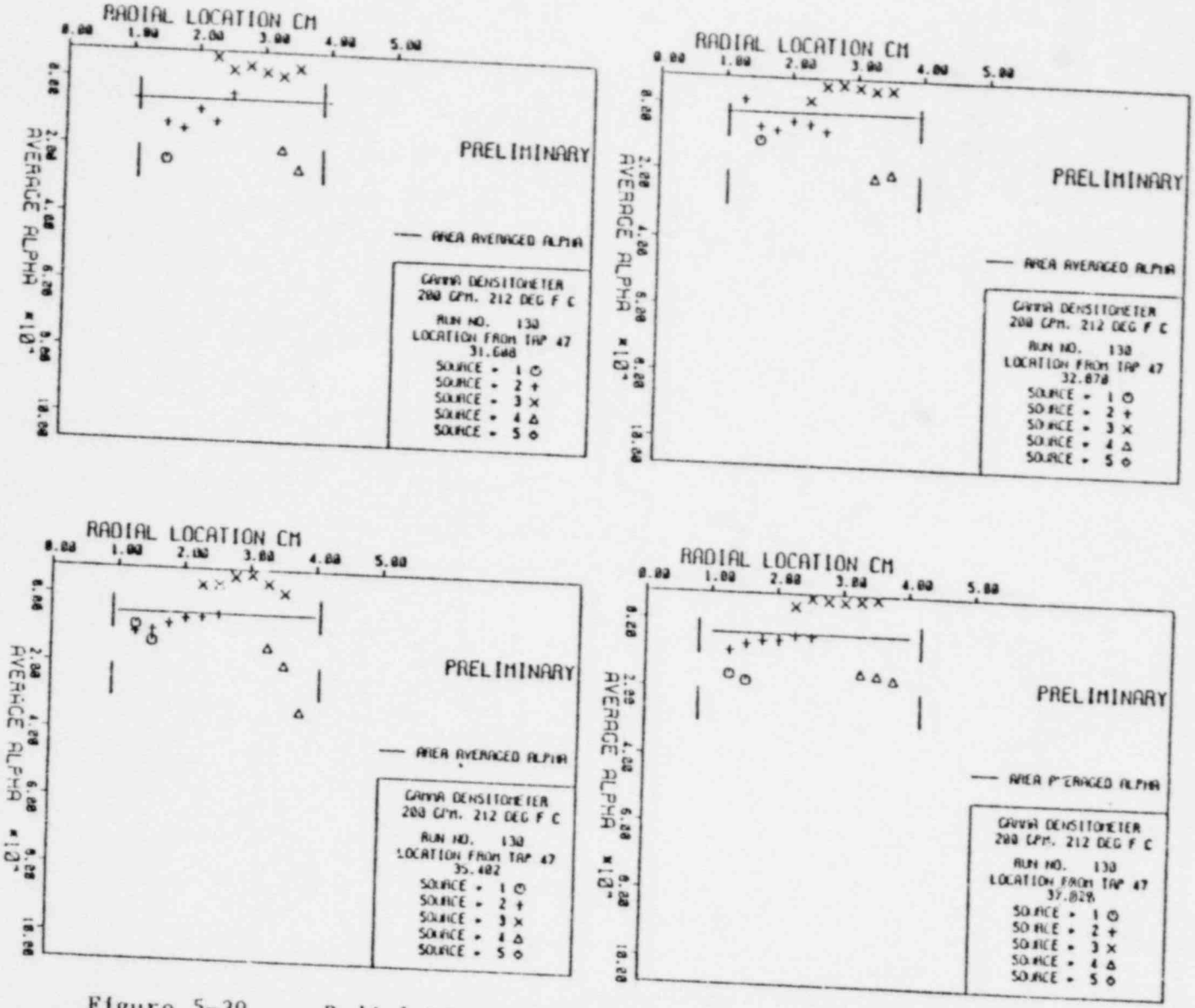

Figure 5-39 - Radial Distributions of the Chordal Averaged Void Fractions at Various Axial Locations Obtained by the Five Beam Gamma Densitometer for Run 130. (BNL Neg. No. 10-1412-79).

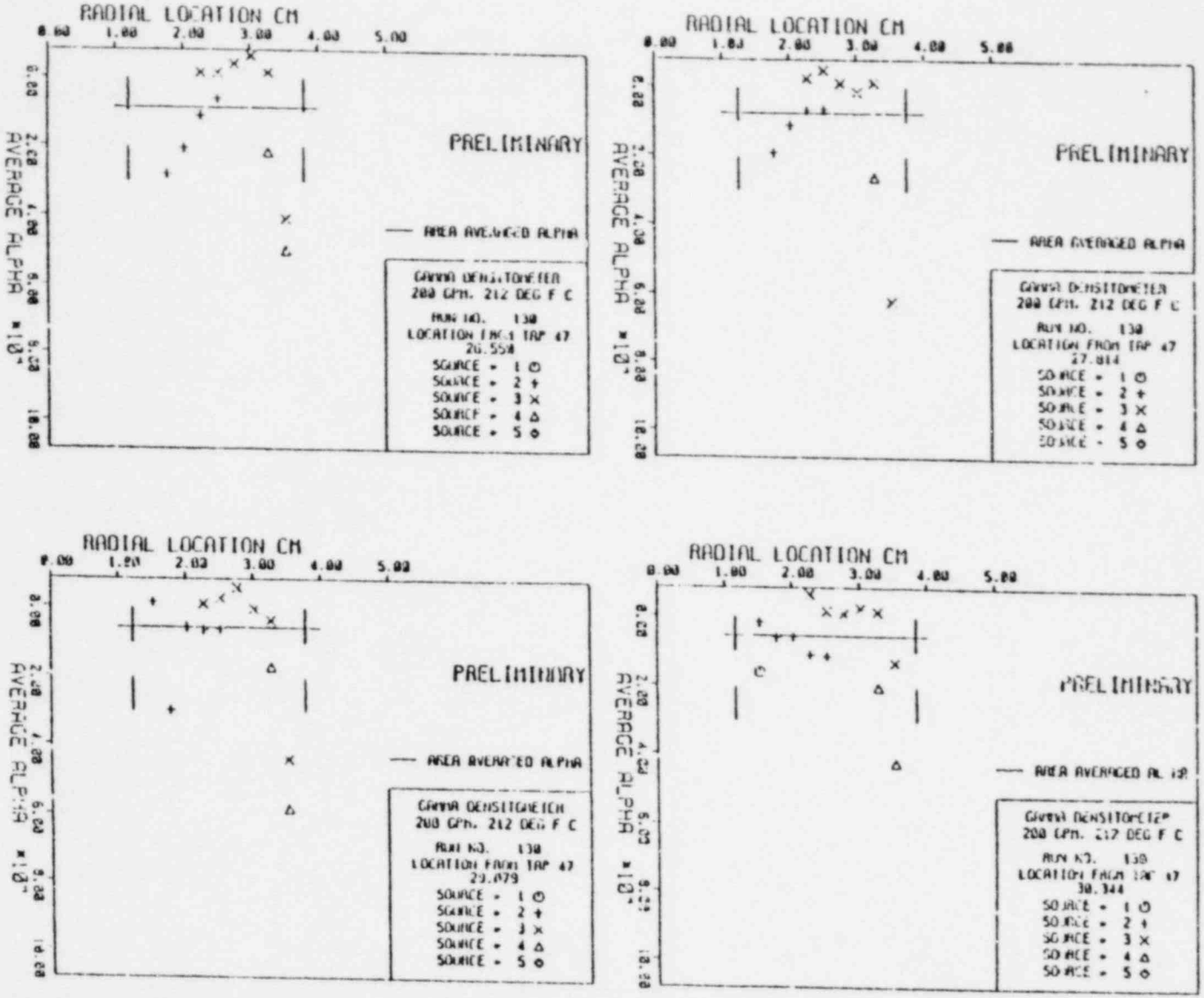

Figure 5-40 - Radial Distributions of the Chordal Averaged Void Fractions at Various Axial Locations Obtained by the Five Beam Gamma Densitometer for Run 130. (BNL Neg. No. 10-1400-79).

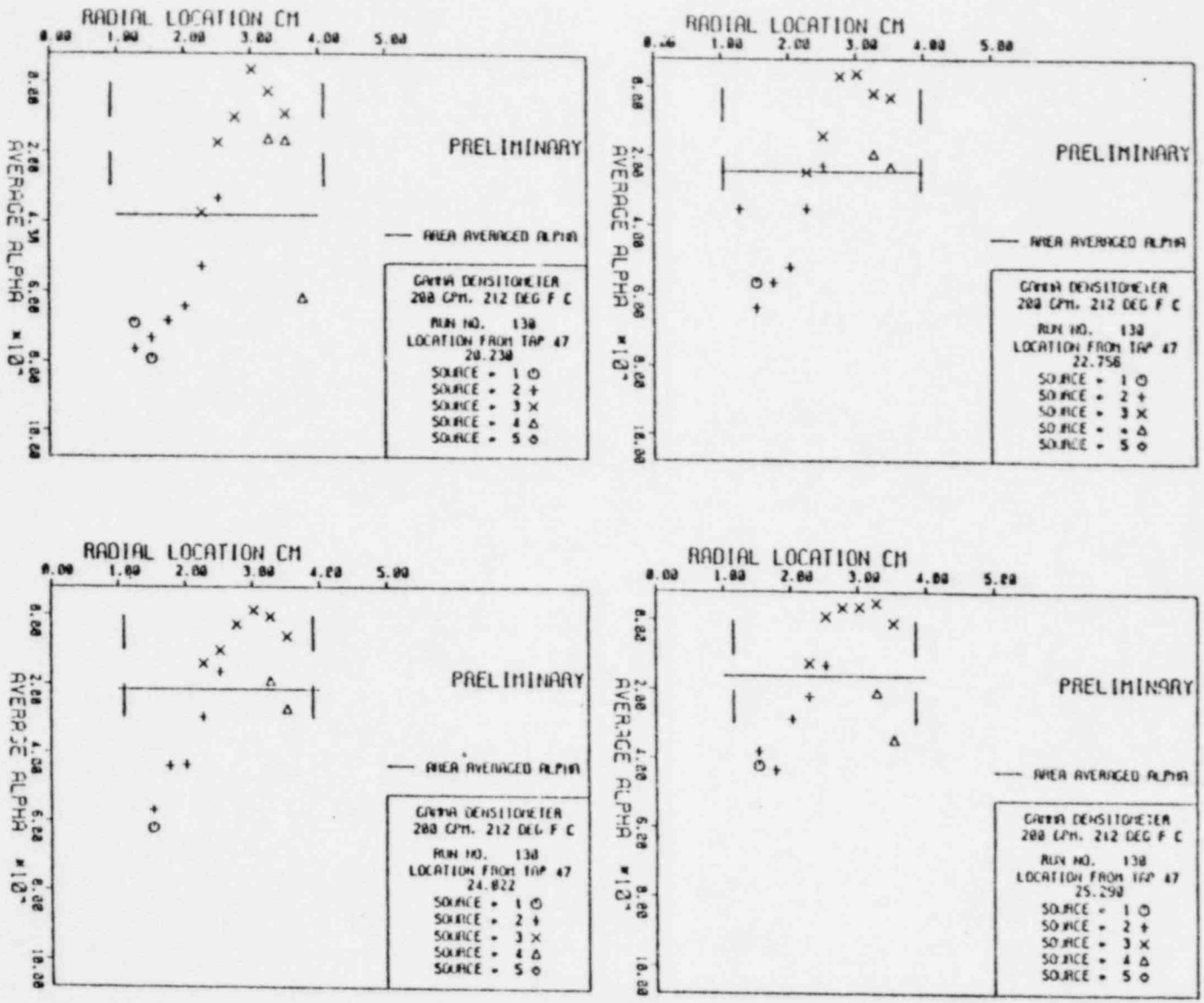

Figure 5-41 - Radial Distributions of the Chordal Averaged Void Fractions at Various Axial Locations Obtained by the Five Beam Gamma Densitometer for Run 130. (BNL Neg. No. 10-1410-79).

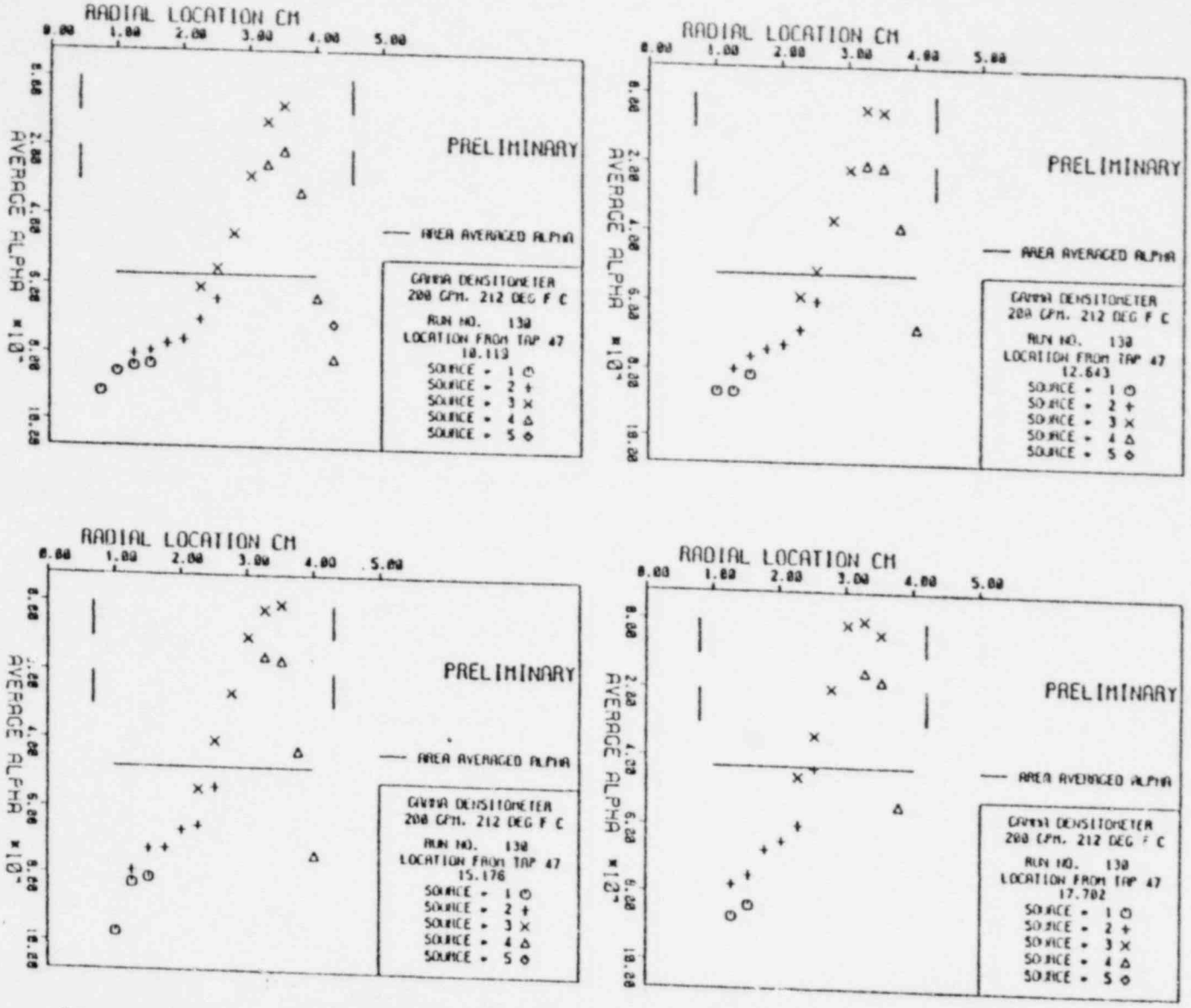

Figure 5-42 - Radial Distributions of the Chordal Averaged Void Fractions at Various Axial Locations Obtained by the Five Beam Gamma Densitometer for Run 130. (BNL Neg. No. 10-1407-79).

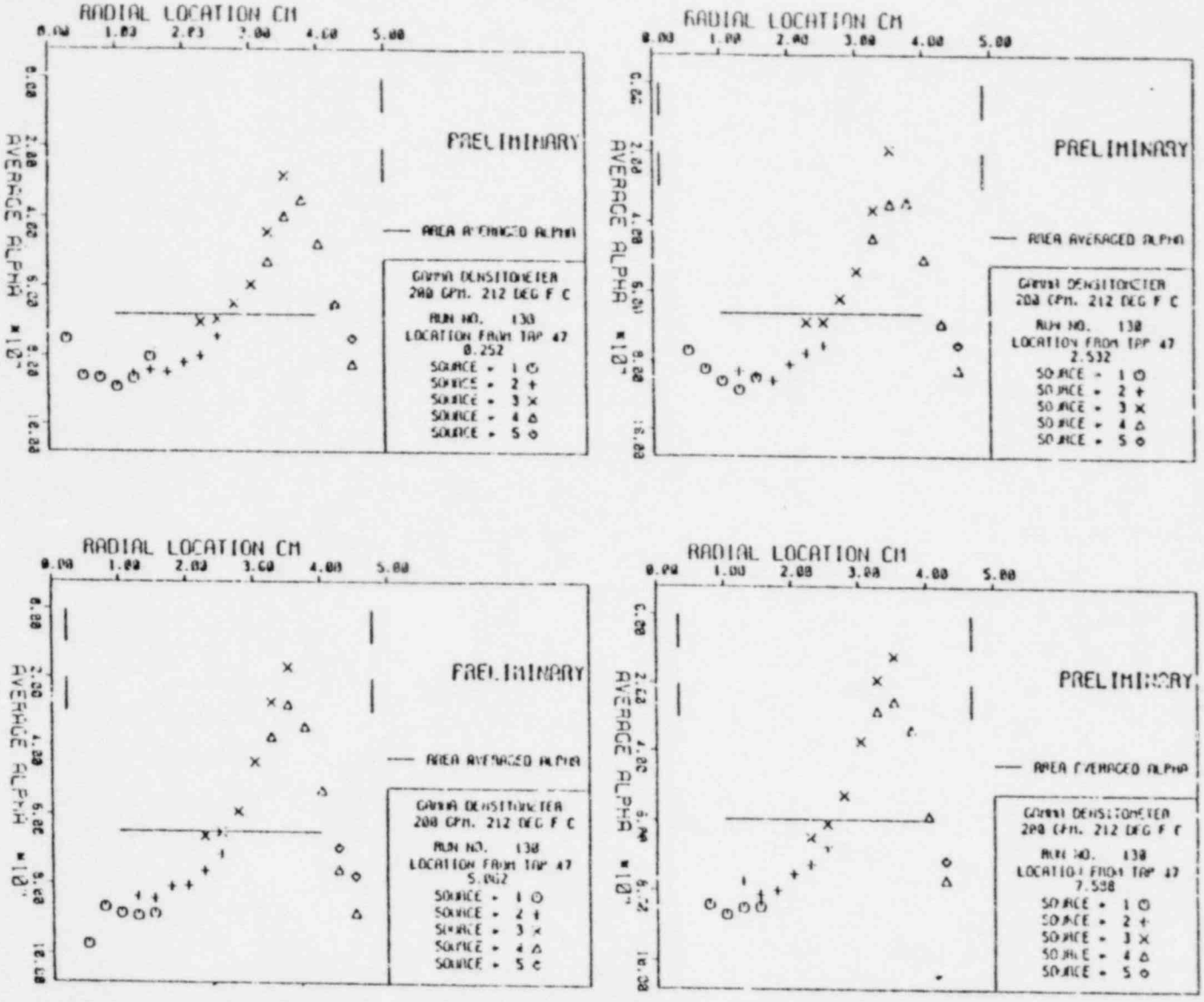

Figure 5-43 - Radial Distributions of the Chordal Averaged Void Fractions at Various Axial Locations Obtained by the Five Beam Gamma Densitometer for Run 130. (BNL Neg. No. 10-1409-79).

Some preliminary observations from this set of data is that the void profile is not symmetrical with respect to the axis of the tube. The void profiles seem to imply the presence of a low void fraction core, surrounded by a high void fraction envelop close to the walls. As we get closer to the throat of the nozzle, the area-averaged void fraction decreases and gets closer to the all liquid single phase value. The scatter of the points close to the wall and upstream of the throat could be attributed to the fact that the extreme locations, close to the walls, the calibrations (both empty and full) change drastically, thus a small error in the locations ($\sim$ 0.005") can cause a large error in the voids measured, since the difference between full and empty is also small in the same region. All our data recorded include absolute locations in the transverse direction and therefore the proper corrections will be applied as a function of location in the final report. Time has not allowed this to be done for this interim report. The difference in the void fraction measured by two neighboring sources at the same location near the nozzle centerline is a result of the unsteady nature of the flashing flow, not scatter since no scatter was presented in the empty and full calibrations.

5.4 Calculations of Net Vapor Generation Rates Under Flashing Conditions

In this section, we shall present the method with which a cross-section-averaged net vapor generation rate per unit volume Γ_v may be determined from the measured pressure and void fraction distribtuions along the test section. We recall the following definitions of cross-section-averaged quantities.

Mixture density,

$$\langle \rho \rangle = \langle \alpha \rho_v \rangle + \langle (1 - \alpha) \rho_\ell \rangle \tag{5-2}$$

Mass flux of vapor,

$$\langle G_v \rangle = \langle \alpha \rho_v u_v \rangle \tag{5-3}$$

Liquid mass flux,

$$\langle G_\ell \rangle = \langle (1 - \alpha) \rho_\ell u_\ell \rangle \tag{5-4}$$

Total mass flux,

$$\langle G \rangle = \langle G_v \rangle + \langle G_\ell \rangle \tag{5-5}$$

Total volume flux,

$$\langle j \rangle = \langle \alpha u_v \rangle + \langle (1 - \alpha) u_\ell \rangle \tag{5-6}$$

Quality,

$$\langle x \rangle = \langle G_v \rangle / \langle G \rangle \tag{5-7}$$

We shall assume that the densities ρ_v and ρ_ℓ of the vapor and liquid phases are given by the saturation values corresponding to the local pressure p, and therefore, are constant over a cross-section. Moreover, we

shall assume that the vapor drift velocity

$$V_{gj} = u_v - j \tag{5-8}$$

is also constant over a cross-section. Combining Eqs. (5-7) and (5-3) & using the drift velocity, Eq. (5-3) we have

$$\begin{aligned} \langle x \rangle \langle G \rangle &= \langle \alpha \rho_v j \rangle + \langle \alpha \rho_v V_{gj} \rangle \\ &= \rho_v (\langle \alpha j \rangle + \langle \alpha \rangle V_{gj}). \end{aligned} \tag{5-9}$$

Introducing the distribution parameter $C_o = \langle \alpha j \rangle / \langle \alpha \rangle \langle j \rangle$, we may write

$$\langle x \rangle \langle G \rangle = \rho_v (C_o \langle \alpha \rangle \langle j \rangle + \langle \alpha \rangle V_{gj})$$

which may be expressed as

$$\langle x \rangle \langle G \rangle = \rho_v \langle \alpha \rangle \left[C_o \left(\frac{\langle x \rangle \langle G \rangle}{\rho_v} + \frac{\langle 1 - x \rangle \langle G \rangle}{\rho_\ell} \right) + V_{gj} \right],$$

when Eqs. (5-6), (5-3), and (5-4) are inserted. Solving for the cross-section-averaged quality $\langle x \rangle$ and replacing the liquid and vapor densities with their saturation values, we get finally

$$\langle x \rangle = \frac{\langle \alpha \rangle \left[C_o \frac{\rho_g}{\rho_f} + \frac{\rho_g V_{gj}}{\langle G \rangle} \right]}{1 - \langle \alpha \rangle C_o \frac{\rho_f - \rho_g}{\rho_f}} . \qquad (5\text{-}10)$$

The vapor drift velocity is assumed to be given by the expression for the churn-turbulent upflow of a bubbly mixture,

$$V_{gj} = K \left[\frac{\sigma g (\rho_f - \rho_g)}{\rho_f^2} \right]^{1/4} , \qquad (5\text{-}11)$$

where the coefficient K = 1.41 according to Kroeger and Zuber (1968). For a given set of test section inlet conditions, we may assume that C_o remains constant in the test section, and that the variation of the liquid density ρ_f is negligible. Thus V_{gj} varies only weakly with ρ_g, and we shall assume V_{gj} to be roughly constant in the test section as well. Hence $\langle x \rangle$ may be considered as an explicit function of the local cross-section averaged void fraction, the vapor density and mixture mass flux.

From conservation of vapor mass, we have

$$\Gamma_v = \langle G \rangle d\langle x \rangle / dz , \qquad (5\text{-}12)$$

which leads to, after dropping the symbol < >,

$$\Gamma_v = \frac{\frac{Gx}{\alpha}\frac{d\alpha}{dz} + \frac{Gx}{\rho_g}(1 - \alpha C_o)\frac{d\rho_g}{dp}\frac{dp}{dz} - \frac{\alpha\rho_g V_{gj}}{G}\frac{dG}{dz}}{1 - \alpha C_o(\rho_f - \rho_g)/\rho_f} \qquad (5\text{-}13)$$

where we have replaced $d\rho_g/dz$ by $[(d\rho_g/dp)(dp/dz)]$. The quantities $d\alpha/dz$ and dp/dz in Eq. (5.13) may be obtained from the experiments, and $d\rho_g/dp$ is given by the equation of state of the vapor, or the steam table. We note, from the mixture continuity equation

$$\frac{1}{G}\frac{dG}{dz} = -\frac{1}{A}\frac{dA}{dz} = -\frac{1}{(A/A^+)}\frac{d(A/A^+)}{dz} \quad . \qquad (5\text{-}14)$$

To account for the frictional effects in an approximate manner, the effective cross-sectional area distribution $(A/A^+)_{eff}$ determined from single phase calibrations instead of the geometrical area distribution were used in the reported calculations. This is probably a good assumption in the convergent section where the favorable pressure gradient is expected to keep the wall boundary layers thin and attached. Greater uncertainty arises when such a procedure is applied to the divergent part of the test section where the boundary layer displacement in two-phase flow may be significantly different from the single-phase flow under adverse pressure gradients. Thus, all terms in Eq. (5-13) may be evaluated as a function of z and the net vapor generation rate may be calculated.

Figure 5-44 shows an example of Γ_v thus determined for the convergent part of the test section. In this figure, the top graph displays the measured pressure and void distributions in the experiments. In addition, least-square polynomial fits to the measured data are also shown for comparison. The derivatives of α and p may be evaluated along the fitted polynomials, instead of through the actual data points, which may lead to considerable scatter. The Γ_v values calculated from Eq. (5-13) are exhibited in the bottom graphs. It is seen that Γ_v's of the order of 10^2 kg/m^{3}s are attained in these experiments, which are in approximately the same range as those found Reocreux's (1974) experiments.

It was found that the value of Γ_v was dominated by far by the variation of α with z in these experiments. For example, for Runs 82/821 at z = 254 mm, the value of the three terms in the numerator in Eq. (5-13) are

$$(Gx/\alpha)d\alpha/dz = 22.53 \text{ kg/m}^3\text{s},$$

$$(Gx/\rho_g)\ (1 - \alpha C_o)\ (d\rho_g/dp)\ (dp/dz) = -\ 2.66 \text{ kg/m}^3\text{s},$$

$$(\alpha\rho_g V_{gj}/G)dG/dz = 0.33 \text{ kg/m}^3\text{s},$$

where V_{gj} = 0.21 m/s.

Thus, the term involving dG/dz, which is directly proportional to the drift velocity assumed, contributes about one percent to the value of Γ_v. Any uncertainty in the assumption of V_{gj} is expected to lead to insignificant

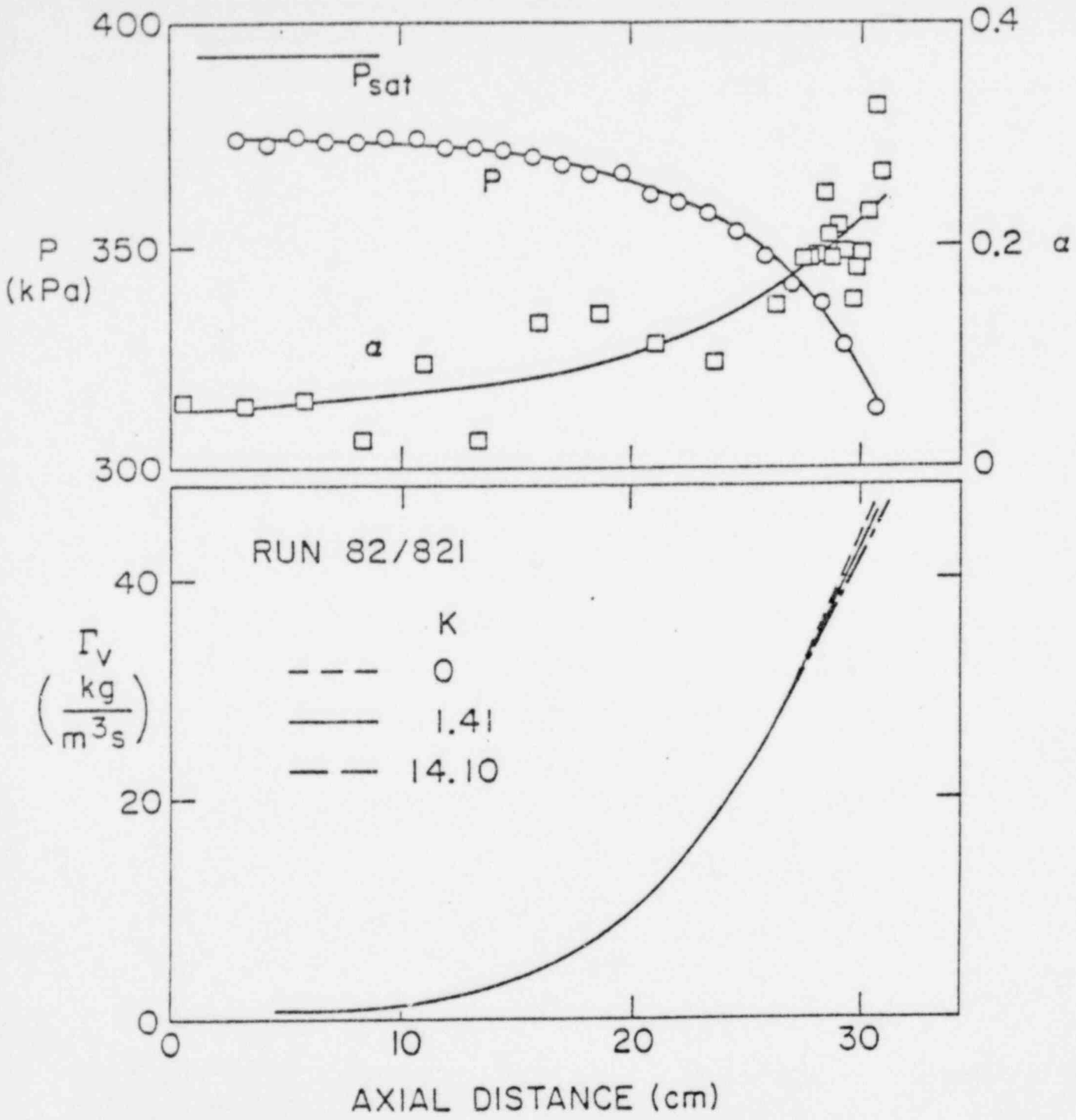

Figure 5-44 Top: Measured Pressure (o) and Void Fraction (□) Distributions in the Converging Part of the Test Section in Runs 82/821 and the Least Square Polynomial Fit to Data. Bottom: Calculated Net Vapor Generation Rate Based on the Least Square Fit to the α and p Data. (BNL Neg. No. 3-1226-79).

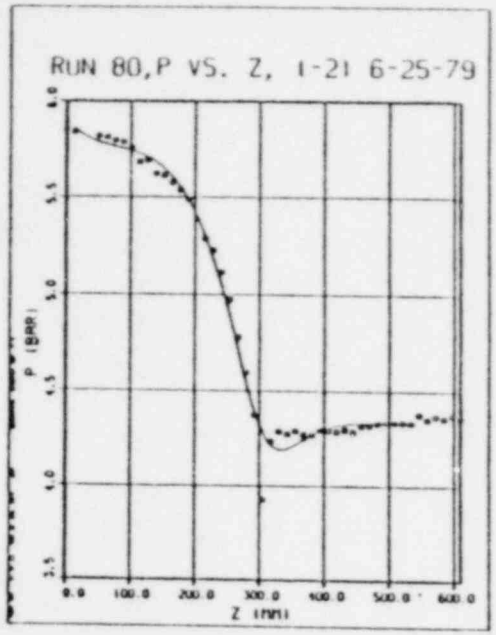

A

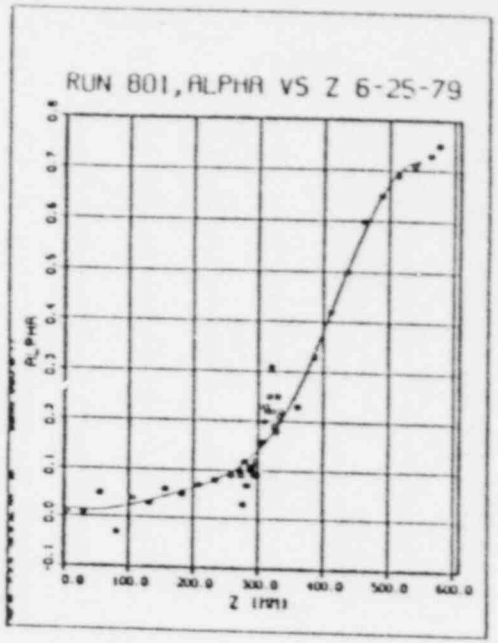

B

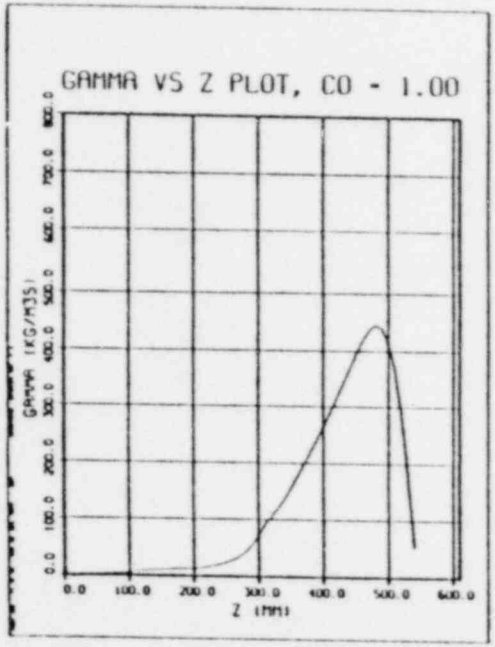

C

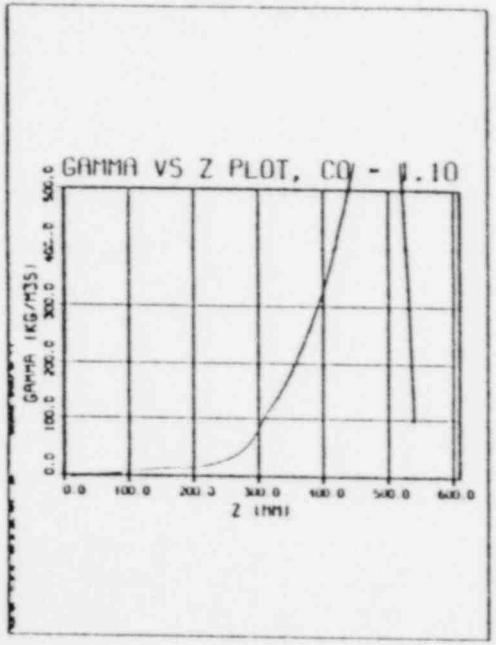

D

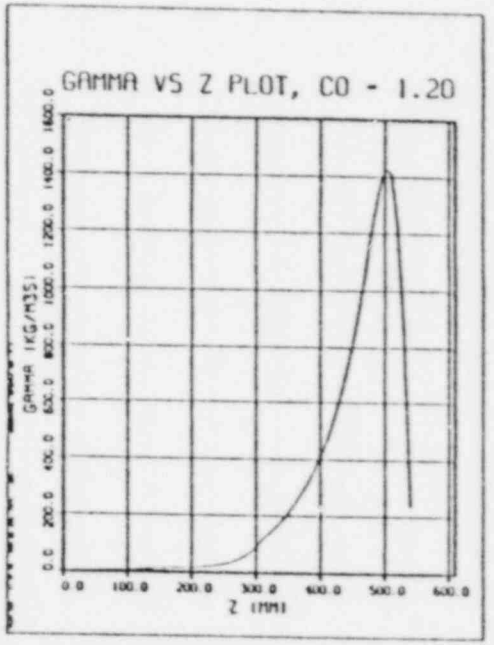

E

Figure 5-45 Results of Calculation on Data of Runs 80/801. (A) and (B): Pressure and Void Fraction Distributions; □, Measured; —— Cubic Spline Fit; +, Optimum Knot Locations. (C), (D), and (E) Calculated Value of Rate of Vapor Generation Γ_v for Three Values of the Distribution Parameter C_o (BNL Neg. No. 7-486-79).

errors in Γ_v thus determined. In Fig. 5-44, we have also shown Γ_v's calculated for zero drift velocity and a ten-fold increase in V_{gj} (taking K = 0 and 14.1, respectively, in Eq. (5-11). The difference between the three curves are indeed small. Hence, it may be concluded that void fraction and pressure distribution measurements are adequate for the determination of cross-section averaged vapor generation rates. Additional data are shown in 5-45 in which the smoothing and interpolation routines of the LMSLX computer program package were used to obtain piecewise continuous least squares cubic spline curve fits to the pressure and void distribution data. The location of the "knots", where neighboring pieces of the spline fit are joined, are optimized by the computer, based on initial guesses specified in the input. The cubic spline fit thus computed is continuous and has continuous first and second derivatives. The initial guess of the location of knots and the number of knots specified are found to influence the cubic splines computed. Hence, some trial and error are required in using this program to determine the vapor generation rates. Typical results of such a calculation for Runs 80 and 801 (Zimmer 1979) are exhibited in Figs. 5-45A to 5-45E. Here the test section entrance is at Z = 0 mm, the throat at Z = 305 mm and exit at 610 mm. The measured pressure and void fraction distributions are shown by the squares in Figs. 5-45A and 5-45B, respectively; the least square fits are shown by the curves, and the "knots" are indicated by the + symbols. The values of Γ_v calculated for three values of the distribution parameter C_o = 1.0, 1.1, and 1.2 (see Zimmer 1979) are plotted in Figs. 5-45C, 5-45D, and 5-45E. It is seen that for high α values ($\alpha \gtrsim 0.5$), Γ_v may be quite sensitive to the

value of C_o assumed in the calculations. This is because the quantity $[1 - \alpha C_o(\rho_f - \rho_g)/\rho_f]$ appears in the denominator of the Γ_v expression, where ρ_f and ρ_g are the densities of the liquid and vapor, respectively, and the bracketed quantity approaches zero when α approaches $1/C_o$ since $\rho_g << \rho_f$. Methods are currently being investigated to reduce or eliminate this sensitivity.